TURUN
YLIOPISTO
UNIVERSITY
OF TURKU

Advanced characterization of thermally sprayed thin-film all-solid-state batteries

Arman Hasani

TURUN YLIOPISTON JULKAISUJA – ANNALES UNIVERSITATIS TURKUENSIS
SARJA – SER. F OSA – TOM. 76 | TECHNICA – INFORMATICA | TURKU 2026

TURUN
YLIOPISTO
UNIVERSITY
OF TURKU

ADVANCED CHARACTERIZATION OF THERMALLY SPRAYED THIN-FILM ALL-SOLID-STATE BATTERIES

Arman Hasani

TURUN YLIOPISTON JULKAISUJA – ANNALES UNIVERSITATIS TURKUENSIS
SARJA – SER. F OSA – TOM. 76 | TECHNICA – INFORMATICA | TURKU 2026

University of Turku

Faculty of Technology
Department of Mechanical and Materials Engineering
Mechanical Engineering
Doctoral programme in Technology (DPT)

Supervised by

Associate Professor, Ashish Ganvir
University of Turku, Finland

Professor, Antti Salminen
University of Turku, Finland

Dr. Sneha Goel
VTT Oy Finland

Reviewed by

Dr. Richard Trache
TREIBACHER INDUSTRIE AG, Austria

Dr. Jarkko Kiilakoski
Owens Corning (Paroc), Turku, Finland

Opponent

Associate Professor, Heli Koivuluoto

Tampere University, Finland.

ISBN 978-952-02-0545-4 (PRINT)
ISBN 978-952-02-0546-1 (PDF)
ISSN 2736-9390 (Print)
ISSN 2736-9684 (Online)
Painosalama, Turku, Finland, 2026

To my dear father and mother, for their endless love and support, and to my beloved homeland, Iran, the source of my inspiration.

تقدیم به پدر و مادر عزیزم به پاس عشق و حمایت بی پایانشان، و به وطن عزیزم ایران، سرچشمه ی امید و الهام من.

UNIVERSITY OF TURKU
Faculty of Technology
Department of Mechanical and Materials Engineering
Mechanical Engineering
ARMAN HASANI: Advanced Characterization of Thermally Sprayed Thin-Film All-Solid-State Batteries
Doctoral Dissertation, 203 pp.
Doctoral Programme in Technology (DPT)
February 2026

ABSTRACT

The global push toward electrification, renewable integration, and safer energy storage has intensified the demand for next-generation battery technologies. Thin-film all-solid-state batteries (TFASSBs) have emerged as promising candidates due to their intrinsic safety, long cycle life, and compatibility with miniaturized and flexible devices. However, their widespread adoption is hindered by slow, complex, and expensive fabrication methods that limit scalability and industrial uptake. Addressing this manufacturing challenge requires alternative deposition routes capable of producing high-quality ceramic layers with controlled microstructure and interfaces-at scale.

The transition toward safer and high-performance TFASSBs requires scalable manufacturing routes capable of producing high-quality ceramic layers with well-controlled microstructure, interfacial integrity, and phase stability. This thesis explores thermal spraying, specifically high velocity oxy fuel (HVOF), atmospheric plasma spray (APS), and suspension plasma spray (SPS), as an industrially viable approach for depositing Lithium Titanate (LTO) anodes and Lithium Lanthanum Zirconium Oxide (LLZO) solid electrolytes, and investigates how these processes govern microstructural evolution, chemical stability, and lithium retention in thin-film architectures. Owing to the inherent heterogeneity of thermally sprayed ceramic thin-films, conventional laboratory techniques (SEM/EDS, XRD, XPS) provide only bulk-averaged insight, lacking required accuracy. To address this limitation, synchrotron μXRD/μXRF mapping is employed to obtain quantitative, micron-scale structural and elemental information across thin-film cross-sections and buried internal interfaces.

The results reveal strong process–structure relationships: HVOF and APS thin-films better preserve the LTO spinel phase, while SPS thin-films exhibit severe lithium volatilization and form secondary phases such as Li_2TiO_3 and TiO_2. Synchrotron measurements uncover localized decomposition zones, through-thickness phase gradients, and interfacial diffusion effects that remain invisible to lab-scale XRD, SEM and EDS. XPS further highlights distinct surface chemistries, with HVOF and APS forming Li_2CO_3-rich surface layers, whereas SPS experiences substantial lithium depletion.

Laser post-processing (LPP) was introduced as a complementary, localized treatment for refining thermally sprayed thin-films. LPP enables rapid surface

remelting, densification, and smoothening without globally heating the substrate, thereby restoring crystallinity, suppressing plasma-induced secondary phases, reducing surface roughness, and improving interfacial uniformity in both LTO and LLZO layers. These improvements provide a promising pathway for engineering high-quality solid–solid interfaces in TFASSB configurations.

Electrochemical testing correlates these structural and chemical findings with battery performance: APS- derived LTO electrodes exhibit the highest initial capacity, lowest polarization, and most stable cycling behavior, while SPS thin-films demonstrate poor performance due to extensive phase degradation. Together, the integration of thermal spraying, laser post-processing, and synchrotron micro-characterization establishes a robust, multi-scale framework linking processing conditions to microstructure, chemistry, and electrochemical behavior.

Overall, this work demonstrates how advanced synchrotron-based micro-characterization provides essential, spatially resolved insight into the process–structure–chemistry relationships governing thermally sprayed thin-film battery materials, while also highlighting thermal spray and laser post-processing as fast and scalable manufacturing routes for next-generation thin-film solid-state batteries.

KEYWORDS: Thin-film all-solid-state batteries (TFASSBs), thermal Spray, high velocity oxy fuel (HVOF), atmospheric plasma spray (APS), suspension plasma spray (SPS), laser post-processing (LPP), LTO, LLZO, Synchrotron μXRD, Synchrotron μXRF

TURUN YLIOPISTO
Teknillinen tiedekunta
Kone- ja materiaalitekniikan laitos
Konetekniikka
ARMAN HASANI: Termisesti ruiskutettujen kiinteä olomuodon ohutkalvo akkujen kehittynyt karakterisointi
Väitöskirja, 203 s.
Teknologian Tohtoriohjelma (DPT)
Helmikuu 2026

TIIVISTELMÄ

Globaali siirtymä kohti sähköistymistä, uusiutuvan energian integrointia ja turvallisempia energiavarastoja on lisännyt tarvetta seuraavan sukupolven akkuteknologioille. Ohutkalvoiset kiinteän elektrolyytin akut (TFASSB) ovat nousseet lupaaviksi vaihtoehdoiksi niiden luontaisen turvallisuuden, pitkän käyttöiän sekä siksi, että ne ovat yhteensopivia miniaturisoitujen ja joustavien laitteiden kanssa. TFASSBn laajamittainen käyttöönotto on kuitenkin edelleen haastavaa, sillä nykyiset valmistusmenetelmät ovat hitaita, monivaiheisia ja kustannusintensiivisiä, mikä rajoittaa prosessien skaalautuvuutta ja teollista soveltamista. Valmistuksen haasteiden ratkaiseminen edellyttää uusiapinnoitusmenetelmiä, jotka kykenevät tuottamaan korkealaatuisia keraami kerroksia, joilla on hallittu mikrorakenne ja rajapinnat skaalautuvasti.

Siirtymä kohti turvallisempia ja suorituskykyisempiä kiinteän olomuodon ohutkalvo akkuja edellyttää valmistusmenetelmiä, joilla voidaan tuottaa korkealaatuisia keraamisia ohutkalvoja joilla on hyvin kontrolloitu mikrorakenne, eheät rajapinnat ja vakaa faasi. Tässä väitöskirjassa tutkitaan termistäruiskutusta, erityisesti High-Velocity Oxy-Fuel (HVOF) -ruiskutusta, plasmaruiskutusta (APS) ja suspensioplasmaruiskutusta (SPS) teollisesti toteuttamiskelpoisena menetelmänä litiumtitanaatti- (LTO) anodien ja litium-lantaani-zirkoniumoksidi- (LLZO) kiinteäelektrolyyttien valmistukseen. Työssä tarkastellaan, miten nämä prosessit hallitsevat ohutkalvojen mikrorakenteen kehittymisen, kemiallisen vakauden ja litiumin säilymisen. Koska termisestiruiskutettujen keraamisten ohutkalvojen rakenteellinen heterogeenisuus on merkittävä, perinteiset laboratoriomenetelmien (SEM/EDS, XRD, XPS) tarjoama tilastollisesti keskiarvoistunut tieto ei ole riittävää. Tämän rajoitteen ratkaisemiseksi hyödynnetään synkrotronipohjaista µXRD-/µXRF-kartoitusta, jonka avulla saadaan kvantitatiivista, mikrometritarkkaa rakenne- ja alkuainejakaumatietoa ohutkalvojen poikkileikkauksista ja rakenteen sisään jääneistä rajapinnoista.

Tulokset osoittavat selviä prosessi–rakenne -suhteita: HVOF- ja APS-kalvot säilyttävät LTO-spinelfaasin parhaiten, kun taas SPS-kalvoissa havaitaan voimakasta litiumkatoa ja sekundaarifaaseja, kuten Li_2TiO_3 ja TiO_2. Synkrotronimittaukset paljastavat paikallisia hajoamisalueita, paksuussuunnassa vaihtelevia faasigradientteja ja rajapintadiffuusiota, jotka eivät ole havaittavissa laboratorioasteen XRD-, SEM- tai EDS-menettelyillä. XPS-mittaukset tuovat esiin

myös prosessikohtaiset pintakemiat: HVOF- ja APS-kalvoihin muodostuu Li_2CO_3-rikkaita pintakerroksia, kun taas SPS-kalvot kärsivät merkittävästä litiumkadosta.

Termisestiruiskutettujen ohutkalvojen rakenteen ja ominaisuuksien parantamiseksi työssä otettiin käyttöön laserjälkikäsittely (LPP). LPP mahdollistaa pinnoitteen nopean sulattamisen, tiivistämisen ja tasoittamisen ilman koko alustan lämpenemistä, parantaen kiteisyyttä, vähentäen plasmaindusoituja sekundaarifaaseja, pienentäen pintakarheutta ja parantaen LTO- ja LLZO-kerrosten rajapintojen tasalaatuisuutta. Nämä parannukset tarjoavat TFASSB-rakenteissa lupaavan reitin korkealaatuisten kiinteä–kiinteä -rajapintojen hallittuun muokkaukseen.

Sähkökemialliset mittaukset yhdistävät rakenteelliset ja kemialliset havainnot akkujen suorituskykyyn: APS-menetelmällä valmistetut LTO-elektrodit tarjoavat korkeimman alkuvarauskapasiteetin, pienimmän polarisaation ja vakaimman syklinkestävyyden, kun taas SPS-kalvojen suorituskyky oli heikko laajan faasihajoamisen vuoksi. Yhdessä terminenruiskutus, laserjälkikäsittely ja synkrotronimikromittaukset muodostavat monitahoisen viitekehyksen, joka yhdistää prosessiolosuhteet mikrorakenteeseen, kemiaan ja sähkökemialliseen käyttäytymiseen.

Tämä työ osoittaa, miten edistynyt synkrotronipohjainen mikromittaus tuottaa olennaisen, paikallisesti erottelevan näkymän termisestiruiskutettujen ohutkalvoakkujen prosessi–rakenne–kemia -suhteisiin ja samalla korostaa termistäruiskutusta ja laserjälkikäsittelyä nopeina ja skaalautuvina valmistusmenetelminä seuraavan sukupolven ohutkalvoisiin kiinteän elektrolyyttin akkuihin.

ASIASANAT: Ohutkalvoiset kiinteäelektrolyyttiset akut (TFASSB), terminenruiskutus, High Velocity Oxy Fuel (HVOF), Atmospheric Plasma Spray (APS), Suspension Plasma Spray (SPS), laserjälkikäsittely (LPP), LTO, LLZO, synkrotroninen µXRD, synkrotroninen µXRF

Table of Contents

Abbreviations

µXRD	micro-X-ray diffraction
µXRF	micro-X-ray fluorescence
ALD	Atomic layer deposition
APS	Atmospheric Plasma Spraying
ASSB	all-solid-state batterie
CGSM	cold gas-spraying methods
CV	Cyclic voltammetry
CVD	Chemical vapor deposition
CW	Continues Wave
D-gun	detonation gun
EDS	Energy dispersive spectroscopy
E_o	working voltage
$E_{p,\ a}$	Reduction voltage/ anodic potential
Ep, c	Oxidation voltage/ cathodic potential
FE-SEM	Field emission Scanning electron microscopy
FIB-milling	Focused ion beam milling
GCD	Galvanostatic charge–discharge
HVAF	high-velocity air fuel
HVOF	High-Velocity Oxy-Fuel
ICE	Initial coulombic efficiency
LIB	Lithium-ion batteries
LLZO	Lithium Lanthanum Zirconium Oxide, $Li_7La_3Zr_2O_{12}$
LPP	Laser Post-Processing
LPPS	low-pressure plasma spray
LTO	Lithium Titanium Oxide, $Li_4Ti_5O_{12}$
PAN	Polyacrylonitrile
PEO	Polyethylene oxide
PLD	Pulsed laser deposition
PSP^2	Process–Structure–Phase–Performance
PVD	Physical vapor deposition
ROI	Region of Interest

SEI	Solid electrolyte interphase
SEM	Scanning electron microscopy
SPS	Suspension Plasma Spraying
TFASSB	Thin-film all-solid state batteries
VPS	vacuum plasma spray
WS	warm spray
XPS	X-ray photoelectron spectroscopy
XRD	X-ray diffraction
XRF	X-ray fluorescence

List of Original Publications

This dissertation is based on the following original publications, which are referred to in the text by their Roman numerals:

I **Arman Hasani**, Shrikant Joshi, Antti Salminen, Sneha Goel, Joakim Reuteler, Malgorzata Grazyna Makowska, Ashish Ganvir. Localized Phase and Elemental Mapping in Solid-State Lithium Battery LTO Anode Thin-Film Produced by a Novel Suspension Plasma Spray Approach. *Journal of Thermal Spray Technology*, 2025; 34, pages 1589–1597. https://doi.org/10.1007/s11666-025-02003-6

II **Arman Hasani**, Antti Salminen, Shrikant Joshi, Malgorzata Grazyna Makowska, Behnam Chameh, Vesa-Pekka Lehto, Vinay Gidla, Sneha Goel, Ilari Angervo, Ashish Ganvir. Process-Dependent Phase Evolution in Thermally Sprayed $Li_4Ti_5O_{12}$ Thin-Film Battery Anodes Revealed by Advanced Synchrotron and Surface Characterization. *Materials and Design*, 2025; (submitted-under review).

III **Arman Hasani**, Shrikant Joshi, Antti Salminen, Sneha Goel, Antonin Breard, Mathias Juan, Malgorzata Grazyna Makowska, Ermei Mäkilä, Chinmayee Nayak and Ashish Ganvir. Advanced synchrotron micro characterization of laser post-processed plasma sprayed LLZO solid-state battery electrolyte. *IOP Conference Series: Materials Science and Engineering*, 2025; 1332. https://10.1088/1757-899X/1332/1/012022

IV **Arman Hasani**, Mathis Luya, Nikhil Kamboj, Chinmayee Nayak, Shrikant Joshi, Antti Salminen, Sneha Goel, Ashish Ganvir. Laser Processing of Liquid Feedstock Plasma-Sprayed Lithium Titanium Oxide Solid-State-Battery Electrode. *Coatings*, 2024; 14(2): 224. https://doi.org/10.3390/coatings14020224

V **Arman Hasani**, Chinmayee Nayak, Vinay Gidla, Antti Salminen, Shrikant Joshi, Vasanth Gopal, Ermei Makila, Mathias Juan, Ashish Ganvir. Laser Post-Processing as a Surface Engineering Strategy for Atmospheric Plasma-Sprayed Thin-Film All-Solid-State Battery Components. *Applied surface science*, 2026; (submitted).

The original publications have been reproduced with the permission of the copyright holders.

List of related publications not included in the thesis:

I. **Arman Hasani**, **Ameey Anupam**, Vinay Gidla, Nikhil Kamboj, Chinmayee Nayak, Shrikant Joshi, Antti Salminen, Ashish Ganvir. Advances in Manufacturing and Processing of Solid State Thin Film Batteries: A Review. (Manuscript is ready-to-submit)

II. **Vinay Gidla, Arman Hasani, Ashish Ganvir**, k/13/2025 / UTU12: A method to fabricate high performance battery electrodes using combustion-based flame spray technology for lithium ion batteries and solid-state batteries Patent application / Finland, Filed in October 2025

List of publications published during PhD (not related to thesis)

I. Chinmayee Nayak, **Arman Hasani**, Vinay Gidla, Ermei Mäkilä, Ebenezer Owusu, Nikhil Kamboj, Malgorzata Grazyna Makowska, Alex Lynam, Acacio Rincon Romero, Sneha Goel, Tanvir Hussain, Antti Salminen, Ashish Ganvir. High-Resolution Synchrotron µXRD and µXRF for Local Phase and Elemental Analysis in Suspension Plasma Sprayed Environmental Barrier Coatings. *Journal of Thermal Spray Technology,* 2026, (Accepted).

Declaration of AI use

An AI tool (ChatGPT) was used during the writing of this thesis only for improving the English language, restructuring my original text, and improving the flow of the text, based on my own original thoughts, research results, drafts, and outlines. All research ideas, experimental results, their interpretation and analysis, as well as all data, images, and schematics are entirely my own and do not involve any use of AI. AI tools were not used in any way to manipulate images, data, or results. All AI-generated suggestions were carefully reviewed and, where necessary, revised by me before being included in the thesis.

1 Introduction

The accelerating electrification of society, driven by climate targets and the integration of intermittent renewable energy sources, has created an urgent demand for safer, more efficient, and more durable energy storage technologies. Conventional lithium-ion batteries, while highly successful, rely on flammable liquid electrolytes and porous composite electrodes, which limit safety, thermal stability, and further gains in energy and power density. All-solid-state batteries (ASSBs) address many of these limitations by replacing the liquid electrolyte with an inorganic solid, enabling non-flammable, mechanically robust cells with wider operating temperature windows and the potential for higher energy density and longer lifetime.

Within the broader ASSB landscape, thin-film all-solid-state batteries (TFASSBs) occupy a particularly important niche. By reducing layer thicknesses to the micro- and nanometre scale, TFASSBs provide short Li^+ diffusion paths, low interfacial resistance, and excellent cycling stability, making them highly attractive for microelectronics, sensors, medical implants, and emerging flexible or miniaturized devices. However, the current state-of-the-art fabrication of TFASSBs is dominated by vacuum-based techniques such as sputtering, pulsed laser deposition, evaporation, and atomic layer deposition. Although these routes deliver dense and well-controlled films, they are inherently slow, area-limited, and capital intensive. As a result, they are poorly suited for large-area manufacturing or for scaling TFASSB concepts towards more industrially relevant formats.

This scalability bottleneck has motivated growing interest in thermal spray as an alternative manufacturing pathway for TFASSBs. Thermal spray processes, including atmospheric plasma spray (APS), suspension plasma spray (SPS), and high-velocity oxy-fuel (HVOF) offer high deposition rates, flexibility in coating large and non-planar substrates, and compatibility with a wide range of ceramic and metallic materials. For electrochemical systems, they provide a route to directly deposit functional oxide thin-films, such as lithium titanate ($Li_4Ti_5O_{12}$, LTO) anodes and garnet-type $Li_7La_3Zr_2O_{12}$ (LLZO) solid electrolytes, without the need for conventional high-temperature sintering of pressed pellets or tapes. In principle, this opens the door to fast, scalable, and binder-free fabrication of TFASSB architectures.

At the same time, the very attributes that make thermal spray attractive such as high enthalpy heat sources, rapid quenching, and non-equilibrium solidification, also introduce new scientific and technological challenges. Li-containing oxides are especially vulnerable to lithium volatilization, oxygen non-stoichiometry, and secondary phase formation under such extreme processing conditions. The resulting thin-films are often structurally heterogeneous, with lamellar microstructures, pores, splat boundaries, and rough surfaces that can compromise ionic transport and interface quality. These microstructural complexities are further amplified at solid–solid interfaces, such as those between LTO or LLZO and metallic current collectors, where local thermal gradients and diffusion processes can drive interfacial reactions, phase decomposition, and residual stresses.

Addressing these challenges requires both post-deposition microstructural engineering and advanced characterization tools capable of resolving local structural and chemical changes. Laser post-processing (LPP) provides a powerful, localized means of modifying thermally sprayed ceramics. By locally remelting and resolidifying the surface, LPP can densify porous regions, smoothen rough topography, and refine near-surface microstructure without globally heating the substrate. When applied to thermally sprayed LTO and LLZO thin-films, LPP has the potential to improve surface quality, enhance interfacial contact, and partially restore or stabilize functional phases that were degraded during spraying.

However, conventional laboratory characterization methods such as SEM/EDS, XRD, and XPS provide primarily bulk- or surface-averaged information and are often unable to capture the micro-scale heterogeneity that is intrinsic to thermally sprayed thin-films. Critical features such as through-thickness phase gradients, localized decomposition zones, lithium-depleted regions, and chemically modified interfacial layers can remain hidden when probed with techniques that average over large volumes. To obtain a mechanistic understanding of how thermal spray and LPP influence TFASSB constituents, it is therefore essential to employ synchrotron-based micro-characterization, in particular micro-X-ray diffraction (µXRD) and micro-X-ray fluorescence (µXRF). These techniques enable micron-scale mapping of crystalline phases and elemental distributions across thin-film cross-sections and buried interfaces, thereby revealing process–structure–chemistry relationships that are inaccessible to conventional tools.

Against this backdrop, this dissertation focuses on thermally sprayed LTO anodes and LLZO solid electrolytes as model TFASSB constituents and investigates how APS, SPS, and HVOF processes, combined with laser post-processing, govern microstructure, phase evolution, elemental gradients, and interfacial chemistry. By integrating lab-scale techniques with synchrotron µXRD/µXRF, the work establishes a multi-scale framework that links processing conditions to local structure and chemistry, and ultimately to electrochemical behaviour. The results are

used to elucidate the benefits and limitations of thermal spray as a manufacturing route for TFASSBs, to assess the role of LPP as a microstructural refinement tool, and to demonstrate the unique value of advanced synchrotron micro-characterization for non-equilibrium battery materials.

The following sections first outline the structure of the thesis and then detail the hypotheses, objectives, research questions, novelty, scope, and limitations that guide this work.

1.1 Thesis Outline

This dissertation is organized into six chapters, each addressing a key component of developing, modifying, and characterizing thermally sprayed TFASSB materials.

Chapter 1. Introduction

This chapter establishes the motivation for next-generation solid-state batteries, the rationale for using thermal spray deposition and laser post-processing, and the need for advanced micro-scale characterization. It presents the hypotheses, objectives, research questions, novelty, scope, and limitations of the work.

Chapter 2. Background

This chapter reviews the scientific and technological foundations relevant to the thesis. It discusses the energy-transition context, fundamentals of all-solid-state and thin-film batteries, key anode/electrolyte/cathode materials, and their processing requirements. Conventional TFASSB fabrication routes are compared with thermal spray technologies, highlighting existing challenges. The chapter also summarizes post-thermal treatments, advanced characterization tools, and identifies three major research gaps motivating the dissertation.

Chapter 3. Materials and Methods

This chapter details the materials used (LTO, LLZO), the thermal spray processes (APS, SPS, HVOF), and the laser post-processing (LPP) methodology. It outlines the complete characterization workflow, including SEM/EDS, XRD, profilometry, FIB, synchrotron μXRD/μXRF, XPS, and electrochemical testing. The aim is to establish a systematic and multi-scale approach to evaluate thin-film microstructure, chemistry, and performance.

Chapter 4. Results and Discussion

This chapter reports experimental findings from both lab-scale and synchrotron-scale characterization. It compares microstructure, phase composition, chemical states, and surface quality across APS-, SPS-, and HVOF-sprayed films. Electrochemical testing links these structural and chemical features to battery performance.

Chapter 5. Implications of Advanced Characterization

This chapter integrates the experimental outcomes into a broader understanding of TFASSB manufacturing. It introduces the PSP² (Process–Structure–Phase–Performance) matrix and proposes a multi-scale characterization framework for thin-film battery systems. The complementary roles of laboratory and synchrotron techniques are discussed, along with implications for scalable thermal-spray-based battery production.

Chapter 6. Summary and Conclusions

The final chapter summarizes the main findings of the thesis, emphasizing how thermal spray processes, laser post-processing, and synchrotron micro-characterization collectively enable improved understanding and optimization of ceramic TFASSB components. It concludes with recommendations for future research.

1.2 Hypothesis

Based on the identified research gaps (RG1–RG3), presented in detail in the background chapter including, the limited understanding of thermal-sprayed TFASSBs, the underexplored role of laser remelting in thermally sprayed TFASSBs, and the lack of localized synchrotron mapping across solid–solid interfaces in thermally sprayed TFASSBs the following hypotheses were formulated:

Hypothesis 1 (Linked to Research Gap 1): The thermal spray processes APS, SPS, HVOF, owing to their demonstrated success in producing multi-layered ceramic architectures in thermal barrier coatings (TBCs) and solid oxide fuel cells (SOFCs), will enable the deposition of high-quality thin-film electrode and electrolyte for TFASSBs with controlled microstructure, phase stability, and interface integrity.

Hypothesis 2 (Linked to Research Gap 2): LPP, due to its fast, localized, and controllable energy input, will densify, smoothen, and homogenize the inherently porous microstructures of thermally sprayed thin-films, thereby improving density, crystallinity, surface quality, and interfacial contact.

Hypothesis 3 (Linked to Research Gap 3): Synchrotron-based micro-characterization techniques (µXRD, µXRF) will reveal localized phase evolution, chemical gradients, elemental segregation, and interfacial reactions within thermally sprayed TFASSBs features that conventional bulk or surface-averaged techniques (XRD, SEM/EDS, XRF) cannot resolve such micro-scale heterogeneity. Therefore, synchrotron µXRD/µXRF will provide the spatially resolved structural and chemical insight required to understand interface evolution.

1.3 Objectives

The objective of this dissertation is:
To develop a fundamental understanding of how thermal spraying and laser post-processing influence the microstructure, phase evolution, elemental gradients, interfacial chemistry in thermally sprayed TFASSB ceramic constituents, using advanced synchrotron-based micro-characterization to establish robust process–structure–performance relationships.

1.3.1 Sub-Objectives

1- **Sub-Objective 1 (Linked to Hypothesis 1):** To investigate the influence of different thermal spray techniques (namely, APS, SPS and HVOF) and processing parameters on the microstructure, interfacial compatibility and phase stability of thermally sprayed TFASSB constituents, namely, LTO and LLZO thin-films anode and solid electrolyte, respectively.

2- **Sub-Objective 2 (Linked to Hypothesis 2):** To understand how laser post-processing modifies surface roughness, densification, crystallinity, and interfacial integrity in thermally sprayed TFASSB constituents.

3- **Sub-Objective 3 (Linked to Hypothesis 3):** To employ synchrotron µXRD/µXRF for obtaining quantitative, spatially resolved insights into localized phases, chemical gradients, and interface reactions across the film thickness, and to correlate these with electrochemical and structural performance.

1.3.2 Research Questions

This research is guided by the following three questions:

1- **RQ1 (Linked to Sub-Objective1):** How do different thermal spray processes (namely, APS, SPS and HVOF) and their parameters influence the microstructure, phase composition, and interface quality of thermally sprayed TFASSB constituents?

2- **RQ2 (Linked to Sub-Objective2):** How does laser post-processing refine, densify, and homogenize the microstructure and surface/interface characteristics of thermally sprayed TFASSB constituents?

3- **RQ3 (Linked to Sub-Objective3):** What localized structural and chemical features including phase gradients, elemental segregation, oxygen non-stoichiometry, and Li volatility effects can synchrotron µXRD/µXRF reveal

in thermally sprayed TFASSB constituents, and how do these insights enhance understanding of the process–structure–performance relationships in thermally sprayed TFASSBs?

1.4 Novelty

The novelty of this dissertation lies in establishing a first comprehensive, multi-scale understanding of thermally sprayed TFASSB constituents (anode and solid electrolyte), combining thermal spray deposition, laser post-processing, and synchrotron micro-characterization in an integrated framework. While thermal spraying has been explored extensively for coatings and structural ceramics, its application to electrochemically functional battery thin-films remains fundamentally underdeveloped. This work addresses that gap by advancing four key innovations:

(1) First systematic investigation of APS, SPS, and HVOF for LTO anode and LLZO solid electrolyte thin-film architectures. Previous studies focus primarily on vacuum-processed thin-films (sputtering, PLD, evaporation). This dissertation is the first to demonstrate how three distinct thermal spray processes influence phase stability, lithium retention, interfacial compatibility, and microstructural evolution in battery-relevant thermally sprayed thin-films. The comparative process–structure analysis provides unprecedented clarity on the suitability and limitations of each process.

(2) Introduction of LPP as a targeted microstructural refinement strategy for thermally sprayed battery thin-films. LPP has not been systematically evaluated for modifying thermally sprayed TFASSB constituents. This study shows how localized remelting, densification, and smoothing enable microstructural healing, surface chemistry stabilization, and interface quality improvement offering a new pathway for tailoring thermally sprayed thin-films for electrochemical applications.

(3) First use of high-resolution synchrotron µXRD/µXRF mapping to reveal local phase evolution and chemical gradients in thermally sprayed TFASSBs. Thermal spray thin-films exhibit inherent heterogeneity that cannot be fully resolved by conventional XRD, SEM/EDS, or XPS. This dissertation provides the first micron-scale insights into through-thickness phase gradients, localized decomposition zones, lithium volatility effects, and buried-interface reactions in LTO and LLZO thin-films. This methodological advance opens new avenues for characterizing thermally sprayed TFASSBs.

(4) Establishment of a unified process–structure–chemistry–performance framework for TFASSBs manufactured using thermal spray and LPP. By correlating spray parameters, post-processing conditions, microstructural signatures, chemical state evolution, and electrochemical behavior, the dissertation

produces a generalizable understanding of TFASSB fabrication using scalable, industrially relevant thermal spray techniques. This framework lays the foundation for future multi-layer thermally sprayed TFASSB development beyond the state-of-the-art.

Taken together, these contributions position this work as the first dissertation to systematically bridge thermal spray processing, localized laser modification, and synchrotron micro-characterization for the development of TFASSBs.

1.5 Scope

The scope of this thesis is restricted to the development, modification, and high-resolution characterization of oxide-based ceramic TFASSB constituents, specifically LTO anodes and LLZO solid electrolytes deposited by APS, SPS, and HVOF.

The study covers:

- Thin-film fabrication via thermal spraying (namely, APS, SPS and HVOF).
- Laser post-processing of thermally sprayed TFASSB constituents for microstructural refinement.
- Laboratory-scale and synchrotron micro-characterization (μXRD, μXRF, XRD, SEM/EDS, XPS, surface profilometry).
- Correlating processing conditions with local microstructure and phase evolution.

The focus remains on single-layer (anode or solid electrolyte) and bi-layer (solid electrolyte and anode) configurations rather than full multi-layer cell assembly which includes cathodes and current collectors. Furthermore, the emphasis is on elucidating process–structure–phase relationships rather than demonstrating full electrochemical cycling.

1.6 Limitations

To maintain scientific focus and ensure a controlled experimental scope, the following limitations apply to this dissertation:

- **Battery Type:** The study is restricted to TFASSBs and does not address liquid-electrolyte, polymer, hybrid, or bulk-format battery systems.
- **Material Chemistry:** Only oxide-based ceramic materials (LTO and LLZO) are investigated; no sulfide-, phosphate-, halide-, or polymer-based chemistries are included.
- **Fabrication Methods:** Among thermal spray processes, only APS, SPS, and HVOF are examined. Other techniques such as HVAF, cold spray, SPPS, and flame spray are excluded from this work.

- **Electrochemical Testing:** Electrochemical evaluation is limited to correlations between microstructural/chemical characteristics and expected performance. Full-cell assembly, long-term cycling, and rate-capability tests fall outside the scope.
- **Characterization Methods:** Advanced characterization focuses on synchrotron µXRD and µXRF mapping. In-situ, operando, or time-resolved characterization techniques are not considered.
- **Interfaces:** The study focuses on thin-film–substrate interfaces and does not include cathode layer or full multi-layer TFASSB stacks.

2 Background

2.1 Energy Transition and the Need for Batteries

The global transition away from fossil fuels is driven by the urgent need to mitigate climate change, air pollution, and environmental degradation. Electricity has emerged as a cleaner alternative, but its widespread adoption requires overcoming challenges related to power generation, long-distance transmission, and most critically energy storage. Batteries play a central role in this context, enabling the storage of intermittent renewable energy, stabilizing power grids, and supporting the decarbonization of transportation and industry [1] [2] [3] [4].

Secondary (rechargeable) batteries are widely used for energy storage in devices ranging from UPS systems and hybrid vehicles to portable electronics. Of these, lithium-ion (Li-ion) batteries are the most common, thanks to their high energy density, long cycle life, and ability to be recharged frequently [5].
However, their reliance on flammable liquid electrolytes limits further improvements in safety, thermal stability, and power performance. Issues such as leakage, thermal runaway, and poor high-temperature performance underscore the need for safer alternatives [6].

All-solid-state batteries (ASSBs) replace the liquid electrolyte and porous separator with a single solid electrolyte layer. This fully solid configuration enhances safety, widens the operating temperature window, improves structural stability, and offers the potential for higher energy density and longer cycle life [7] [5], [8]. Solid electrolytes are non-flammable, chemically stable, and capable of operating from approximately –50 °C to 200 °C significantly broader than conventional LIBs [9], [10], [11]. These advantages position ASSBs as an enabling technology for large-scale renewable integration, next-generation EVs, and advanced microelectronic systems.

2.2 All-Solid-State Batteries

All-solid-state batteries (ASSBs) employ a solid electrolyte that simultaneously conducts lithium ions and physically separates the electrodes. By eliminating the liquid phase entirely, ASSBs address the major failure modes of conventional LIBs

including flammability, leakage, gas evolution, and poor thermal stability, while enabling compact, mechanically robust cell architectures.

Figure 1 illustrates the fundamental distinction between LIBs and ASSBs: in ASSBs, the separator and liquid electrolyte are replaced by a single solid electrolyte layer, which provides mechanical integrity and safe ion transport.

Solid electrolytes also introduce new considerations for interface mechanics, processing, and transport behavior, yielding two distinct architectural classes within ASSB technologies: bulk ASSBs and TFASSBs.

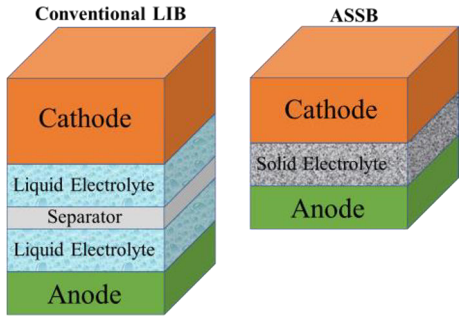

Figure 1. A schematic comparison illustrates that, unlike conventional LIBs, ASSBs do not include a separator or liquid electrolyte. Instead, a single inorganic solid electrolyte layer is placed between the two solid electrodes, enabling efficient lithium-ion transport while maintaining mechanical integrity and safety

2.2.1 Bulk ASSBs vs Thin-Film ASSBs (TFASSBs)

Bulk ASSBs generally employ thick (40 µm to 200 µm, and even up to 1 mm) oxide, sulfide, or composite electrolytes, either as bulk pellets or thick coatings, and can utilize high-capacity lithium-metal anodes [12], [13] . While they offer high energy density and excellent thermal stability, they face significant challenges related to interfacial resistance, mechanical brittleness, pressure requirements, and large-scale manufacturability.

In contrast, TFASSBs rely on much thinner films (from 50 µm down to 5 nm). Reported examples include LLZO films and sulfide composite films in the ~30–100 µm range, as well as ultrathin layers down to ~5 nm [14], [15]. These layers are typically deposited using precision thin-film techniques such as sputtering, pulsed laser deposition, or evaporation, which produce dense layers with sharp, well-defined interfaces suitable for microbattery integration [16], [17]. Typical TFASSB layer thicknesses reported in the literature include:

- Solid electrolyte: typically, 0.05–1.5 µm, down to ~50 nm, with some demonstrations using sub-100 nm films or up to a few micrometers depending on the process and function[18], [19],

- Cathode: typically, from a few micrometers to over 100 µm. For high-power applications, thinner cathodes of 25–50 µm are used, whereas high-energy applications employ thicker cathodes of ~90–120 µm [17], [19], [20], [21],
- Anode: can range from nanometers in thin-film cells to tens of micrometers (40-160 µm) in more conventional layered structures [22], [23].

These reduced length scales significantly shorten Li^+ diffusion distances and improve power density. However, they also magnify the role of interfacial stability, film uniformity, and material compatibility.
Electrochemical behaviour may be evaluated using half-cells (one active electrode with a stable counter electrode) or full cells (solid anode + solid electrolyte + solid cathode), providing flexibility in studying individual components or complete device behaviour [24], [25].

2.2.2 Cell Architecture and Working Principle of TFASSBs

TFASSBs consist of sequentially deposited thin-films including current collector, anode, solid electrolyte, and cathode supported on a suitable substrate. Their operation is governed by the behaviour of each individual layer and the interfaces between them.

2.2.2.1 Anode

The anode acts as the electron source during discharge while Li^+ migrates through the solid electrolyte toward the cathode. For TFASSBs, the anode must maintain both ionic and electronic conductivity, chemical compatibility with the solid electrolyte, and mechanical integrity under thin-film constraints. Minimizing interfacial resistance is central to reducing overpotential and ensuring efficient cycling. The fully solid configuration enhances safety, eliminating leakage and most thermal-runaway pathways [26], [27], [28].

2.2.2.2 Solid Electrolyte

The solid electrolyte defines ionic transport and interfacial stability. Ideal properties include: high ionic conductivity ($\sigma Li^+ \geq 10^{-4}$ S cm^{-1}), wide electrochemical stability window, mechanical robustness (particularly against dendrites), chemical compatibility with both electrodes, and minimal interfacial resistance.

Thin-film solid electrolytes must also form uniformly dense, pinhole-free with intimate electrode contact. Interfacial instability can trigger resistive interphases (e.g., SEI-like layers), reducing ionic conductivity and causing capacity fade. Interface engineering through protective films, compositional grading, or composite

architectures helps mitigate these effects. Although solid electrolytes are intrinsically safer due to their non-flammability, exothermic reactions with lithium metal and low thermal conductivity remain considerations for thermal management [26], [29], [30].

2.2.2.3 Cathode

The cathode governs the energy density and operating voltage. It must provide strong electronic conductivity, adequate ionic diffusion pathways, structural robustness, and chemical compatibility with the electrolyte [31], [32], [33]. Thin-film cathodes benefit from short lithium diffusion distances but suffer from limited areal capacity due to their restricted thickness. The cathode–electrolyte interface is often the dominant performance-limiting region, with issues such as poor wetting, interdiffusion, parasitic reactions, or space-charge layers leading to high interfacial impedance.

2.3 Materials for Thin-Film All-Solid-State Batteries (TFASSBs)

Material selection for TFASSBs is more constrained compared to bulk ASSBs because, in addition to electrochemical functionality, each layer must also be compatible with thin-film deposition. The subsections below first outline the material families commonly used in bulk ASSBs, followed by the additional considerations required for adapting these materials into thin-film battery architectures.

2.3.1 Anode Materials

In bulk ASSBs, anode chemistries include graphite, transition-metal oxides (TiO_2, Nb_2O_5, $TiNb_2O_7$), and polyanionic titanates such as $Li_4Ti_5O_{12}$. These are valued for their structural stability, safety, and well-understood lithiation mechanisms. In TFASSBs, the range of practical anode materials narrows considerably due to thin-film processing constraints, interfacial challenges, and the need to deposit uniform micrometre- or nanometre-scale layers. The most relevant anode systems include:

- Lithium metal (Li): Li offers the highest theoretical capacity (3,860 mAh g^{-1}) and lowest redox potential among anodes, making it the predominant choice for TFASSBs [34], [35]. However, dendrite formation and instability at solid–electrolyte interfaces remain critical issues, requiring interlayers or alloying strategies to mitigate failure [36], [37].
- Silicon (Si): Si provides exceptionally high theoretical capacity and is abundant and low-cost [38]. Its major drawback is the ~300% volume

expansion during lithiation, leading to mechanical failure, although nanostructuring and composite designs have been shown to reduce these effects [39], [40]. Si thin-films remain attractive [41], but their ionic conductivity is extremely low ($\sigma_i \approx 10^{-10}$–$10^{-8}$ S/cm), with Li^+ transport governed by diffusion coefficients of 10^{-16}–10^{-12} cm^2/s. Thin-film geometries partially compensate for these transport limitations.

- Graphite and Li–C compounds: These provide high electrochemical stability and are especially compatible with sulfide-based electrolytes. Although their capacity is lower than Li or Si, engineered composites can enhance performance [42], [43], [44].
- Li-alloy systems (Li–Si, Li–Sn, Li–Ge, Li–Al): These alloys balance high capacity with improved mechanical stability, partially suppressing dendritic growth [45], [46].
- Titanium-based oxides ($Li_4Ti_5O_{12}$, TiO_2, $TiNb_2O_7$): These exhibit excellent structural robustness, negligible volume change, thermal stability, and long cycle life [47], [48]. Their lower capacity is offset by exceptional reversibility, making them strong candidates for TFASSBs.
- Composite anodes: Systems such as Si/Li_3PS_4/carbon leverage synergistic effects to improve interfacial contact and cycling behavior [49], [50], [51].

2.3.2 Solid Electrolyte Materials

Solid electrolytes used in ASSBs fall into four primary families: oxide-based**,** sulfide-based**,** polymer-based, and composite systems. Oxide electrolytes such as LLZO ($Li_7La_3Zr_2O_{12}$) and LLTO ($Li_3xLa_{2/3}–xTiO_3$) offer excellent thermal and electrochemical stability [52], [53], [54], [55], [56], with cubic LLZO typically stabilised by Al, Ga, Ta, or Y doping [56]. Sulfide-based electrolytes like $Li_{10}GeP_2S_{12}$ and Li_6PS_5Cl have very high ionic conductivities (~10^{-3} S/cm) but require inert-gas handling and exhibit instability with many oxide electrodes [57], [58]. Polymer electrolytes (PEO, PAN) provide flexibility and ease of processing but have low room-temperature conductivity and modest mechanical strength [59], [60]. Composite electrolytes (LLZO/PEO, LATP/PVDF) aim to combine ionic conductivity with mechanical compliance [61], [62].

For TFASSBs specifically, additional constraints arise from thin-film deposition requirements such as vacuum compatibility, densification behaviour, pinhole-free morphology, and controlled interfacial chemistry. The most relevant solid electrolytes for TFASSBs include:

1. LiPON (Lithium Phosphorus Oxynitride): LiPON is the benchmark electrolyte for SSTFBs, with $\sigma_i \approx 10^{-6}$–10^{-5} S/cm, excellent stability against Li metal, and long-term cycling durability [63]. Variants such as nitrogen-rich, sulfur-doped, and fluorine-doped films have been explored to enhance conductivity and interfacial performance.
2. Oxide electrolytes (LLZO, LLTO): These offer high ionic conductivity but are difficult to adapt to TFASSB architectures due to their need for high-temperature processing and challenges in producing dense, pinhole-free thin-films [22].
3. Sulfide electrolytes: Rarely used in TFASSBs because they are air-sensitive and incompatible with vacuum deposition [64].
4. Polymer and composite systems: Although promising for flexibility, they remain largely experimental in thin-film formats [65].

Overall, despite broader research into oxide, sulfide, polymer, and composite systems, LiPON remains the most established solid electrolyte for TFASSBs due to its reliable thin-film processability and stable interfaces [66], [67].

2.3.3 Cathode Materials

Cathodes used in TFASSBs originate from the same material families as bulk LIB cathodes such as layered oxides, spinels, and polyanionic compounds, but must additionally be compatible with thin-film deposition and solid-electrolyte interfaces [68]. Key material families include:

1. Layered oxides such as $LiCoO_2$ (LCO), $LiNi_xMn_yCo_zO_2$ (NMC), $LiNi_{1-x-y}Co_xAl_yO_2$ (NCA). These provide high energy density but suffer from interfacial degradation, particularly with sulfide electrolytes [69], [70], [71]. LCO is the most established cathode in TFASSBs due to its high volumetric energy density and well-studied interface behaviour [72].
2. Phosphate-based cathodes such as $LiFePO_4$ (LFP), $Li_3V_2(PO_4)_3$ (LVP), $LiFePO_4F$ (LFPF). These materials offer excellent structural stability and safety but limited ionic conductivity [73], [74], [75], [76], [77] [78], [79], [80].
3. Spinels such as $LiMn_2O_4$ (LMO) and $LiNi_{0.5}Mn_{1.5}O_4$ (LNMO): Spinel structures ($LiMn_2O_4$, $LiNi_{0.5}Mn_{1.5}O_4$) provide 3D diffusion pathways and high-rate capability, making them attractive for TFASSBs. Although their capacity is modest (LMO: 148 mAh g^{-1}; LNMO: 147 mAh g^{-1}), their ionic conductivity (~10^{-6}–10^{-5} S/cm) is beneficial for thin-film architectures [81].

4. Sulfide-based cathodes such as Li_2FeS_2 (LFS), $Li_2S–P_2S_5$ (LSPS) composites: These compounds exhibit high capacity but are incompatible with vacuum deposition and are highly air-sensitive [82].

2.3.4 Current collectors and Substrate Materials

Current collectors and substrates play a crucial role in TFASSB manufacturability and interfacial performance. Noble metal foils (Pt, Au, Al, Cu) are widely used in lab-scale cells due to their conductivity and chemical stability, although they are costly and rigid. Silicon wafers provide atomically flat, defect-free surfaces ideal for precision deposition, but their cost and rigidity limit scalability. Flexible polymer substrates (polyimide, PET) enable lightweight and bendable battery designs but pose challenges in thermal stability and solvent resistance under high-temperature or vacuum deposition. Achieving an optimal balance among conductivity, chemical stability, flexibility, and cost remains central to enabling scalable TFASSB integration.

2.4 Manufacturing of All-Solid-State Batteries

Manufacturing of ASSBs requires the integration of multiple solid layers including electrodes, solid electrolytes, and current collectors into dense, stable, and chemically compatible architectures. Conventional fabrication approaches, largely inherited from ceramic processing and microfabrication, remain effective for producing laboratory-scale cells but face significant challenges in scalability, energy consumption, and interfacial quality. In bulk ASSBs, techniques such as powder compaction, high-temperature sintering, hot pressing, tape casting, and multilayer lamination are commonly employed. These processes provide reliable densification and structural uniformity; however, they often involve temperatures above 1000 °C, which can induce interfacial reactions, mechanical brittleness, or thermal expansion mismatch between active materials and solid electrolytes. Additionally, multilayer stacking introduces alignment, pressure distribution, and residual stress challenges, limiting compatibility with flexible or thin architectures [83], [84], [85], [86], [87]. Processing requirements also vary significantly across material classes. Oxide electrolytes typically demand high-temperature sintering to achieve adequate density and ionic conductivity, which can degrade interfacial chemistry and induce phase changes. In contrast, sulfide-based electrolytes can be densified at lower temperatures but require stringent inert-atmosphere handling to avoid moisture-induced decomposition. Ensuring clean, well-bonded interfaces, controlling densification behavior, and preventing undesired reactions across multiple solid

layers remain central manufacturing bottlenecks. These limitations have driven interest in alternative, and more scalable fabrication methods for next-generation ASSB architectures [88] [89].

2.4.1 Conventional Manufacturing of TFASSBs and Associated Challenges

TFASSBs rely on thin-films to achieve short ion transport paths, low interfacial resistance, and high energy density at miniature scales. Conventional thin-film fabrication techniques, primarily derived from microelectronics, enable highly uniform and defect-free layers but face challenges in throughput, deposition area, and economic viability for large-scale production. These methods can be broadly categorized into vacuum-based, solution-based, and printing-based routes.

2.4.1.1 Vacuum-Based Thin-Film Deposition

Physical vapour deposition (PVD) techniques such as sputtering, thermal evaporation, and electron-beam evaporation are among the most widely employed for thin-film solid electrolytes and electrodes. They offer excellent control over thickness, density, and stoichiometry, enabling the deposition of high-quality materials such as LiPON, LLZO, and $LiCoO_2$. However, their slow deposition rates, high vacuum requirements, limited deposition area, and fixed line-of-sight processing make industrial scaling difficult and costly [90] [91].

Chemical vapour deposition (CVD) and atomic layer deposition (ALD) offer conformal coatings and atomic-level thickness control, which are beneficial for ultrathin electrolyte films and engineered interfaces. Despite their precision, these methods suffer from extremely slow growth rates, precursor costs, and complex reactor requirements, further limiting their practical adoption [92].

Pulsed laser deposition (PLD) enables stoichiometric transfer and high-quality films for materials such as LLZO, Li_3PO_4, and $LiCoO_2$; however, its tiny deposition footprint, sensitivity to target–substrate alignment, and equipment complexity restrict its use to fundamental research [93].

2.4.1.2 Solution-Based and Wet Chemical Routes

Solution-based approaches such as sol–gel deposition, chemical solution deposition, and wet coating offer simpler and more cost-effective routes for large-area thin-films. These methods can cover complex geometries and produce uniform coatings but often lead to porous or cracked films before sintering. The high-temperature post-treatments required for oxide electrolytes (>700–1000 °C) risk interfacial

degradation and limit compatibility with temperature-sensitive substrates. Achieving dense, uniform, and compositionally stable solution-derived layers remains a significant challenge [88].

2.4.1.3 2D Printing

Tape casting, screen printing, and inkjet or aerosol printing are also widely used for thin-film components and pilot-scale manufacturing. They offer scalability and integration into roll-to-roll systems but typically produce films thicker than 10 µm. The key limitation in TFASSBs, is post printing densification which often requires high-temperature sintering, which may compromise interfacial chemistry and mechanical integrity [94], [95], [96].

2.4.1.4 Summary of Challenges in Conventional TFASSB Manufacturing

Despite substantial progress in TFASSB research, conventional manufacturing routes still face critical scientific and engineering challenges that limit their scalability and practical deployment [30].

1. One of the most fundamental issues is the low areal capacity of vacuum-deposited electrodes, typically <1 mAh cm^{-2}, which falls significantly short of the ≥3–4 mAh cm^{-2} levels required for practical applications. Although thin-films enable fast ionic transport, their extremely small active mass per unit area fundamentally limits energy storage capability unless thicker or multilayer architectures are introduced both of which introduce additional challenges [97], [98].
2. A second limitation arises from the thickness–conductivity trade-off, where ultra-thin solid electrolytes (<1 µm) minimise ionic transport resistance but become prone to pinholes, cracking, and short-circuit pathways. Increasing electrolyte thickness improves mechanical robustness but results in higher internal resistance due to the relatively low ionic conductivity of many oxide solid electrolytes. Vacuum-based techniques such as sputtering and PLD can create dense, high-quality ultrathin films, but the resulting layers often require post-annealing at elevated temperatures that degrade interfacial chemistry or lead to unwelcome interphase formation [99], [100].
3. Interfacial stability remains one of the most severe bottlenecks. High-temperature processing used in sol–gel or CVD-derived films can trigger unwanted reactions between electrodes and electrolytes, forming resistive layers that increase charge-transfer resistance and degrade cycling stability.

Even in low-temperature vacuum processes, compositional drift (e.g., Li loss during sputtering or PLD) and stress accumulation caused by mismatched thermal expansion can result in delamination or poor adhesion, especially over larger areas [92] [101] [102] [103].

4. Cost and throughput constraints are also major barriers for industrial-scale adoption. PVD and ALD offer excellent thickness control but are limited by their inherently slow deposition rates (e. g. ALD often deposits only angstroms per cycle) making production times impractically long for large-area or multi-layer battery stacks. PLD, while ideal for stoichiometric transfer, is restricted by its small deposition footprint. Multistep vacuum processes further increase equipment complexity, energy consumption, and operational cost, reducing their suitability for high-volume manufacturing [104] [89].
5. Finally, film uniformity and reproducibility remain challenging across large substrates. Vacuum deposition techniques can suffer from local variations in film density, composition, and crystallinity, especially near substrate edges or when scaling from 1–2 cm² lab samples to wafer-scale formats. Solution-based or printed layers introduce additional challenges related to solvent evaporation, cracking, and porosity, often requiring high-temperature densification steps that are incompatible with integrated device manufacturing [105], [106], [107].

A comparison of the major thin-film manufacturing routes for TFASSBs including their benefits, limitations, and scalability considerations is summarized in Table 1.

Table 1. Comparison of Manufacturing Routes for SSTFBs based on the deposition methods discussed above

Deposition Method	Typical Film Thickness	Processing Temperature	Scalability	Film Density / Quality	Ionic Conductivity (S cm^{-1})	Key Advantages	Main Limitations
Sputtering (PVD)	0.1–5 µm	300–600 °C	Low–medium	Dense, uniform	10^{-6}–10^{-5}	High purity; good adhesion	Slow deposition; expensive
Pulsed Laser Deposition (PLD)	0.1–2 µm	400–700 °C	Low	Very dense, epitaxial possible	10^{-5}–10^{-4}	Precise stoichiometry control	Low throughput; small area
Sol–gel Coating	0.5–10 µm	400–800 °C	High	Moderate (porous unless annealed)	10^{-5}–10^{-4}	Low cost; tunable composition	Cracking, Li loss, shrinkage
CVD / ALD	0.05–1 µm	200–500 °C	Medium	Highly uniform, conformal	10^{-5}–10^{-4}	Atomic-scale control; excellent coverage	Costly; precursor handling
2D Printing (Screen / Inkjet / Spray)	2–200 µm	25–1000 °C (with post-sintering)	Very high	Dense after sintering	10^{-4}–10^{-3}	Scalable; patternable; cost-effective	Ink optimization; cracking; sintering needed

2.5 Thermal Spray as a Manufacturing Route for Thin-Film All-Solid-State Batteries

Thermal spray has emerged as a compelling alternative to conventional thin-film fabrication routes for TFASSBs, particularly in light of the challenges identified in Section 2.4, namely the limited scalability, high cost, slow deposition rates, and multi-step manufacturing associated with vacuum-based methods. Unlike sputtering, evaporation, or pulsed laser deposition, thermal spray techniques enable the direct deposition of ceramic, metallic, or composite thin-films at far higher deposition rates (10–100×), over large areas, and without the need for vacuum environments [108], [109]. These features position thermal spray as an attractive pathway for scalable production of battery components, where thickness, architecture, microstructure, and interface quality can be tailored through process control.

2.5.1 Thermal Spray fundamentals and Benefits

Thermal spray works on the principle that a raw material typically in the form of powder, wire, or liquid feedstock such as a suspension or solution precursor is injected into a heat source (combustion flame or plasma). This heat source melts or partially melts the feedstock, and the hot, accelerating gases then propel the molten or semi-molten particles toward the substrate. Upon impact, these droplets rapidly solidify to form splats, which are the fundamental building blocks of the coating. With subsequent passes, multiple splat layers stack to build a coating to the desired thickness. Typical coating thicknesses produced by thermal spray can range from a few tens of micrometres up to several millimetres, depending on the specific thermal spray process and processing conditions.

As a film or coating technology, thermal spray is widely regarded as one of the most versatile manufacturing methods for both thin and thick films and coatings [110], [111]. Key advantages include, for example:

- high deposition rates (often 10–100× faster than sputtering or PLD),
- the ability to coat large-area and non-planar surfaces,
- microstructural tunability, enabling dense to porous films via process control, and
- direct deposition of materials without binders or solvents.

Given these attributes, thermal spray offers a compelling, industry-ready framework for building TFASSB architectures with high speed and material versatility.

2.5.2 Why Thermal Spray for TFASSBs?

Thermal spray is particularly well suited for battery architectures that require ceramic thin-films with thicknesses from a few tens to several hundreds of micrometres, combined with strong adhesion, tuneable density, and compositional flexibility [14], [15]. Electrodes, solid electrolytes, and current collectors can be deposited sequentially into multilayer stacks, offering a binder-free, solvent-free, and potentially roll-to-roll manufacturable alternative to vacuum-based TFASSB technologies [112]. The method accommodates a wide range of feedstocks including oxides, spinels, garnets, phosphates, metals, and composite mixtures and allows local tailoring of porosity and crystallinity [113]. For materials such as LTO and LLZO, thermal spray provides a rapid route to form functional ceramic thin-films without conventional high-temperature sintering [114], [115]. The manufacturing of TFASSBs is traditionally dominated by vacuum-based thin-film deposition methods such as sputtering, pulsed laser deposition, and evaporation. While these techniques produce dense and compositionally well-controlled thin-films, their low deposition rates, high operational cost, small-area limitations, and poor scalability make them unsuitable for large-area or industrial TFASSB production [116], [117], [118]. These inherent bottlenecks motivate the search for alternative fabrication routes capable of delivering fast, scalable, and compositionally flexible ceramic thin-films requirements that thermal spray technologies are well positioned to address. However, the same high enthalpy and rapid quenching that make thermal spray versatile also introduce challenges such as lithium volatilization, secondary phase formation, surface roughness, and interface non-uniformity. These unresolved issues motivate the systematic study carried out in this thesis [114], [115].

2.5.3 Thermal Spray Variants Relevant to This Thesis

At its core, thermal spray involves heating and accelerating particles, either powders or liquid-borne droplets, toward a substrate where they impact, deform, and solidify to form a thin or thick film. Particle temperatures range from moderate (flame spray, HVOF) to extreme (plasma spray >10,000 K) [119], [120], [121], producing cooling rates of 10^4–10^6 $K \cdot s^{-1}$ [122], [123] that generate characteristic lamellar microstructures. For TFASSBs, these rapid solidification events strongly influence

phase formation, lithium retention, porosity, and interfacial bonding, thereby directly affecting ionic transport and electrochemical behaviour.

This dissertation focuses specifically on APS, SPS, and HVOF, three variants selected for their relevance to ceramic battery materials and their complementary thermal/kinetic characteristics (see figure 2).

2.5.3.1 Atmospheric Plasma Spray (APS)

APS employs a high-temperature plasma ($Ar/H_2/N_2$) to melt ceramic powders and deposit them as lamellar coatings. Particle temperatures exceed 10,000 K, enabling full or partial melting of oxides such as LTO and LLZO [114], [115]. APS provides high deposition rates, strong adhesion via molten splat formation, and microstructures that can range from dense to semi-dense depending on plasma power, gas flows, and standoff distance [124]. However, the high enthalpy environment in APS were shown to induce lithium volatilization and secondary phase formation, making it highly sensitive for Li-containing ceramics [114]. These thermal–chemical effects form a central theme of this thesis.

2.5.3.2 Suspension Plasma Spray (SPS)

SPS adapts plasma spraying for fine (submicron) particles dispersed in a liquid suspension. The solvent evaporates in-flight, enabling sub-micron particles to melt and form finely structured coatings. SPS offers improved microstructural refinement, smoother film morphology, and the capability to deposit thinner (5–20 µm) films than APS [125]. However, the high plasma enthalpy and the presence of liquid carriers can intensify Li loss, oxygen imbalance, and localized non-stoichiometry in lithium-based battery films. Several groups have demonstrated garnet-type (Li–La–Zr family) coatings by SPS and related liquid-feed plasma approaches [126].

2.5.3.3 High-Velocity Oxy-Fuel (HVOF)

HVOF relies on rapid combustion to generate moderate temperatures (~2000–3000 °C) but very high particle velocities (600–1000 $m \cdot s^{-1}$) [127]. There are no studies showing the use of HVOF for depositing Li-based thin or thick films. In general, the literature suggests that HVOF can effectively reduce volatilization of thermally sensitive materials and increase splat deformation and film adhesion, due to its lower thermal energy and higher kinetic energy compared with APS [128]. The same could be true for Li-containing battery thin films produced by HVOF.

2.5.3.4 Other

While not used experimentally in this thesis, several other thermal spray processes are relevant for future thermally sprayed TFASSB research. Solution Precursor Plasma Spray (SPPS) enables molecular-level feedstock control and direct in-situ oxide formation, making it highly promising for doped garnets and multi-cation oxides [129], [130], though challenges remain in controlling decomposition chemistry and avoiding Li loss. Cold Spray (CS) is a solid-state process ideal for ductile metals (Cu, Zn, Ni), making it attractive for current collectors and interlayers [131]; however, it cannot adequately deposit brittle ceramic electrolytes due to the high critical velocity requirements for oxide bonding. High velocity air fuel (HVAF) provides dense, low-oxidation coatings at lower temperatures, while low pressure plasma spray or vacuum plasma spray (LPPS/VPS) support controlled-atmosphere spraying [132]. Both are promising for phase-sensitive Li-bearing ceramics but require specialized infrastructure. Low-pressure/plasma-spray variants and hybrid vapor-phase plasma spray (PS-PVD) bridge the gap toward thinner, vapor-derived films and can reduce volatilization and oxidation for reactive Li compounds [126], [133], [134], [135]. These methods contextualize the broader thermal-spray landscape but remain outside the experimental scope of this dissertation.

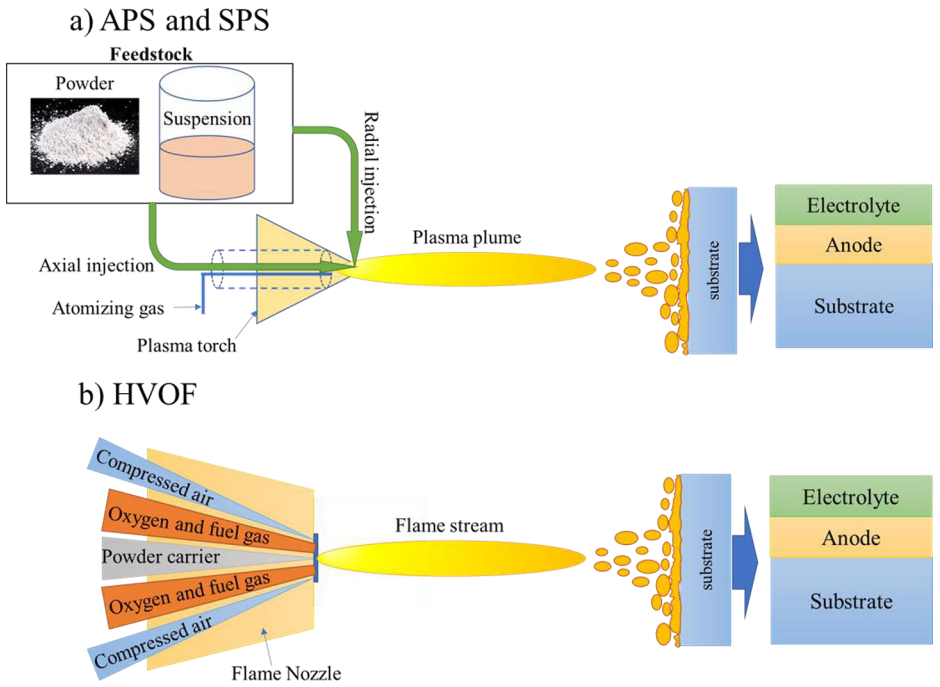

Figure 2. Schematics of (a) Plasma spray (APS and SPS) and (b) HVOF while depositing TFASSBs

Table 2. Summary of research on TFASSBs manufactured by thermal spray

Ref	Material / System	Thermal Spray Process	Substrate	Key Phases / Microstructure	Electrochemical Characteristics / Highlights
Liang et al., 2019 [136]	$Li_4Ti_5O_{12}$ (LTO)	APS (powder feed)	SS	Mixed LTO + TiO_2; lamellar	Exhibited ~1.55 V plateau; confirmed Li storage activity despite partial TiO_2.
Gopal et al., 2025 [114]	$Li_4Ti_5O_{12}$ (amorphous)	APS (rapid quench)	SS	Amorphous ~8 µm film	Structural relaxation after cycling; stable quasi-solid-state operation.
Mathiyalagan et al., 2025 [115]	$Li_4Ti_5O_{12}$ (LTO)	SPS (suspension feed)	SS	~76 wt % spinel LTO + minor TiO_2	Reversible lithiation/delithiation; binder-free thin-film validated SPS feasibility
Hasani et al., 2025 [137]	$Li_4Ti_5O_{12}$	SPS + synchrotron µXRD/ µXRF	SS-304	Spinel LTO dominant; $Li_2Ti_3O_7$ / Li_2TiO_3 near interface	Identified local Li depletion zones; emphasized need for process optimization.
Yost et al., 2023 [138]	TiO_2 / $Li_4Ti_5O_{12}$ dual layer	APS (powder feed)	SS foil	Nanocrystalline TiO_2 + spinel LTO	Demonstrated all-active-material electrode concept; tunable capacity by spray energy.
Hsueh et al., 2022 [139]	$LiCoO_2$ (LCO)	APS (high-deposition-rate)	Al foil	Layered structure partially degraded; recrystallized after anneal	Thick (>5 µm) LCO films; areal capacity > 5 mAh cm^{-2} after post-anneal.
Gopal et al., 2025 [114]	LTO, LLZO, NMC111	APS	Al	APS (multi-layer build)	Full stacks of all the constituents in SSB are made successfully by APS.
Lou et al., 2023 [140]	Si composite anode	Supersonic cold spray	Cu/Al	Work-hardened, dense Si-alloy splats	Viable Li-ion anode via solid-state spray; preserves chemistry
Zhang et al. (2016) [141]	$LiNi_{0.5}Mn_{1.5}O_4$ (LNMO)	HVOF	SS	Dense spinel/oxide structure; controlled volatility	Demonstrates viability of lower-enthalpy HVOF for spinel-type cathodes
Wu et al. (2023) [142]	$Li_7La_3Zr_2O_{12}$ (LLZO)	APS (large-area)	Al_2O_3	Cubic LLZO; dense ~300 µm film	$\sigma = 3.8 \times 10^{-5}$ S cm^{-1} (after anneal); flexural strength ≈ 157 MPa
Singh et al. (2025) [143]	$Li_{6.5}La_3Zr_{1.5}Ta_{0.5}O_{12}$ (LLZTO)	SPS (suspension)	SS 304	~68 % cubic phase; ~75 % crystallinity	$\sigma \approx 10^{-8}$ S cm^{-1} (as-sprayed); dense nanostructure
Sun et al. (2022) [144]	Li_3PO_4 (LPO)	APS	SS	Dense γ-LPO (< 1 % porosity); Li/P > 3	$\sigma \approx 4.6 \times 10^{-8}$ S cm^{-1}; γ-phase stability without post-anneal
Bu et al. (2025) [145]	$Na_3Zr_2Si_2PO_{12}$ (NASICON)	APS	Al_2O_3 plate	Dense single-phase Na-superionic conductor	Demonstrates spray feasibility beyond Li systems
Ockel et al. (2024) [146]	Cu metal (interlayer)	APS	LLZO	Dense, low-oxide Cu film	Robust low-resistance interface on garnet electrolytes

2.5.4 Limitations of Thermal Spray for TFASSBs

Thermal spray enables rapid deposition of ceramic and metallic thin-films with tunable microstructure; however, its application to TFASSBs is constrained by several scientific and engineering challenges:

1- **Phase stability:** Lithium evaporation and secondary phase formation (e.g., Li_2TiO_3, TiO_2, $La_2Zr_2O_7$, Li_2CO_3) occur under high enthalpy conditions [147]. In oxide systems such as LLZO, these processes reduce ionic conductivity and interfacial stability. High plasma temperatures and rapid quenching can therefore induce unwanted structural changes in both solid electrolytes and electrodes[148], [149] .

2- **Microstructural heterogeneity:** Uneven melting, splat boundaries, and heterogeneous porosity are intrinsic to rapid solidification in thermal spray.

These features create irregular Li^+ transport pathways and can generate localized mechanical stresses that affect long-term performance [88], [89].

3- **Surface roughness and interface impedance:** rough and porous interfaces hinder intimate solid–solid contact and increase interfacial resistance. Voids and micro-gaps formed during deposition limit Li^+ transport and may trigger dendrite formation or delamination during cycling. High interfacial impedance, frequently reported for sprayed LLZO and related electrolytes, stems from incomplete interfacial wetting and porosity [150], [151].

4- **Interfacial reactions, residual stresses, and adhesion:** High temperatures can trigger chemical interdiffusion at anode–electrolyte and electrolyte–cathode interfaces [152]. Thermal gradients and thermal expansion mismatch can lead to cracking or delamination, particularly in brittle ceramics [89].

These challenges highlight the need for post-deposition strategies capable of refining microstructure, stabilizing lithium-containing phases, and improving interface quality. The next section therefore examines thermal and laser-based post-processing routes that address these issues and enable optimization of TFASSB-relevant ceramic thin-films.

2.6 Post-Thermal Treatments and Laser Modification

Post-deposition processing plays a crucial role in modifying thermal-sprayed ceramic films; both at the surface and within the bulk to achieve dense, stable, and electrochemically efficient layers for ASSBs and other ceramic thin/thick-film applications. As-sprayed thermal-sprayed films often suffer from high porosity, surface roughness, and phase degradation due to rapid cooling, incomplete melting, and steep thermal gradients during deposition [153], [154]. To mitigate these effects, furnace-based thermal annealing and laser-assisted treatments are widely adopted as post-thermal modification routes aimed at enhancing surface smoothness, densification, crystallinity, and interfacial integrity.

A substantial body of literature reports the use of conventional furnace annealing to modify thermal-sprayed ceramic films across diverse application areas [155]. However, this number reduces significantly for laser post-processing (LPP), and the gap becomes even more evident in the context of battery materials. Specifically, for thermal-sprayed thin and thick films used in ASSBs, LPP remains virtually unexplored. Prior to this dissertation, no report existed on exploiting LPP as a post-thermal-treatment method for thermal-sprayed thin-film battery architectures which is a knowledge gap that strengthens both the novelty and motivation of this work.

Thermal annealing promotes grain growth, neck formation, and the removal of amorphous or defective phases, improving ionic conductivity and adhesion. Numerous studies demonstrate that post-annealing of oxide electrolytes and cathodes significantly reduces interfacial resistance and stabilizes the Li-ion conduction pathways [89], [156]. However, high-temperature annealing (>800–1000 °C) can induce lithium volatilization, oxygen loss, and the formation of secondary insulating phases such as, Li_2CO_3 or $La_2Zr_2O_7$, which deteriorate ionic conductivity and interface quality[157] [147].

In contrast, LPP offers a highly localized and rapid alternative [158]. Short laser pulses deliver concentrated surface heating, enabling controlled partial remelting, densification, and smoothening of rough coatings without globally heating the substrate [159]. This improves surface uniformity, adhesion, and phase stability and has been shown to significantly reduce interfacial impedance in oxide and sulfide solid electrolytes [160]. LPP enhances electrochemical performance by restoring crystallinity, suppressing decomposition, and forming denser interfaces in Li-conducting phases. Furthermore, the spatial precision of laser techniques enables selective surface structuring, graded interfaces, and engineered buffer layers that suppress interdiffusion and improve mechanical compatibility [161].

Combining moderate thermal annealing with targeted laser finishing offers a practical route to balance densification, chemical stability and interface quality. Recent studies even suggest integrating LPP directly into scalable roll-to-roll manufacturing lines for in-situ interface repair and densification during scalable battery production [154], [162].

While thermal annealing and laser post-processing can significantly modify microstructure and interface quality, their effects must be evaluated with techniques capable of resolving local structural and chemical changes. Conventional laboratory methods provide valuable but averaged information, necessitating advanced micro-scale probes. Section 2.7 therefore introduces the characterization framework used in this thesis, with a focus on synchrotron μXRD/μXRF.

2.7 Characterization Approaches

Conventional characterization techniques such as scanning electron microscopy coupled with energy-dispersive spectroscopy (SEM/EDS), X-ray diffraction (XRD), surface profilometry, and electrochemical testing are widely employed to investigate the morphology, phase composition, and electrochemical behavior of thermally sprayed thin and thick films. These laboratory-scale methods provide valuable insights into surface topography, averaged structural information, and overall material behaviour. SEM/EDS reveals microstructural features and elemental distributions, XRD identifies crystalline phases, and XPS probes surface chemical

states and oxidation levels. However, despite their utility, these techniques primarily offer surface-averaged or bulk-averaged information and lack the spatial resolution necessary to resolve local variations in chemistry or structure, especially across buried interfaces or through the film thickness [163], [164], [165]. As a result, they often cannot capture the micro-scale heterogeneity inherent to thermally sprayed films.

For thermally sprayed TFASSB components, understanding the structural and chemical evolution across solid–solid interfacesis particularly critical. Interfaces, such as those between the LTO films and metallic current collector (e.g., SS-304 substrate and Al), experience steep thermal and kinetic gradients during deposition. These gradients may induce localized phase transformations, diffusion-driven reactions, or compositional shifts that strongly influence electrochemical performance. Conventional methods fail to resolve such localized effects, they integrate signals over relatively large volumes and cannot distinguish micro-scale variations in phase composition or chemistry[166], [167] . Therefore, advanced characterization techniques with high spatial and depth resolution are essential to understand and overcome these challenges.

Synchrotron-based micro-X-ray diffraction (μXRD) and micro-X-ray fluorescence (μXRF) techniques provide such capability[166], [167] . These techniques enable micron-scale mapping of crystalline phases (μXRD) and elemental distributions (μXRF) across both the film thickness and buried interfacial regions. The high brilliance, tunable energy and small probe size of synchrotron radiation allow non-destructive interrogation of multi-layer ceramic–metal systems with exceptional depth sensitivity. When combined with X-ray photoelectron spectroscopy (XPS), which offers complementary surface-sensitive chemical information, this multi-scale suite of techniques provides a comprehensive view of phase evolution, elemental gradients, lithium chemistry, and interface reactions phenomena that remain largely inaccessible to conventional methods [168].

In particular, μXRD/μXRF scanning imaging delivers spatially resolved maps of both structural and chemical heterogeneity with micron-level precision, revealing subtle variations through the film thickness and directly at buried interfaces [169]. Such capabilities are essential for interpreting thermal-spray-induced transformations, phase gradients, and interdiffusion processes that govern the behaviour of LTO and LLZO thin-films.

Conventional SEM, EDS, and XRD remain important for establishing global trends but cannot resolve interfacial phenomena that critically influence performance of TFASSBs. This motivates the central role of synchrotron μXRD and μXRF in this dissertation. Accordingly, this work employs combination of laboratory-scale techniques (SEM, XRD, and XPS) together with synchrotron-based μXRD/μXRF mapping to investigate the thermally sprayed thin-films on metallic current

collectors in TFASSBs. The primary objective is to elucidate the local phase composition, elemental distribution, and interfacial chemistry within the film and across the film–current collector interface. Table 3 compares laboratory-scale and synchrotron methods whereas Figure 3 schematically illustrates the difference in probing volume between bulk XRD and localized µXRD.

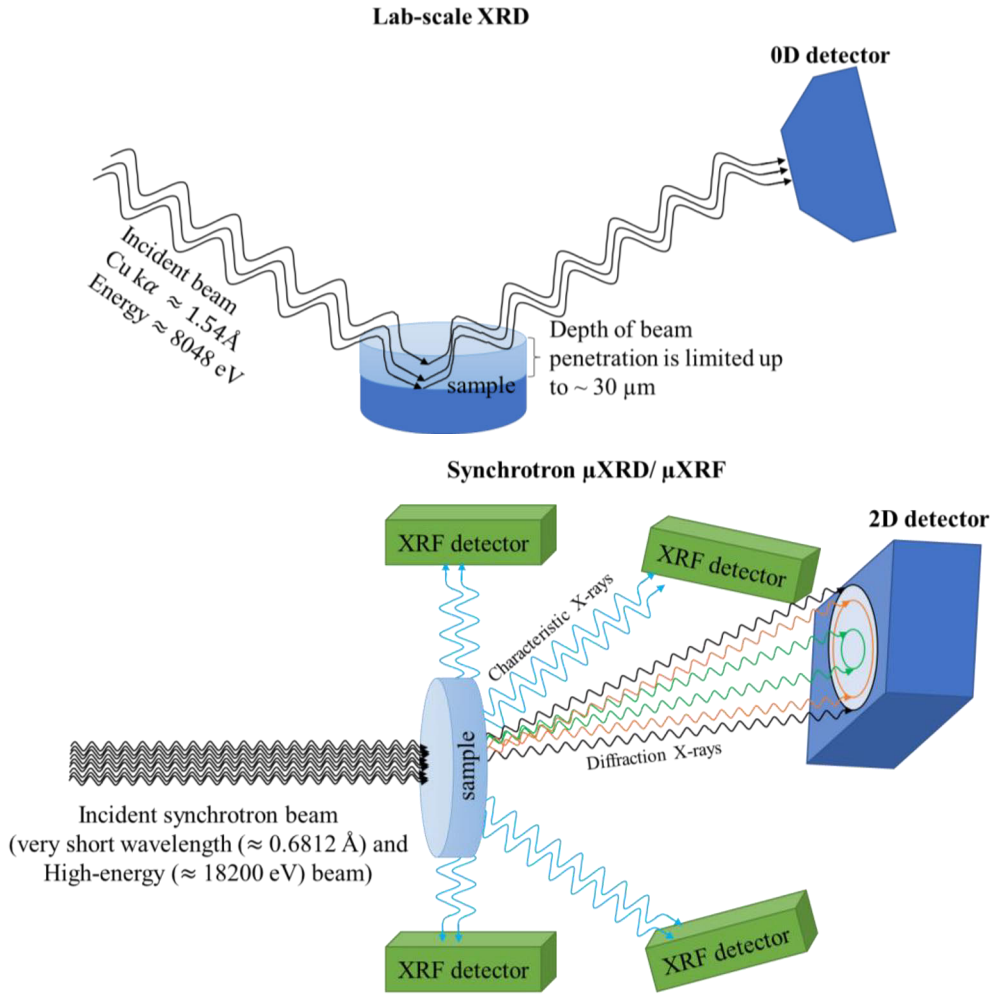

Figure 3. Schematic of lab vs synchrotron probing volumes (illustration showing bulk XRD averaging vs µXRD local spot).

Table 3. Comparison of lab-scale vs synchrotron techniques

Parameter	**Lab-scale Techniques** (SEM, EDS, XRD, XPS)	**Synchrotron Techniques** (μXRD, μXRF)
Spot size	• SEM/EDS: ~1–5 μm • Lab XRD: mm-scale footprint • XPS: ~100 μm	• μXRD/μXRF beam: 1 × 1 μm (focused)
Spatial resolution	• SEM: sub-μm • EDS: 1–2 μm • XRD: bulk-averaged, no spatial resolution • XPS: surface (nm-scale depth but large lateral footprint)	• μXRD: micron-scale phase resolution • μXRF: micron-scale elemental mapping
Information depth	• SEM: top surface • EDS: ~1–2 μm • XPS: a few nm (ultra-surface) • Lab XRD: few μm into surface (Cu Kα penetration, geometry dependent)	• μXRD/μXRF: 50–60 μm penetration depth, enabling through-thickness mapping of coatings and buried interfaces
Data type	• SEM: morphology • EDS: elemental composition • XRD: bulk-averaged phase composition • XPS: chemical states (surface-sensitive)	• μXRD: pixel-resolved phase identification & crystallography • μXRF: pixel-resolved elemental maps • Combined: correlated structural–chemical heterogeneity mapping
Strengths	• Fast • Accessible • Good for overall composition and morphology screening	• Non-destructive micro-mapping • Detects localized phases, gradients, and buried interfaces invisible to lab tools
Limitations	• Bulk-averaged • Cannot resolve local heterogeneity or buried features	• Requires synchrotron access • Lower throughput

The limitations of conventional characterization and the advantages of synchrotron micro-analysis directly inform the experimental approach of this dissertation. Chapter 3 outlines the materials, deposition parameters, post-processing conditions, and characterization methodologies employed to systematically investigate thermal-sprayed LTO and LLZO thin-films.

2.8 Research Gaps (RGs)

Despite significant progress in ASSB materials and thin-film manufacturing, several fundamental scientific gaps remain unresolved for thermally sprayed TFASSB architectures. The preceding sections (2.1–2.7) highlight limitations associated with conventional thin-film fabrication, thermal-spray-induced chemical/structural transformations, post-processing constraints, and the inadequacy of laboratory-scale characterization techniques to resolve local heterogeneity. These limitations give rise to three major research gaps that motivate this dissertation.

2.8.1 Research Gap 1 (RG1): Lack of fundamental understanding of process–structure–property relationships in thermally sprayed TFASSB constituents

Previous sections established that vacuum-based TFASSB methods suffer from poor scalability, whereas thermal spray offers high-rate, large-area deposition of ceramic thin-films. However, Sections 2.5 and 2.6 show that the extreme thermal gradients,

rapid quenching (10^4–10^6 $K \cdot s^{-1}$), kinetic effects during APS, SPS, HVOF, and substrate heat-dissipation effects; collectively induce lithium volatilization, secondary phase formation, heterogeneous porosity, rough interfaces, and non-uniform adhesion in LTO and LLZO films.

While numerous studies report feasibility of thermal-sprayed LTO/LLZO (Table 1), systematic, comparative, and mechanistic insights into how APS, SPS, and HVOF individually influence microstructure (lamellae, porosity, splat boundaries), phase stability (Li_2TiO_3, TiO_2, $La_2Zr_2O_7$, Li_2CO_3), lithium retention, and interface formation remain largely absent.

Thus, the first gap is the absence of a process-resolved understanding of how different thermal spray techniques govern phase evolution, microstructure, and interface integrity in ceramic TFASSB. This gap directly leads to Hypothesis 1, Sub-Objective 1, and RQ1.

2.8.2 Research Gap 2 (RG2): Limited understanding of how laser post-processing modifies thermal-sprayed LTO/LLZO microstructures and interfaces

As established in previous sections, especially section 2.6, thermal annealing improves crystallinity but suffers from high-temperature Li loss, formation of carbonate/pyrochlore secondary phases, poor scalability, incompatibility with metallic or flexible substrates.

LPP offers localized, rapid, and substrate-friendly remelting. However, LPP effects on densification, splat healing, microcrack closure, lithium chemistry recovery, and interface flattening in LTO/LLZO films, the mechanistic basis for phase restoration or suppression of plasma-induced phases, and the optimal balance between laser energy density and ceramic stability are poorly understood. Existing studies treat LPP as an auxiliary step, not as a scientifically interrogated microstructural engineering tool.

Thus, the second gap is the lack of mechanistic understanding of how LPP transforms the microstructure, chemistry, and interface quality of thermally sprayed TFASSBs. This gap directly leads to Hypothesis 2, Sub-Objective 2, and RQ2.

2.8.3 Research Gap 3 (RG3): Absence of spatially resolved, micro-scale characterization of phase, chemistry, and interfacial evolution in thermal-sprayed TFASSBs

Section 2.7 shows that conventional tools (SEM/EDS, XRD, XPS) average over bulk volumes, fail to capture buried interface reactions, cannot resolve through-thickness

phase gradients, cannot detect micron-scale lithium depletion zones, overlook microstructural heterogeneity inherent to APS/SPS/HVOF films.

Given the large thermal and chemical gradients in thermal spraying, the interfaces, especially LTO/metal and LLZO/metal, likely exhibit localized secondary phase bands, chemical diffusion layers, oxygen/lithium non-stoichiometry pockets, partially amorphous regions, residual stresses and microcracks. These features critically control interfacial resistance and electrochemical performance but remain invisible to conventional methods.

Synchrotron μXRD/μXRF offers micron-scale phase identification, lithium/transition metal mapping, non-destructive buried-interface probing, correlation of structural and chemical gradients. Yet, their application to thermal-sprayed TFASSBs remains extremely limited, and no study provides a comprehensive microstructure–chemistry correlation across spray-modified interfaces.

Thus, the third gap is the absence of high-resolution synchrotron-based mapping of localized phase evolution and elemental gradients in thermally sprayed TFASSB architectures. This gap directly leads to Hypothesis 3, Sub-Objective 3, and RQ3.

3 Materials and Methods

In this study, the experimental procedure consisted of several key steps. First, the raw powders and suspensions were procured. Second, the thermal spraying processes (HVOF, APS, and SPS) were carried out. Third, LPP was performed, and finally, various characterization techniques were applied. A flowchart illustrating the experimental workflow is shown in Figure 4.

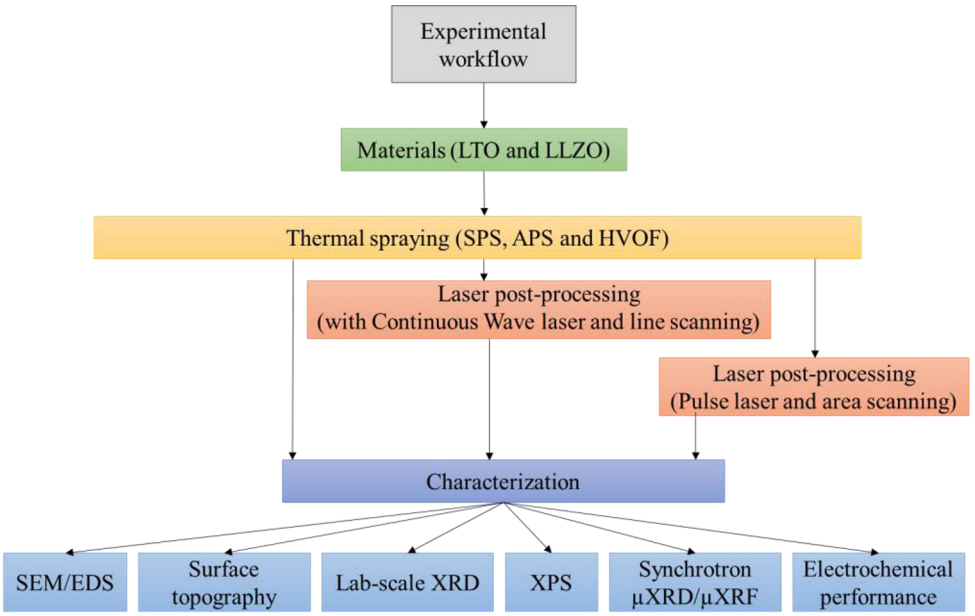

Figure 4. Flowchart of experimental workflow (materials → spraying → post-processing → characterization

3.1 Materials

Commercially available $Li_4Ti_5O_{12}$ (LTO) and $Li_7La_3Zr_2O_{12}$ (LLZO) powders were used as the primary ceramic feedstocks in this study for anode and solid electrolyte.

Lithium titanate ($Li_4Ti_5O_{12}$, LTO) powder was sourced from NEI Corporation (Franklin Township, NJ, USA). Two particle-size distributions of the same LTO material were employed depending on the thermal spray technique. For SPS, LTO

with d_{50} = 1.5–3.0 µm and purity > 99.9% was used to prepare the fine-particle suspension. Whereas for APS and HVOF the same LTO composition was used in powder form but with a larger particle size of d_{50} = 6–7 µm.

Lithium lanthanum zirconium oxide ($Li_7La_3Zr_2O_{12}$, LLZO) powder, supplied by Toshima Manufacturing Co., Ltd. (Japan), was used as the solid electrolyte feedstock. Cubic-stabilized LLZO powder was employed in powder form with with d_{50} = 5-10 µm and purity > 99.9% for APS deposition. Whereas for SPS, LLZO with d_{50} ~ 1 µm and purity > 99.9% was used to prepare the fine-particle suspension.

Two types of substrates were used to deposit thin-films which served as the current collector and deposition surface. For HVOF and APS deposited thin-films, commercial pure aluminum (Al) coupons with 25 mm diameter and 2 mm thickness, were used. For SPS, deposited thin-films, disk-shaped stainless steel (SS-304) substrates with 25 diameter and 2 mm thickness were used.

All powders and substrates were stored and handled under controlled humidity to minimize moisture uptake and surface carbonation, particularly crucial for LLZO.

Table 4 presents the chemical composition of the LTO and LLZO powders as obtained from energy-dispersive spectroscopy (EDS).

Table 4. Chemical composition of LTO and LLZO powders measured by EDS.

	Li	Ti	O	C	Ca, Si, Cl	Zr	La
LTO	nd*	54.4	45.2	-	0.4	-	-
LLZO	nd*	-	25.1	10.7	0.1	18.1	46.0

*Li is not detectable with the technique used)

3.2 Manufacturing and Post-Processing

The manufacturing workflow used in this thesis consisted of two sequential stages: (1) thermal spray deposition of LTO and LLZO thin-films using APS, SPS, and HVOF, and (2) LPP to modify surface morphology, densification, and interfacial quality. The detailed experimental parameters for each technique are provided in the appended publications and the subsections below summarize the essential manufacturing steps relevant to this dissertation.

3.2.1 Thermal Spraying

Three thermal spray techniques including APS, SPS, HVOF were employed depending on the desired microstructure, feedstock format, and experimental objective. Prior to spraying, all substrates were grit-blasted with 125 µm alumina and subsequently cleaned to ensure optimal adhesion.

3.2.1.1 Atmospheric Plasma Spray (APS)

APS was used to deposit LTO and LLZO thin-films. A Mettech Axial III high-power plasma torch (Northwest Mettech Corp., Vancouver, Canada) equipped with a G4™ Gravimetric Powder Feeder was used. Ceramic LTO powder (d_{50} = 6–7 µm) was injected axially into an $Ar/H_2/N_2$ plasma jet. The spray parameters employed for APS deposition of LTO are summarised in Table 5.

Table 5. Spray parameters for APS deposition

Nozzle size (inch)	Current (A)	Power (KW)	Enthalpy (kJ)	Gas Composition (%)	Gas flow rate (l/min)	Powder feed rate (g/min)	Stand-of-Distance (mm)	No. of Passes	Spraying time (cm^2/s)
5/16	150	73.2	6.7	80Ar-10 N_2-10H_2	280	30	130	4	20

3.2.1.2 Suspension Plasma Spray (SPS)

An Axial III high-power plasma torch equipped with a NanoFeed 350 suspension feeder (Northwest Mettech Corp., Vancouver, Canada) was employed for the SPS thin-film deposition. The process parameters used for depositing the LTO suspension are listed in Table 6. Multiple spray passes were sequentially applied to build up a thin-film with an approximate thickness of 40 µm. A suspension was prepared in deionized water containing 20 wt.% LTO powder and 1 wt.% 1-Methyl-2-pyrrolidinone (NMP) (Sigma-Aldrich) as an additive. The suspension was continuously stirred during spraying to prevent sedimentation.

Table 6. Spray parameters for SPS deposition

Suspension Feed (mL/min)	Total Gas Flow (L/min)	Power (kW)	Enthalpy (kJ)	Number of Passes
42	200	110	11	20

3.2.1.3 High-Velocity Oxy-Fuel (HVOF)

HVOF spraying was conducted using a DJ2700 gun (Oerlikon Metco) with propane as the fuel at the Thermal Spraying Engineering (TSE) facility in Malmo, Sweden. LTO powders (d_{50} = 6–7 µm) were deposited onto grit-blasted Al substrates.

3.2.2 Laser Post-Processing (LPP)

Two types of lasers including continoues wave (CW) laser and pulsed laser were used for laser post processing of selected APS- and SPS-sprayed samples to refine the surface, modify near-surface microstructure, and improve interfacial integrity.

3.2.2.1 Continuous-Wave (CW) Laser Processing

A 10 kW IPG Photonics YLS-10000-SM fiber laser (Marlborough, MA, USA) equipped with a PRECITEC YW52 optical head was used. The beam diameter remained constant at 1 mm, while power and scanning speed were varied to adjust energy density. Further details about the used experimental parameters of the fiber laser and optics are provided in Table 7.

Straight-line scan patterns were applied, with each line representing a distinct energy density condition. Lines were spaced sufficiently apart to avoid overlap, and the laser was activated 4 mm before reaching the sample to ensure steady-state beam conditions. More details can be found in the appended publications.

Table 7. The specifications of CW laser equipment

Laser YLS-10000-SM Class 4		**PRECITEC Optical Head YW52**	
Operating Wavelength (nm)	1070 ± 10	**Focal length collimation (mm)**	200
Mode of Operation	CW	**Focal length focusing (mm)**	400
Modulation Frequency (kHz)	0–5	**Magnification multiplier**	2
Power Tunability, %	10–100	**Beam diameter (µm)**	400
Power Stability, %	2	**Rayleigh length (mm)**	207.7
Laser Power [min–max] (kW)	0.08–10	**Processing speed [min–max] (mm/s)**	[0–50] (With robot)
Fiber Core Diameter, (µm)	200 (multi-mode)		

3.2.2.2 Pulsed Laser Processing

For the pulsed LPP, square-shaped areas (5 × 5mm) were scanned using the pulsed laser, and each square was treated under a distinct set of laser parameters. The key pulsed-laser variables include laser power, scanning speed, pulse frequency, and hatch distance. An IPG YLPN nanosecond pulsed fiber laser equipped with an integrated scanner head was used for LPP. The system offers a scanning area of 100 mm × 100 mm, operates typically at a wavelength of 1064 nm (1055–1075 nm range), provides a maximum output power of 100 W, and is configured with a focal length of 283 mm and a focal spot diameter of approximately 60 µm.

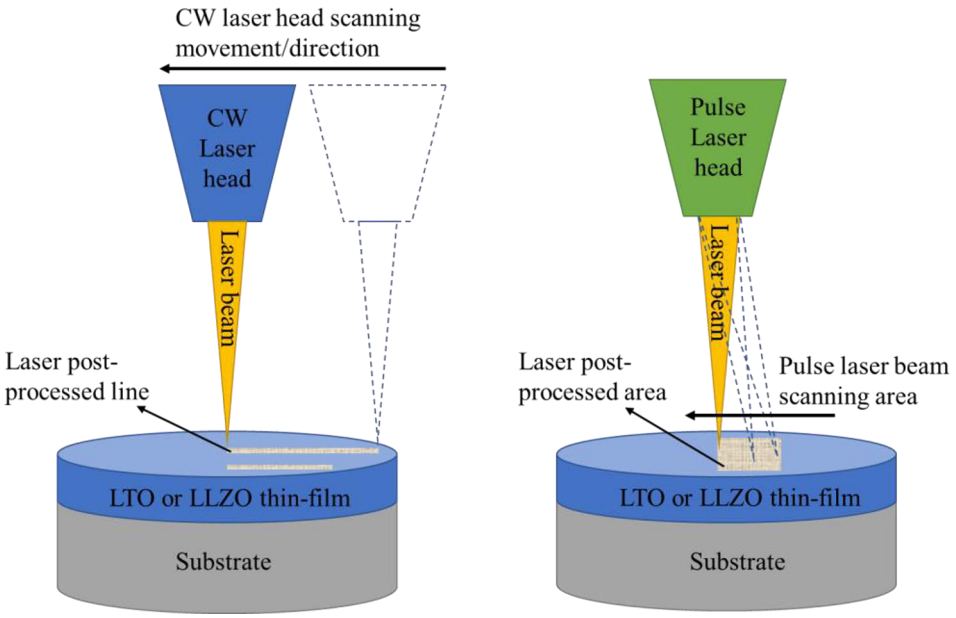

Figure 5. Schematic LPP using CW and nanosecond pulsed laser systems

Together, thermal spray deposition and laser post-processing establish a versatile processing framework to engineer the microstructure, phase stability, and surface quality of thermally sprayed LTO and LLZO thin-films. Full parameter sets and auxiliary experiments are detailed in the appended publications.

3.3 Characterization Workflow

A multi-scale characterization strategy was employed in this study, combining laboratory-scale techniques with large-scale synchrotron methods to evaluate the microstructure, chemistry, and phase evolution of the thermally sprayed and laser-processed thin-films. Specifically, scanning electron microscopy coupled with

energy-dispersive spectroscopy (SEM/EDS), X-ray diffraction (XRD), X-ray photoelectron spectroscopy (XPS), and electrochemical performance measurements were used as primary lab-based tools. These were complemented by high-resolution synchrotron-based micro-XRD (μXRD) and micro-XRF (μXRF) mapping to obtain spatially resolved structural and elemental information across the film thickness and film–substrate interface. Together, these techniques provided the necessary experimental framework to characterize the LTO anode and LLZO solid-electrolyte thin-films produced in this work.

3.3.1 SEM/EDS analysis

For powders and sample investigations, scanning electron microscopy was performed using an APREO field emission SEM (FE-SEM) system (Thermo Fisher Scientific, Waltham, MA, USA), equipped with an energy-dispersive X-ray spectroscopy (EDS) detector. SEM imaging was conducted at an acceleration voltage of 5 kV, while EDS analysis was carried out at 15 kV or 20 kV, depending on the sample requirements.

3.3.2 Surface topography

Surface topography and roughness were evaluated using the Alicona Infinite Focus G6 optical 3D measurement system (Bruker, Billerica, MA, USA), operated with MetMax software (version 3.0).

3.3.3 Lab-scale XRD

Laboratory-scale X-ray diffraction (XRD) analysis was performed using a Philips X'Pert PRO MPD diffractometer (Malvern Panalytical, The Netherlands). The samples were mounted on a metal sample holder and scanned over a 2θ range of 10°–90°. Measurements were conducted in θ–2θ Bragg–Brentano geometry using Cu Kα radiation (λ = 1.54 Å) at an operating voltage of 40 kV and a current of 50 mA. A PIXcel1D detector (Malvern Panalytical, The Netherlands) was used for data collection. Phase identification and data analysis were carried out using X'Pert HighScore Plus software (version 4.9). To enable synchrotron μXRD data analysis in the same software, specific adjustments were applied, including setting the wavelength to 0.68123 Å. Quantitative phase analysis, as presented in the pie charts, was performed using Rietveld refinement of the XRD patterns obtained from both μXRD and laboratory-scale XRD measurements.

3.3.4 Focused Ion Beam milling

A focused ion beam (FIB) was used to extract a microsample from the LTO thin-film for detailed microstructural analysis. The procedure employed a Xe^+ ion beam operated at 30 kV for milling and 12 kV for carbon deposition, allowing the manipulator to attach to the microsample for lift-out and subsequent mounting on a pin for synchrotron µXRD/µXRF measurements (see Figure 2). A detailed description of this procedure is provided appended publications [137].

3.3.5 Synchrotron µXRD/µXRF

The chemical composition and crystalline phases of the sample were analyzed using combined µXRF and µXRD contrast microscopy at the microXAS beamline of the Swiss Light Source (PSI) [170], as schematically illustrated in Figure 6. The µXRD data were collected with a Dectris Eiger 4M single-photon counting detector [171], while µXRF measurements were performed using four SDD detectors positioned around the sample. During raster scanning of the ceramic cross-sections, µXRD and µXRF data were simultaneously acquired using the detector configuration shown in Figure 6. The X-ray beam was focused to 1 µm, and the sample was scanned in 0.5 µm steps along both the x and y directions, with an acquisition time of 200 ms per point. Further methodological details can be found in Colldeweih et al. [172]. The X-ray beam wavelength was 0.6812 Å. Data were collected over an area of 250 × 200 µm with a resolution of 1 × 1 µm pixels and 0.5 µm scan steps. Azimuthal integration of the diffraction rings was performed using the pyFAI Python library [173], assigning each integrated diffraction pattern to a corresponding pixel in the scanned region and generating approximately 3000 XRD intensity maps at specific diffraction angles. Simultaneously, µXRF spectra were recorded for each pixel and processed with the PyMca software [174] to produce elemental distribution maps. Collectively, the µXRD and µXRF analyses provided complementary information on the structural and compositional characteristics of the sample.

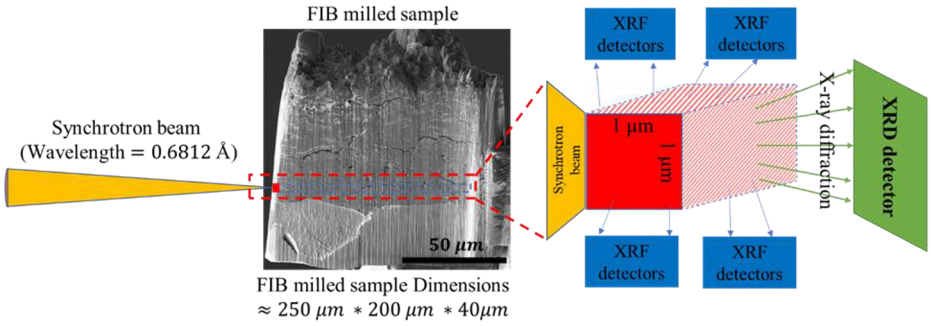

Figure 6. Schematic illustration of the synchrotron µXRD and µXRF measurements **[Publication II]**

3.3.6 X-ray Photoelecteron spectroscpy (XPS)

X-ray photoelectron spectroscopy (XPS) analysis was performed using a Thermo Fisher Nexsa (ESCA) system. For the survey scans, a step size of 1 eV was employed over a binding energy range of 0–1350 eV, while a finer step size of 0.1 eV was used for high-resolution scans of the core elements. The acquired XPS data were processed using Avantage software, and charge correction was applied by referencing the C–C bond peak.

3.3.7 Electrochemical characerization

For electrochemical characterization, all thermal sprayed TFASSB samples were laser-cut into disks with a diameter of 0.8 mm and subsequently dried in a vacuum oven at 100 °C for 24 h prior to cell assembly. The mass loading of the coated active material was maintained between 6–7 mg/cm². Cell assembly was carried out in an argon-filled glovebox using an ECC-Combi cell (EL-Cell) with lithium foil as the counter electrode, 140 µL of 1 M $LiPF_6$ in ethylene carbonate and dimethyl carbonate (v/v = 50/50, battery grade, Sigma-Aldrich) as the liquid electrolyte, and a Whatman GF/A glass microfiber filter as the separator. Cyclic voltammetry (CV), rate performance, and cycling tests were conducted within a voltage range of 1.0–2.5 V. For rate and cycling tests, the first cycle was performed at 0.05 C, followed by 10 cycles each at 0.1 C, 0.2 C, 0.5 C, 1 C, and 2 C, and then 150 cycles at 0.5 C. The C-rate was calculated based on the theoretical capacity of LTO (175 mAh g^{-1}). The applied current densities corresponded to the respective C-rates (1 C = 1.05 mA h). All electrochemical measurements were performed at room temperature (22 °C) using a Biologic BCS-805 cycler.

4 Results and Discussion

This chapter presents the main experimental findings of the thesis and discusses them in the context of thermally sprayed TFASSBs. Conventional lab-scale techniques are first used to establish baseline microstructural, phase, elemental, and surface-chemical characteristics of the thin-films. These are then complemented by large-scale synchrotron-based micro-characterization, which provides spatially resolved insight into local phase evolution and interfacial chemistry. Finally, the electrochemical performance of the thermally sprayed thin-films is discussed and correlated with the observed structure–phase relationships.

It is important to emphasize that optimization of the thermal spray processes was not the primary objective of this thesis. The thermal spray conditions used here were based on parameter sets developed elsewhere within the "GREEN-BAT" project consortium, of which this thesis is a part, and can be found in the corresponding publications [114], [115]. The focus in this chapter is therefore on comparative assessment and mechanistic understanding of the resulting thin-films, rather than on exhaustive optimization of process windows. Detailed experimental procedures and extended datasets are available in the appended papers **[Publication I-V]**.

4.1 Lab-Scale Assessment of Thermally Sprayed TFASSBs

This section summarizes the key findings obtained using lab-scale characterization techniques: surface profilometry and SEM for surface topography and microstructure analysis, XRD for phase analysis, EDS for elemental analysis, and XPS for surface chemistry analysis. Wherever relevant, as-sprayed thin-films are compared to laser post-processed ones to highlight the effect of LPP. LPP experiments were conducted primarily on APS and SPS thin-films of LTO and LLZO, and on LTO/LLZO double layers. HVOF thin-films were not subjected to LPP in this work; instead, they serve as an important baseline for comparing different thermal spray routes.

4.1.1 Surface Topography and Microstructure

4.1.1.1 As-Thermally-Sprayed Films

The surface and cross-sectional morphologies of the thermally sprayed LTO thin-films produced by HVOF, APS, and SPS are summarized in Table 8. The thickness for all three LTO thin-films measured are approximately 18 µm, 40 µm and 70 µm for LTO-HVOF, LTO-APS and LTO-SPS, respectively. HVOF thin-films exhibit well-flattened, compact splats with minimal unmelted particles and uniform lamellar stacking. This results in relatively low surface roughness (Sa ≈ 9.15 µm) and a smooth, continuous interface that supports strong adhesion to the Aluminium substrate.

APS LTO thin-films show coarser, irregular splats with partially melted particles and pronounced interlamellar ridges, leading to a higher surface roughness (Sa ≈ 11.79 µm) and a rougher interface. In contrast, SPS LTO thin-films, produced from a fine particle suspension, display fine, thin, well-spread splats and a dense microstructure, yielding the smooth surface (Sa ≈ 7.84 µm) and interface with SS-304 steel substrate[175].

Overall, these observations demonstrate that thermal energy input and particle state in each process strongly influence splat flattening, porosity, and interface roughness which are key factors governing integrity and suitability for thin-film battery applications **[Publication II].**

Table 8. Comparison of thermally sprayed LTO thin-films (HVOF, APS, SPS) in terms of film morphology and surface roughness.

Metric / Property	HVOF	APS	SPS
Thickness (µm)	~ 18	~ 40	~ 70
Surface roughness (Sa, µm)	9.15	11.79	7.84
Splat morphology	Well-flattened, compact splats with minimal unmelted particles; uniform lamellar stacking.	Coarse and irregular splats with partially melted particles and pronounced interlamellar ridges.	Fine, thin, well-spread splats; dense microstructure but possible columnar features due to fine suspension feed.
Interface roughness	Smooth and, continuous interface	Rougher interface	Smooth interface

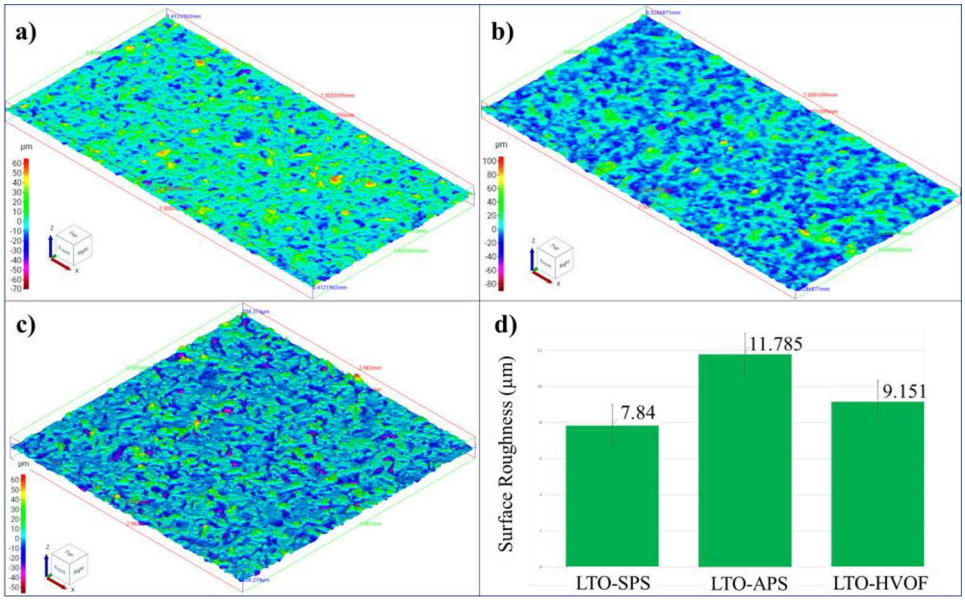

Figure 7. Surface morphology and surface roughness of thermally sprayed LTO coatings: (a) LTO-HVOF, (b) LTO-APS, (c) LTO-SPS, and (d) quantitative roughness comparison. LTO-SPS exhibits the smoothest surface (Sa ≈ 7.84 µm), followed by LTO-HVOF (9.15 µm) and APS (11.78 µm) **[Publication II]**.

For SPS-LLZO solid electrolyte, the measured thickness is approximately 40 µm and the as-thermally sprayed surface exhibits a relatively rough morphology (Sa ≈ 11.78 µm) with uneven topography and interlamellar boundaries typical of plasma-deposited ceramics **[Publication II]**.

4.1.1.2 Laser Post-Processed Films

LPP was used to modify the as-sprayed LTO-APS and LLZO-APS thin-films in two ways: line LPP (selected tracks) in **[Publication III and IV]** and full-area LPP (5 × 5 mm regions) **[Publication V]**. HVOF thin-films were not laser-processed in this work; instead, LPP studies focused on plasma-sprayed thin-films (APS & SPS), which exhibit higher initial roughness and stronger microstructural heterogeneity, making them more relevant targets for interface engineering and synchrotron-based micro-analysis.

For the LTO-SPS single layer thin-film, line-based LPP experiments showed that varying laser power and scanning speed produced markedly smoother laser-processed tracks compared to the as-sprayed thin-film surface. Table 9 lists the laser-processing variables, while figure 8 shows the laser-processed lines' positions and

geometry on the LTO-SPS single-layer thin-film and the average width of the laser-processed lines. Figure 8 shows how the average width of the laser-processed lines increases with energy density. The effect of laser power on line width is more pronounced than that of scanning speed.

Table 9. Laser post-processing variables for LTO-SPS **[Publication IV]**

Lines/ Codes	Laser Power (W)	Process Speed (mm/s)	Energy Input (J/mm^2)	Lines/ Codes	Laser Power (W)	Process Speed (mm/s)	Energy Input (J/mm^2)
a (line 1)	200	0.25	1019.1	i	80	0.5	203.8
b	200	0.5	509.5	j	80	1	101.9
c	200	1	254.8	k	80	2	50.9
d	200	4	63.7	l	80	4	25.5
e	200	16	15.9	m	80	8	12.7
f (line 2)	200	50	5.1	n	80	16	6.4
g	80	0.125	815.5	o	80	32	3.2
h (line 3)	80	0.25	407.6	**p (line 4)**	80	50	2.1

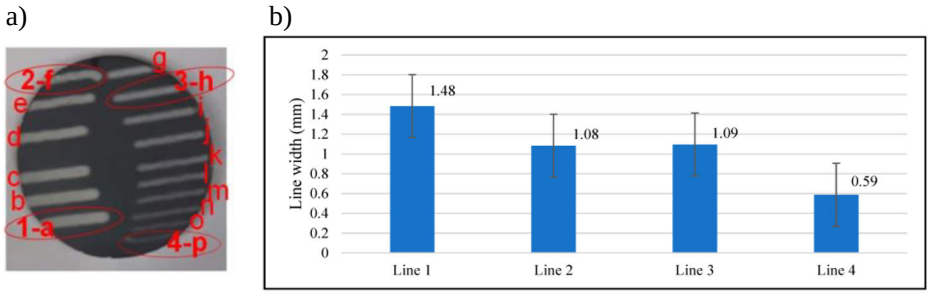

Figure 8. a) Laser post-processed lines' positions and geometry on the LTO-SPS single-layer thin-film, and b)The average width of laser-processed lines on the LTO-SPS single layer thin-film **[Publication IV]**.

Surface profilometry (Figure 9) confirmed the rough, hilly texture of the as-sprayed thin-films, typical of plasma-sprayed ceramics, caused by low-momentum droplets forming cauliflower-like structures. In laser post-processed regions, melting of hilltops and filling of valleys reduced the maximum roughness height from 238.3 µm to 96.9 µm, with Sa decreasing to 5.87 µm (line 2). Faster, low-power laser scans mainly interacted with hilltops, limiting heat diffusion and surface modification **[Publication IV]**.

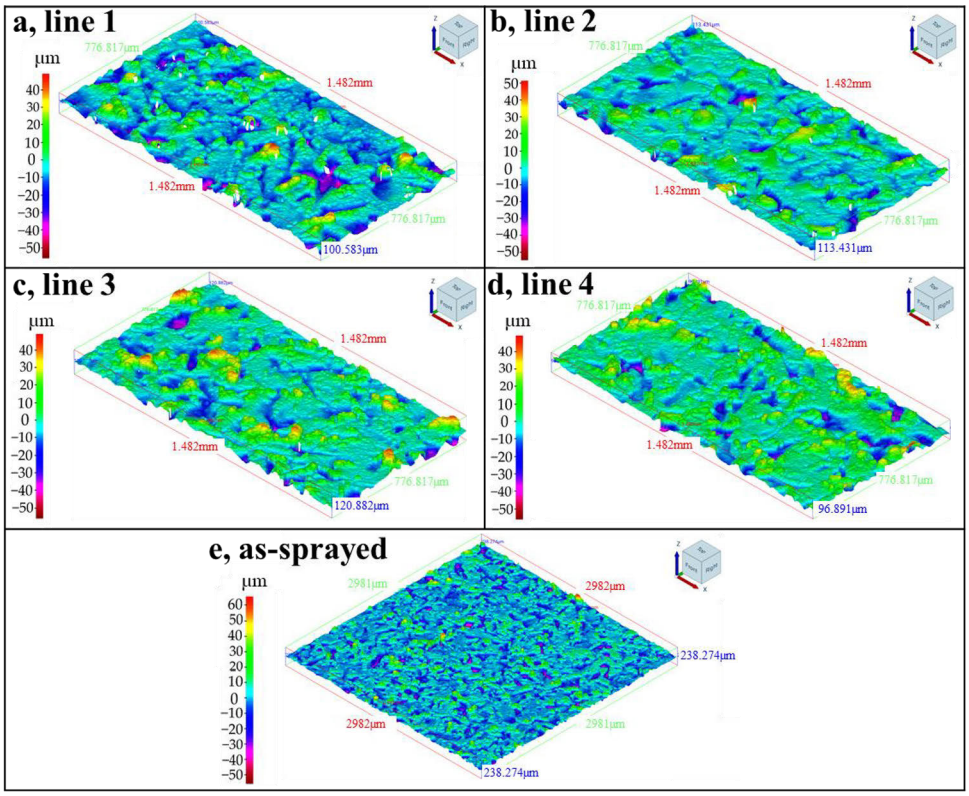

Figure 9. LTO-SPS surface topography imaged using optical profilometry from central area of laser-processed lines on plasma-sprayed sample: (a) line 1, (b) line 2, (c) line 3, (d) line 4, and (e) as-sprayed area (non-laser-processed) **[Publication IV]**.

Roughness variations correlate strongly with laser parameters. All laser-processed lines exhibit reduced Sa compared to the as-sprayed area, confirming that LPP effectively smoothens plasma-sprayed TFASSB films. At similar energy inputs, comparable Sa values were obtained, although topographical depths differed. For lines with equal speed but different powers, higher power increased roughness, indicating that excessive energy input can cause surface turbulence and spatter formation.

SEM analysis (Figure 10) further supports these findings: laser-processed zones show lake-shaped melted regions and partial pore elimination, while localized mud cracks form due to thermal stresses from rapid heating and cooling. Pits and pores are also observed, arising from trapped gas bubbles in the molten LTO which is typical of porous plasma-sprayed thin-films. At lower speeds or higher powers, localized overheating reduces melt viscosity, which leads to discontinuous melt pools. In the laser-processed regions, dense, flat equiaxed grains are evident, reflecting high solidification rates. This transition from columnar to equiaxed microstructure highlights the strong effect of laser-induced cooling dynamics on ceramic solidification [Publication IV].

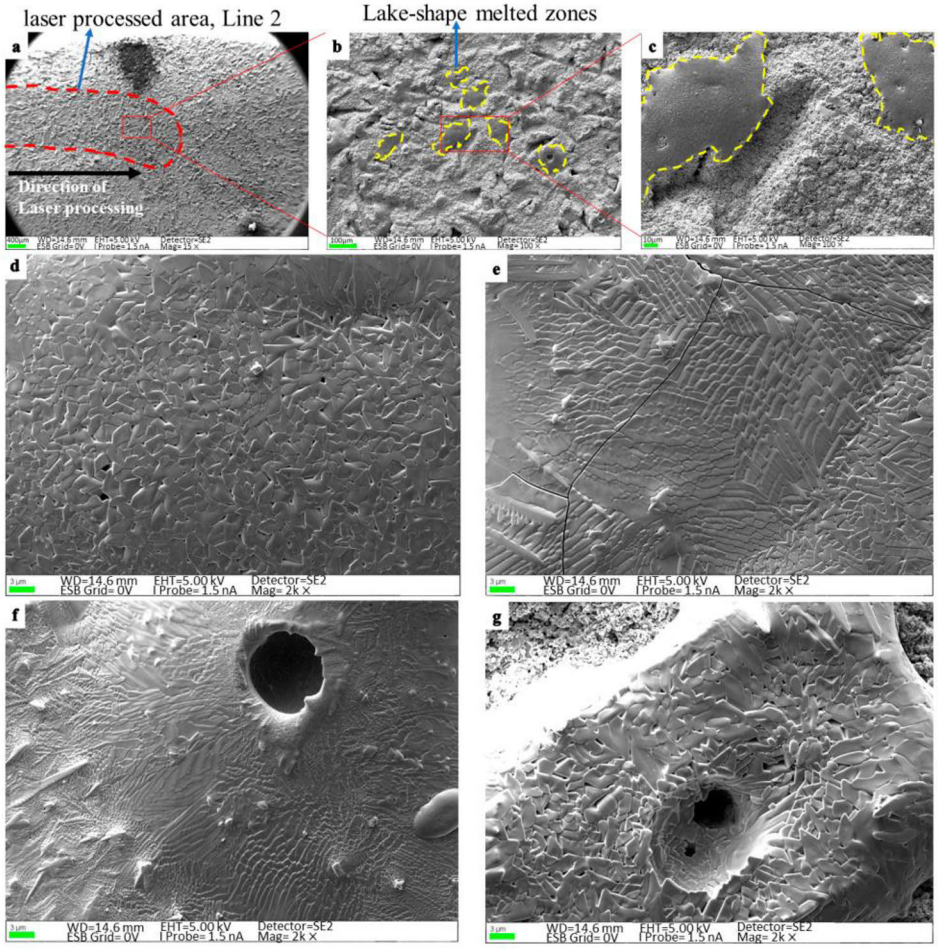

Figure 10. The surface topography of line 2 on the LTO-SPS laser-processed zone, (a) 16× mag., (b) 100× mag., (c) 500× mag., (d) 2k× mag., (e) presence of cracks, (f,g) pits **[Publication IV]**.

For the LLZO-SPS single layer, line-based LPP also significantly altered surface topography. According to Table 10 and Figure 11, among the 13 conditions applied, lines 1, 2, and 3 exhibited the lowest Sa and the largest roughness reductions (ΔSa ≈ 34.3%, 35.8%, and 39.5%, respectively) [**Publication III**]. These lines were continuous and uniform, unlike other low-energy tracks that appeared discontinuous or irregular. Among these three lines, increasing energy input further reduced roughness, primarily because a larger fraction of material melted. Lower scanning speeds allowed sufficient time for uniform solidification of molten regions, thereby minimizing surface roughness.

Table 10. LPP parameters, locations, and geometry of the processed lines on the LLZO-SPS thin-film single layer (blue-highlighted rows were characterized in detail) **[Publication III]**.

LLZO-SPS laser post-processing conditions											
Lines	Laser power (W)	Laser scanning speed (mm/s)	Energy input (J/mm^2)	Sa (µm)	ΔSa (%)	Lines	Laser power (W)	Laser scanning speed (mm/s)	Energy input (J/mm^2)	Sa (µm)	ΔSa (%)
L1	56	0.1	713.37	11.60	1.51	R1	111	5	28.28	7.75	34.17
L2	111	0.1	1414.01	8.64	26.63	R2	111	10	14.14	7.45	36.78
L3	111	1	141.40	8.12	30.48	R3 (line 3)	222	5	56.56	7.12	39.53
L4	167	1	212.74	7.89	33.04	R4 (line 2)	222	10	28.28	7.56	35.77
L5	222	1	282.80	9.11	22.66	R5	333	5	84.84	18.80	-59.60
L6	167	5	42.55	8.72	25.92	R6	333	10	42.42	10.66	9.45
L7 (line 1)	167	10	21.27	7.73	34.33	As-sprayed	-	-	-	11.78	0

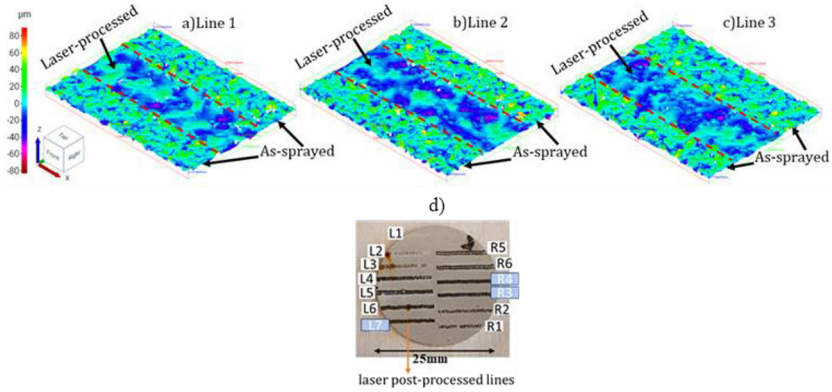

Figure 11. Surface topography of the central regions of laser-processed lines on LLZO-SPS thin-film, as measured by optical profilometry: (a) line 1, (b) line 2, and (c) line 3, and d) Laser post-processed lines' positions and geometry on the LLZO-SPS single-layer thin-film **[Publication III]**

After establishing line-based LPP on LTO-SPS and LLZO-SPS thin-films, full-area LPP using a pulsed laser was performed on LTO-APS and LLZO-APS thin-films **[Publication V]**. Several 5 × 5 mm² square regions were processed on LTO-APS single layers, followed by LLZO-APS single layer, and finally on LTO/LLZO-APS double-layer half-cell structures. The corresponding LPP parameter sets and samples schematics are summarized in Table 11 and figure 12.

Table 11. LPP parameters for LTO-APS single-layer samples (A-code), LLZO-APS single-layer samples (B-code), and double-layer LLZO/LTO-APS sample (C-code) **[Publication V]**

Sample	Scanning Speed (mm/s)	Frequency (kHz)	Laser Power (W)	Hatch Distance (mm)
A-1	5	100	5	0.05
A-2	5	100	2.5	0.05
A-3	2.5	100	5	0.05
A-4	2.5	100	2.5	0.05
A-5	5	25	5	0.05
A-6	2.5	25	5	0.05
A-7	5	100	5	0.075
A-8	5	100	5	0.025
B-1	5	100	10	0.05
B-2	5	100	7.5	0.05
B-3	2.5	100	10	0.05
B-4	2.5	100	15	0.05
B-5	5	25	10	0.05
B-6	2.5	25	15	0.05
B-7	5	100	10	0.075
B-8	5	100	10	0.075
C-1	5	100	10	0.05

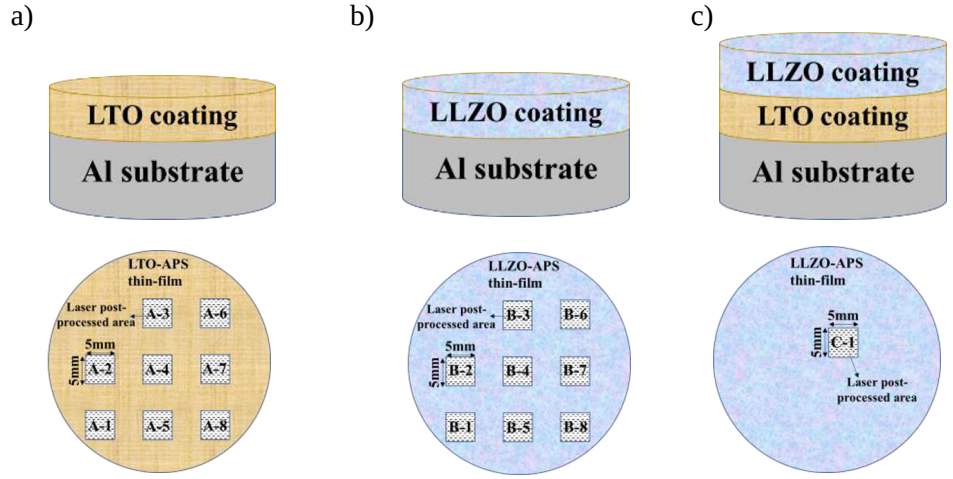

Figure 12. Laser post-processing schematics for APS samples a) LTO-single layer, b) LLZO-single layer, and c) LLZO/LTO double-layer **[Publication V]**

As shown in Table 12, surface roughness measurements show that pulsed-laser processing can substantially reduce surface irregularities, but the outcome depends strongly on laser parameters. Poorly chosen conditions can even increase roughness, whereas an optimized combination (such as 5 mm/s scanning speed, 100 kHz frequency, 10 W power, and 0.05 mm hatch distance) reduced roughness by up to 41.5%, 31.2%, and 40.2% for samples A, B, and C, respectively. Under these conditions, Sa decreased to 4.2 µm (B-1) and 2.75 µm (C-1), representing significant improvements over the as-sprayed states (Table 12). Overall, higher frequency emerged as the strongest factor for achieving a uniform energy distribution and suppressing defects, while laser power, scanning speed, and hatch distance all contributed to obtaining a clean, fully melted, and evenly levelled surface.

Table 12. Surface roughness comparison of pulsed-laser post-processed areas and as-sprayed thin-films **[Publication V]**

Region	**A-1**	**A-2**	**A-3**	**A-4**	**A-5**	**A-6**	**A-7**	**A-8**	**A-as-sprayed**
Sa (µm)	5.70	11.56	6.12	6.68	9.35	7.93	6.17	5.96	9.75
Region	**B-1**	**B-2**	**B-3**	**B-4**	**B-5**	**B-6**	**B-7**	**B-8**	**B-as-sprayed**
Sa (µm)	4.20	9.20	5.12	7.37	9.17	11.34	4.85	4.30	6.11
Region	**C-1**								**C-as-sprayed**
Sa (µm)	2.75								4.60

As shown in Figure 13, the initially porous as-sprayed LTO-APS and LLZO-APS thin-films become significantly denser after remelting, with a clear reduction in thin-film thickness indicating densification. In the LTO/LLZO-APS double-layer thin-film architecture, laser remelting not only densifies the top LLZO thin-film layer but also enhances interfacial bonding with a LTO thin-film layer below, yielding a more cohesive microstructure.

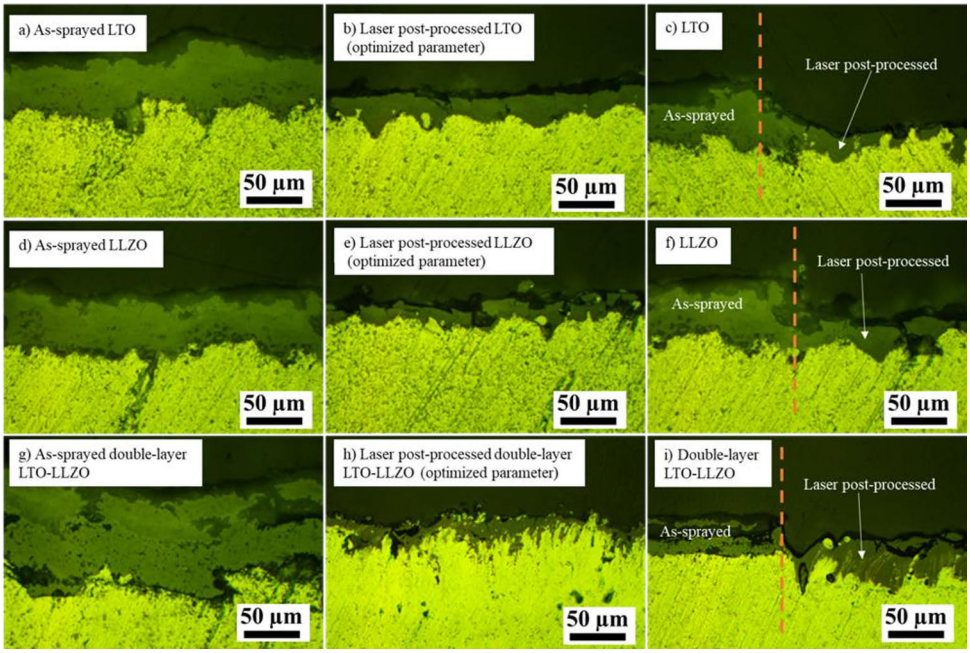

Figure 13. Cross-sectional images of (a) as-sprayed LTO-APS, (b) laser-remelted LTO-APS (best LPP parameters), (c) transition from as-sprayed to laser-remelted region showing thickness reduction, (d) as-sprayed LLZO-APS, (e) laser-remelted LLZO-APS (best parameters), (f) corresponding transition, (g) as-sprayed LLZO/LTO-APS double layer, (h) laser-remelted LLZO/LTO-APS double layer (best parameters), and (i) transition indicating thickness decrease **[Publication V]**.

4.1.2 Phase Assessment via XRD

4.1.2.1 As-Thermally-Sprayed Films

Conventional lab-scale XRD was used to identify and quantify the crystalline phases present in the thermally sprayed LTO thin-films (Figure 14). Because Cu Kα radiation (~1.54 Å) primarily probes the near-surface region (a few micrometres, depending on density, beam angle, and porosity), the resulting patterns mainly reflect the surface layers, which are most affected by oxidation, cooling gradients, and post-deposition reactions. Figure 11 shows that all LTO thin-films contain a mixture of

spinel $Li_4Ti_5O_{12}$ (LTO), monoclinic Li_2TiO_3, and minor TiO_2 (tetragonal/anatase) phases, with their relative fractions varying by process route. Quantitative analysis reveals:

- LTO-APS: ≈ 81.2% Li_2TiO_3, ≈ 16.9% LTO, minor TiO_2
- LTO-SPS: ≈ 72.7% Li_2TiO_3, ≈ 25.9% LTO, ≈ 1.4% TiO_2
- LTO-HVOF: ≈ 60% LTO, ≈ 31% Li_2TiO_3, negligible TiO_2

Weak Li_2CO_3 peaks appear only in the LTO-HVOF sample, attributed to post-deposition reaction of Li_2TiO_3 with atmospheric CO_2 according to:

$$Li_2TiO_3+CO_2 \rightarrow Li_2CO_3+TiO_2$$ [176] Equation1

Such carbonate formation is well known in Li-based ceramics exposed to ambient conditions and can degrade electrode kinetics due to the insulating nature of Li_2CO_3. Weak metallic Al reflections in the LTO-APS and LTO-SPS patterns indicate partial diffraction from the underlying substrate, consistent with thinner or more porous layers.

Overall, the lab XRD trends show that LTO-HVOF best preserves the parent spinel phase, LTO-SPS exhibits intermediate decomposition, and LTO-APS displays the highest degree of phase transformation correlating with increasing thermal input and particle residence time in the plasma jet. These findings demonstrate that higher process enthalpy promotes lithium volatilization and phase decomposition, while lower thermal exposure and rapid quenching (LTO-HVOF) more effectively maintain the LTO spinel structure **[Publication II]**.

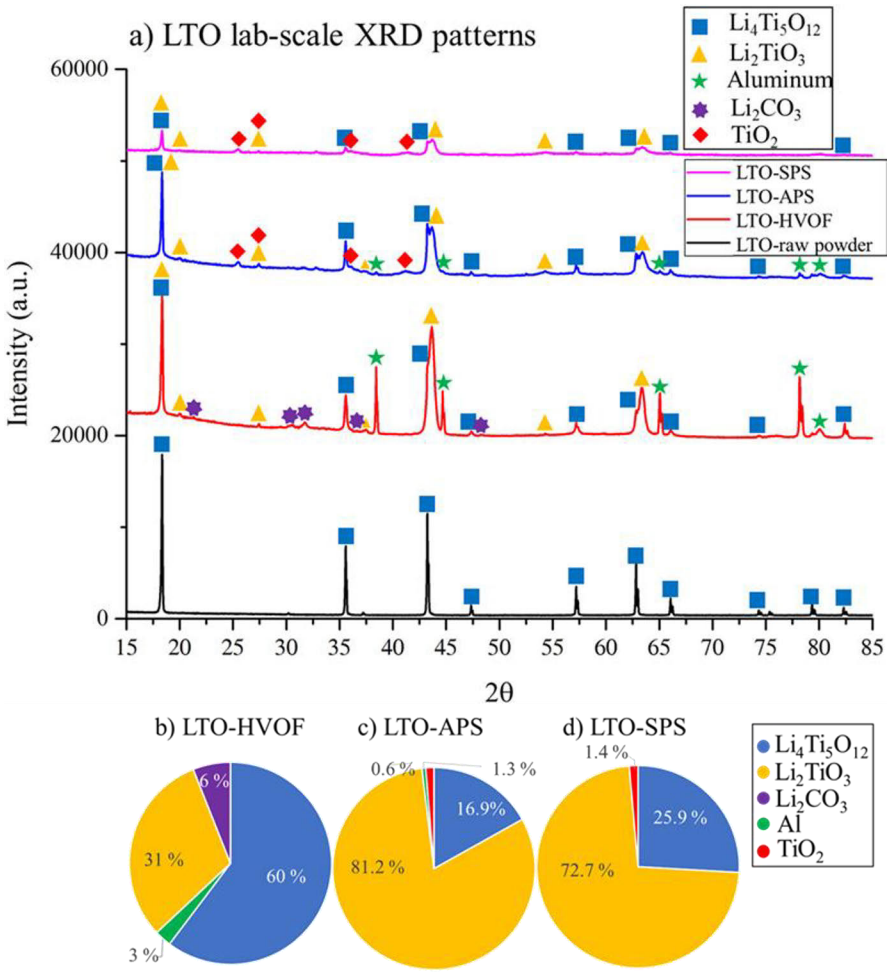

Figure 14. Lab-scale XRD patterns of LTO thin-films and feedstock. Feedstock = 100 % LTO; LTO-HVOF retains ≈60 % LTO, LTO-APS ≈16.9 %, LTO-SPS ≈25.9 %. Li_2CO_3 traces appear only in LTO-HVOF due to post-spray CO_2 uptake. Lower enthalpy and faster quenching favor spinel preservation **[Publication II].**

4.1.2.2 Laser Post-Processed Films

Lab-scale XRD was not systematically performed on all pulsed-laser-processed LTO and or LLZO thermally sprayed thin-film samples in this thesis; instead, phase evolution after LPP, particularly in LLZO-SPS thin-films, was primarily assessed using synchrotron µXRD, as discussed in Section 4.2.1.2. For LLZO-SPS, XRD patterns from laser-processed lines and unprocessed regions are presented and interpreted in the context of laser-induced phase changes in Section 4.2.1.2 (Figure 25).

4.1.3 Elemental Assessment via EDS

4.1.3.1 As-Thermally-Sprayed Films

In the context of this thesis, EDS was mainly used in a comparative manner, examining local compositional changes between as-sprayed and laser post-processed regions, rather than establishing exhaustive baseline compositions. For both LTO-SPS and LLZO-SPS thin-films, EDS of neighbouring as-sprayed regions serves as the reference to interpret LPP-induced chemical modifications.

4.1.3.2 Laser Post-Processed Films

For the LTO-SPS single-layer thin-film, EDS results clearly show that LPP influences elemental distribution (Figure 15 and Table 12) **[Publication IV]**. Although Li cannot be detected by EDS, titanium and oxygen were consistently observed in both as-sprayed and laser-processed regions, indicating that the main spinel-related metal elements remain present. In the laser-processed regions, Ti content was slightly lower and C content slightly higher than in the as-sprayed regions. Oxidation occurred due to processing in ambient air, increasing oxygen content; thus, using inert or vacuum atmospheres is recommended for future work. In the laser post-processed zone, lake-shaped melted regions exhibited higher C and lower Ti content, likely due to local alloying effects and the preferential melting of carbon-rich areas.

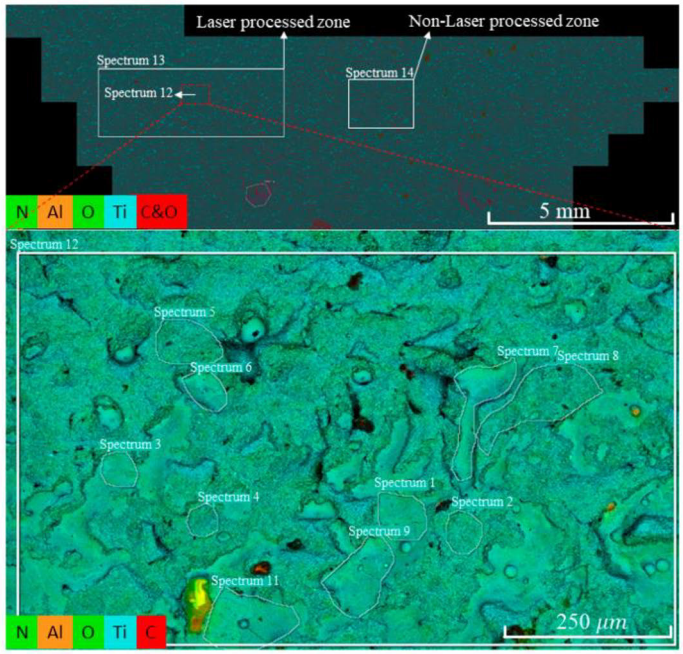

Figure 15. Elemental mapping of LTO-SPS laser-processed and non-laser-processed zones in line 1. Multiple localized spectra were recorded within the analysed region of Spectrum 12 **[Publication IV]**.

Table 13. Elemental composition of different zones in line 1 of the LTO-SPS single-layer thin film (Li not detected).

			Ti (wt%)	O (wt%)	C (wt%)
Non-laser processed (As-sprayed area)	Spectrum 14		59.5	35.6	3.3
Laser processed area	Spectrum 12		55.0	37.8	6.5
	Lake-shape melted zones	Spectrum 1	51.0	39.5	9.5
		Spectrum 3	52.0	38.2	9.8
		Spectrum 6	55.2	35.1	9.7
		Spectrum 7	56.1	36.5	7.4
		Spectrum 9	55.3	35.6	8.5
		Spectrum 11	53.3	37.6	8.7
		Average composition	53.8	37.1	8.9
	Non-melted zones	Spectrum 2	54.6	41.8	3.6
		Spectrum 4	54.8	39.2	6.0
		Spectrum 5	54.0	39.8	6.2
		Spectrum 8	55.3	38.8	6.0
		Average composition	54.7	39.9	5.4

For the LLZO-SPS single layer thin-film, EDS analysis (Figure 16) reveals that LPP significantly alters elemental distribution between laser-processed and as-sprayed regions. In all three laser-processed lines, localized heating promotes surface oxidation, as evidenced by increased oxygen content, while Zr and La concentrations decrease, likely due to oxidation, diffusion, or volatilization at high temperatures. These compositional changes indicate that laser processing not only smoothens the surface but also modifies local chemistry, which may influence interfacial and electrochemical behaviour of LLZO-SPS solid electrolytes **[Publication III]**.

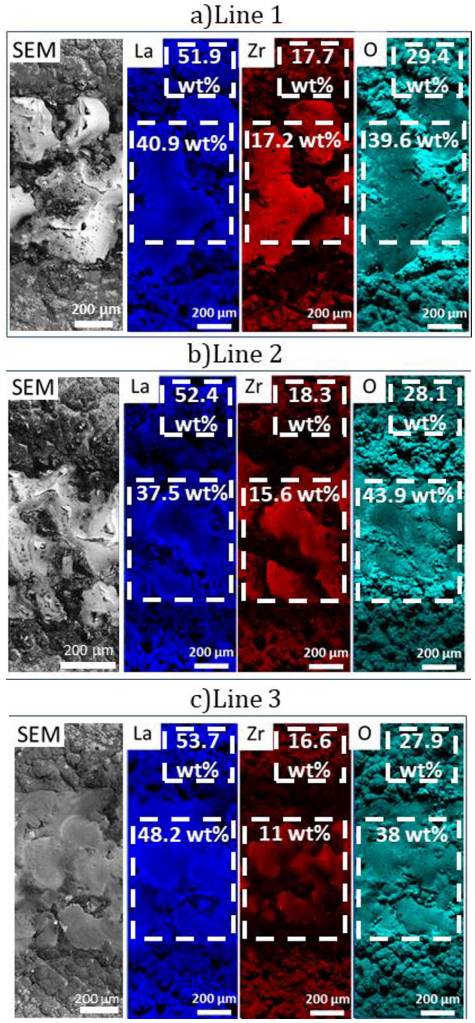

Figure 16. SEM images and corresponding EDS elemental maps for O, Zr, and La for all three laser-processed lines in the LLZO-SPS single-layer thin-film. Chemical compositions of laser-processed and neighbouring as-sprayed regions are shown in dashed boxes **[Publication III].**

In addition to surface profilometry, SEM surface topography and SEM cross-sections demonstrate that whole-surface LPP densifies and restructures the thin-film interior. As illustrated in Figure 17, the as-sprayed LTO-APS and LLZO-APS thin-films exhibit typical plasma-sprayed features such as pronounced peaks and valleys, mud-crack networks, and splat boundaries. After LPP, these features are largely remelted and levelled: sharp asperities are rounded, crack opening is reduced, and the surface appears more continuous, in agreement with the measured decrease in Sa. For the LTO/LLZO-APS half-cell, LPP similarly transforms the initially rough, cauliflower-like surface into a smoother landscape of remelted regions and shallow residual undulations, indicating more uniform wetting and improved potential contact with counter-electrodes [**Publication V]**.

For full-area pulsed LPP on APS thin-films (LTO, LLZO, and LTO/LLZO double-layer), surface topography and EDS again confirm that LPP smoothens as-sprayed surfaces and restructures local chemistry. For LTO-APS, laser-post-processed regions show remelted zones and solidification cracks, while EDS confirms persistent Ti and O with slightly increased C (surface reactions) (see Table 14). For LLZO-APS, laser post-processing generates numerous spherical or semi-spherical remelted particles and, in some regions, removes parts of the thin-film; EDS registers Zr and La with oxygen increasing from 33.4% to 44.2%, indicating preferential oxidation (see Table 15). In the LTO/LLZO-APS double layer, large bumpy features are replaced by smoother remelted particles, though localized holes appear due to beam penetration; EDS still detects Zr and La in both as-sprayed and laser-processed regions **[Publication V].** These trends are visualized in Figure 18 and Tables 14 and 15, which compares EDS elemental maps of as-sprayed and LPP-processed LTO-APS, LLZO-APS, and LTO/LLZO-APS half-cell thin-films.

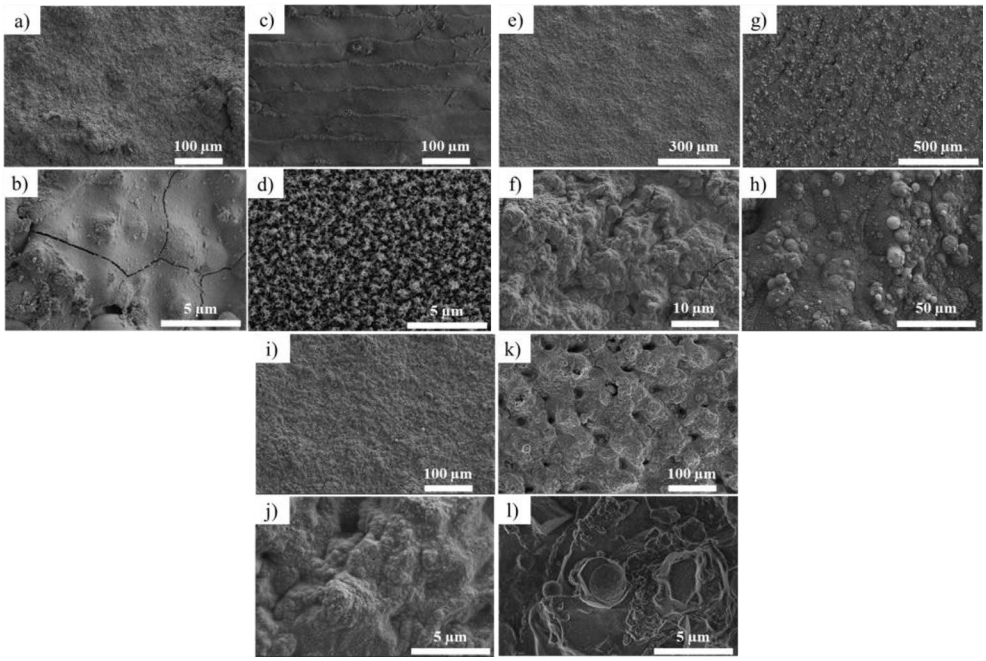

Figure 17. SEM images of as-sprayed LTO-APS (a and b), LLZO-APS (e and f), and LTO/LLZO-APS half-cell (i and j), and their corresponding LPP-processed counterparts LTO-APS (c and d), LLZO-APS (g and h), and LTO/LLZO-APS half-cell (k and l). **[Publication V].**

Table 14. Elemental composition of the black-highlighted spectrums in the single-layer LTO thin-film for the as-sprayed and laser post-processed samples **[Publication V]**.

	Ti	**O**	**C**
As-sprayed region (obtained from selected spectrum) (wt %)	51.9	44.1	4.0
Laser post-processed region (obtained from selected spectrum) (wt %)	42.3	51.2	6.5

Table 15. Elemental composition of the black-highlighted spectrums in the single-layer LLZO thin-film for the as-sprayed and laser post-processed samples **[Publication V]**.

	La	**Zr**	**O**	**C**	**Al**
As-sprayed region (obtained from selected spectrum) (wt %)	39.8	12.9	33.4	13.9	0
Laser post-processed region (obtained from selected spectrum) (wt %)	28.2	10.4	44.3	14.5	2.6

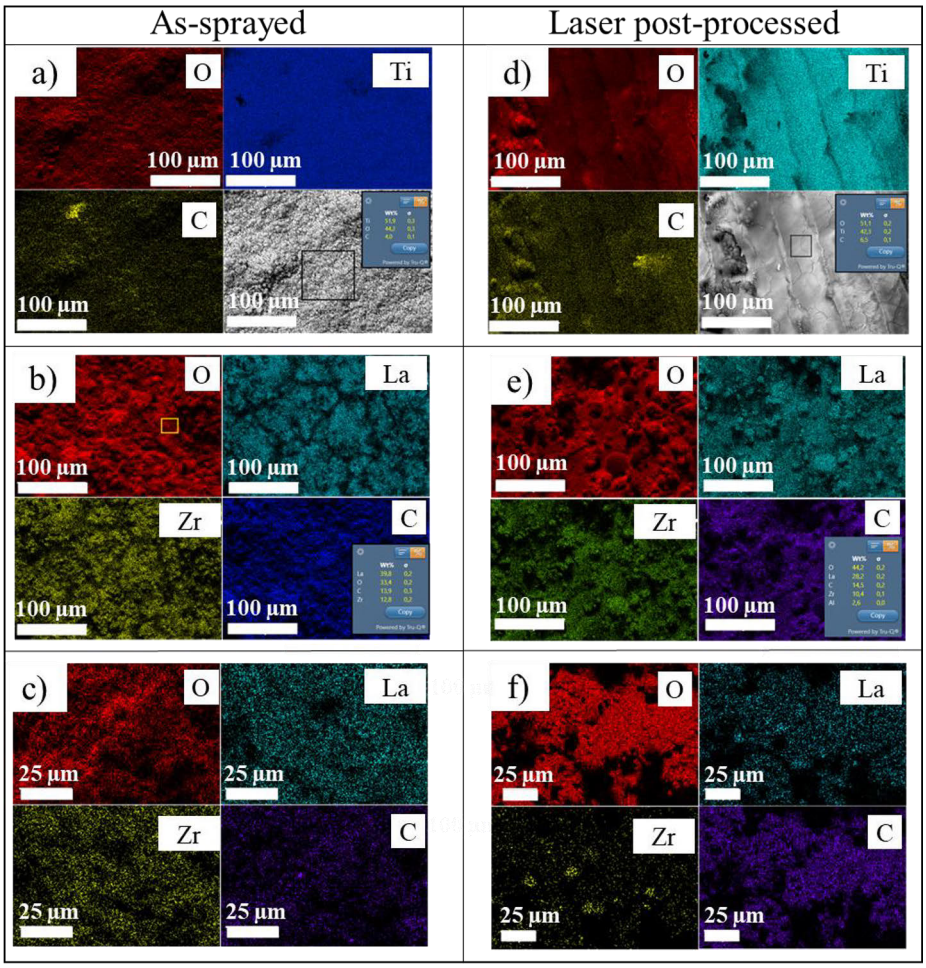

Figure 18. EDS mapping of SEM pictures shown above showing as-sprayed LTO-APS (a), LLZO-APS (b) and LTO/LLZO-APS half cell (c), and their corresponding LPP-processed counterparts LTO-APS (d), LLZO-APS (e) and LTO/LLZO-APS half cell (f) **[Publication V]**.

Together with the SEM topography and cross-sectional observations in Figure 17 and Figure 13, respectively, these EDS results confirm that LPP densifies and restructures the thin-films, while also inducing oxidation and occasional localized damage, depending on composition and laser–material interaction.

4.1.4 Surface Assessment via XPS

4.1.4.1 As-Thermally-Sprayed Films

XPS was used to assess surface lithium and carbon chemistry in the LTO thin-films produced by HVOF, APS, and SPS (Figure 19, Li 1s and C 1s spectra). For LTO-HVOF, the Li 1s peak at 56.5 eV indicates Li_2CO_3, while LTO-APS shows a slightly lower binding energy at 56.06 eV, also consistent with carbonate species. The higher Li 1s binding energy in LTO-HVOF suggests stronger Li_2CO_3 contributions at the surface. In contrast, LTO-SPS exhibits no detectable Li 1s peak, indicating severe lithium depletion at the surface **[Publication II]**.

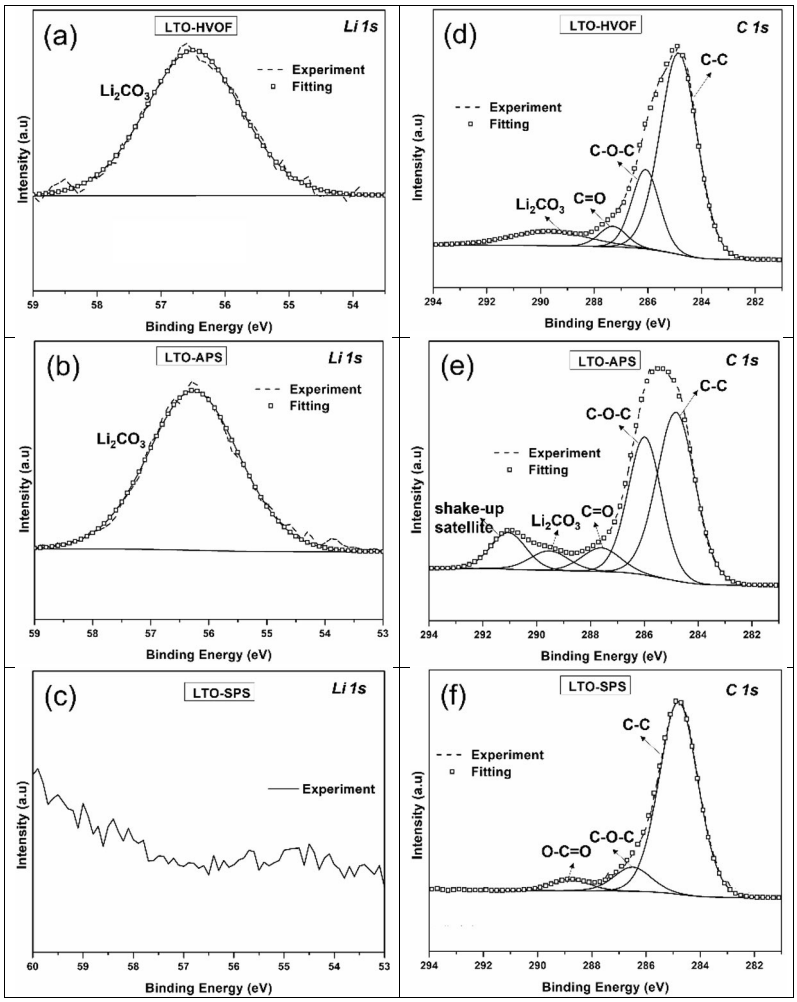

Figure 19. XPS spectra of Li 1s for (a) LTO-HVOF, (b) LTO-APS, and (c) LTO-SPS, with corresponding C 1s regions shown in (d–f) **[Publication II]**.

The C 1s spectra further support these trends. All thin-films show a C–C component at ~284.8 eV (adventitious carbon, used for charge referencing). For HVOF, additional peaks at ~286.1 eV (C–O), ~287.3 eV (C=O), and a strong carbonate feature at ~289.7 eV confirm surface Li_2CO_3 formation. LTO-APS displays a similar pattern with an additional peak at ~291.1 eV (shake-up of sp^2 carbon), suggesting partial graphitic carbon deposition. In LTO-SPS, C–C (284.8 eV), C–O (286.5 eV), and O–C=O (288.8 eV) peaks are present, but with no Li 1s or carbonate signals, consistent with lithium volatilization during spraying, likely as LiOH(g), due to reactions with water vapour in the suspension feedstock.

Overall, XPS reveals a process-dependent trend in surface lithium chemistry: HVOF and APS retain lithium at the surface, forming Li_2CO_3 passivation layers upon cooling, whereas SPS experiences near-complete surface lithium depletion. Bulk XRD and µXRD nonetheless confirm lithium-titanate phases within the SPS thin-films. Since XPS probes only a few nanometres, it is particularly sensitive to lithium–environment interactions at the final surface **[Publication II]**.

4.1.4.2 Laser Post-Processed Films

XPS analysis was also used to study the effect of pulsed LPP on the LLZO-LTO-APS surface. XPS analysis (Figure 20) shows that laser post-processing significantly alters the surface chemistry. The Li 1s peak remains, but carbonate species (CO_3^{2-}) increase. Zr and La signals, suppressed in the as-sprayed state, reappear, with Zr 3d (182.1/184.5 eV) and La 3d (834–839 eV) confirming Zr^{4+} and La^{3+} in the garnet lattice. Peak shapes and binding energies remain unchanged, indicating preserved oxidation states and no chemical degradation. Ti 2p peaks appear, consistent with Ti^{4+} from underlying LTO, corroborated by EDS maps showing partial LLZO layer removal and localized remelting. Overall, laser post-processing reduces surface carbonate coverage, reveals the intrinsic LLZO chemistry, exposes the LTO layer, and preserves all elemental chemical states. [**Publication V**]

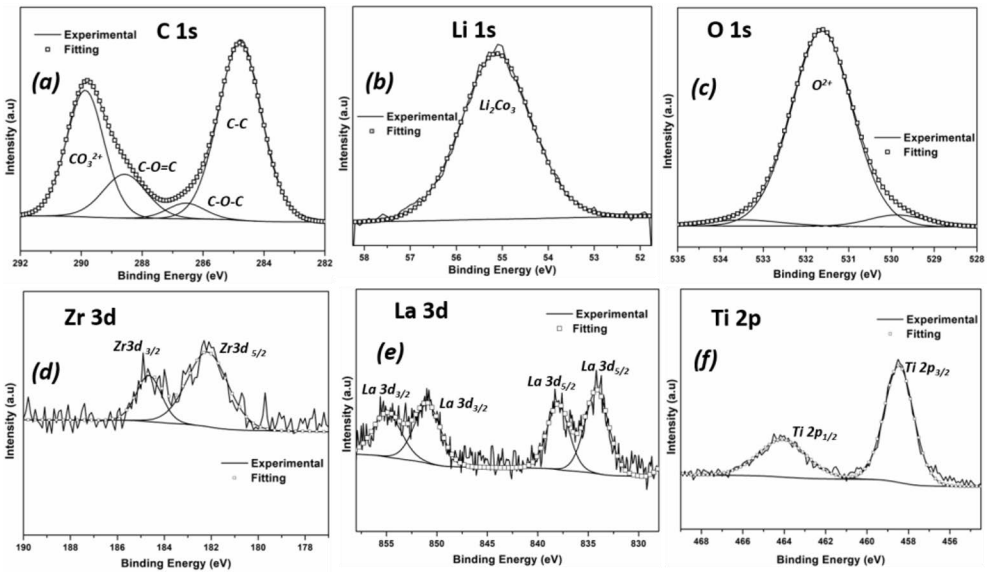

Figure 20. XPS spectra of laser post-processed APS double-layer LLZO-LTO showing the core level binding energy scans of C 1s, Li 1s, O 1s Zr 3d, La 3d in (a, b, c, d, e) respectively, (f) Ti 2p is also shown for the same highlighting the presence of Ti from the beneath LTO layer **[Publication V].**

4.2 Large-Scale Assessment of Thermally Sprayed TFASSBs

In addition to lab-scale techniques, large-scale synchrotron-based µXRD and µXRF were employed as large-scale facility methods to obtain spatially resolved insight into phase composition and elemental distribution at the micrometre scale. These tools are essential to resolve local heterogeneity and buried interfaces, which are not accessible to conventional techniques. This section first discusses µXRD-based phase analysis and then µXRF-based elemental mapping, again distinguishing between as-sprayed and laser post-processed films where applicable.

4.2.1 Phase assessment via Synchrotron µXRD

This section presents the results obtained from synchrotron-based micro-X-ray diffraction (µXRD) as a large-scale, high-resolution tool to evaluate phase composition in thermally sprayed TFASSB constituents. While Section 4.1.2 focused on bulk-averaged, lab-scale XRD, here the emphasis is on resolving local phase evolution within the thin-film interior (bulk), at thin-film–substrate interfaces,

and after laser post-processing (LPP). Detailed experimental settings and data-processing protocols are reported in the appended publications **[Publication I-III]**.

4.2.1.1 As-Thermally-Sprayed Films

4.2.1.1.1 Thin-film interior: phase fractions in LTO thin-films

Synchrotron µXRD mapping of the LTO thin-film interior revealed that the extent of decomposition from the parent spinel $Li_4Ti_5O_{12}$ (LTO) to secondary phases depends strongly on process enthalpy, exposure duration, and cooling rate. Quantitative Rietveld refinement of the µXRD data (Figure 21) showed the following phase fractions **[Publication II]**:

- LTO-HVOF: 66.8% LTO, 32.8% Li_2TiO_3, 0.4% TiO_2
- LTO-APS: 65.1% LTO, 34.0% Li_2TiO_3, TiO_2 below detection limit
- LTO-SPS: 53.5% LTO, 43.5% Li_2TiO_3, 3% TiO_2

In LTO-SPS, extreme plasma conditions combined with plasma–liquid interactions, such as droplet atomization and rapid solvent evaporation, intensify lithium volatilization and promote the formation of Li_2TiO_3 and TiO_2 **[Publication I]**. In contrast, LTO-HVOF involves lower particle temperatures, shorter residence times, and faster cooling, helping to preserve the spinel phase. LTO-APS, although characterized by high thermal input, lacks the liquid-phase chemistry of LTO-SPS and therefore achieves a degree of LTO retention similar to LTO-HVOF in the µXRD-mapped regions **[Publication II]**.

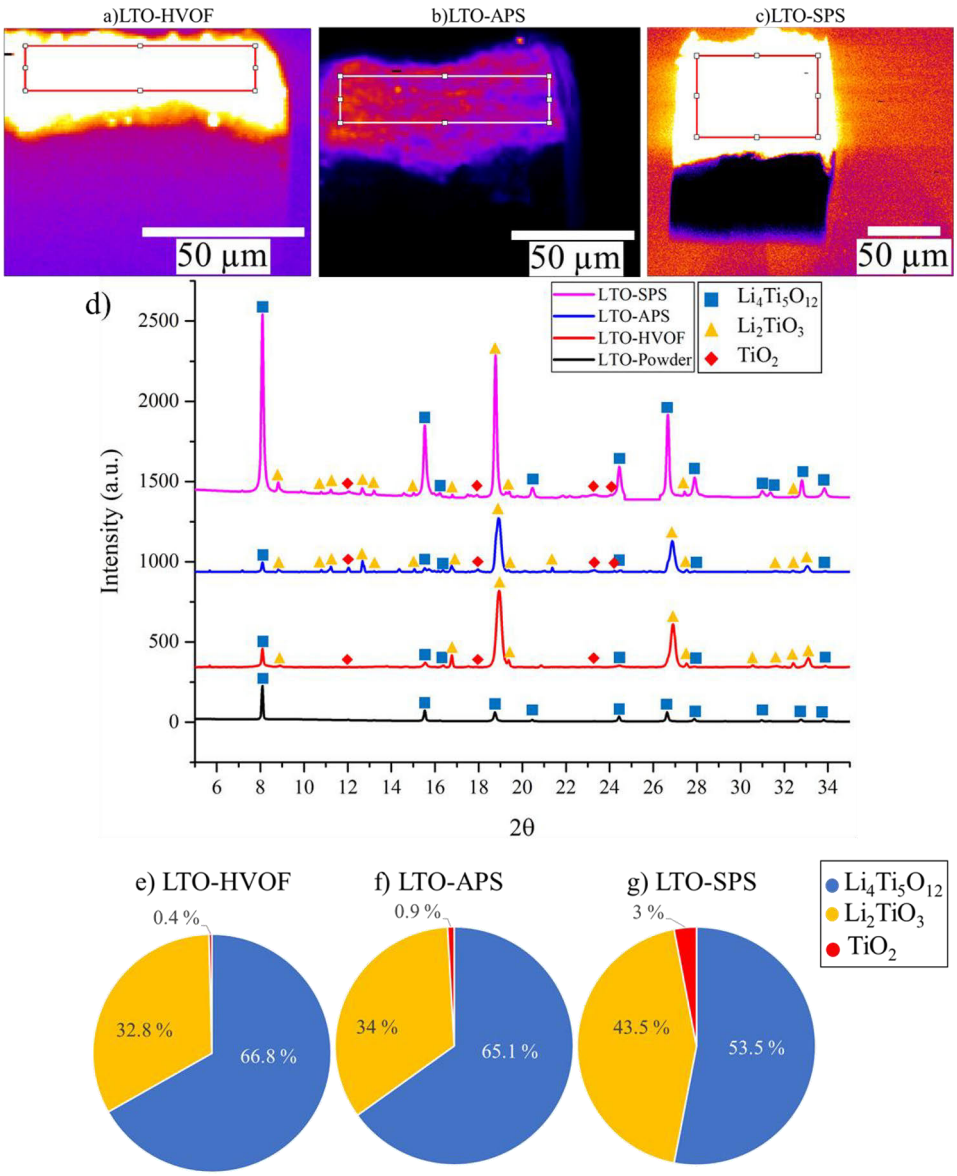

Figure 21. Synchrotron µXRD analysis of as-thermally-sprayed LTO thin-films mapped regions of interest (ROIs) for (a) LTO-APS, (b) LTO-SPS and (c) LTO-HVOF, (d) representative integrated patterns, (e–g) Rietveld-derived phase fraction **[Publication II].**

4.2.1.1.2 Thin-film–substrate interfaces: LTO/Al and LTO/SS-304

Depth-resolved µXRD analysis was then applied specifically at the thin-film–substrate interfaces for the three LTO thin-films (Figure 22). Aluminum substrates

were used for LTO-HVOF and LTO-APS, and stainless steel 304 (SS-304) for LTO-SPS. Unlike conventional lab XRD (probing ~5–10 µm in reflection mode), synchrotron µXRD in transmission geometry enabled localized phase identification directly at the interface **[Publication II]**:

- LTO-HVOF on Al: interface dominated by LTO peaks (62.3%), with 27.1% Li_2TiO_3 and 10.5% Al.
- LTO-APS on Al: higher Li_2TiO_3 (35.2%), stronger Al signal (15.3%), reduced LTO (49.5%).
- LTO-SPS on SS-304: interface dominated by substrate reflections (55.1% FCC and 6.7% BCC), with only 36.8% LTO and 6.7% Li_2TiO_3.

The LTO-HVOF interface is dominated by LTO, with moderate Li_2TiO_3 and a relatively weak substrate signal, indicating limited thermal degradation and interfacial reaction, consistent with low flame temperature and short residence time. LTO-APS shows higher Li_2TiO_3 and stronger Al contributions, reflecting partial LTO decomposition and enhanced diffusion at the interface under higher plasma enthalpy **[Publication II]**. At the LTO-SPS thin-film-substrate interface, the µXRD signal is dominated by SS-304 reflections, with lower LTO content and limited Li_2TiO_3, indicating poor LTO crystallinity and weak adhesion near the interface. The coexistence of FCC and BCC phases in SS-304 near the interface confirms partial BCC→FCC transformation driven by intense localized heating and rapid quenching **[Publication I].**

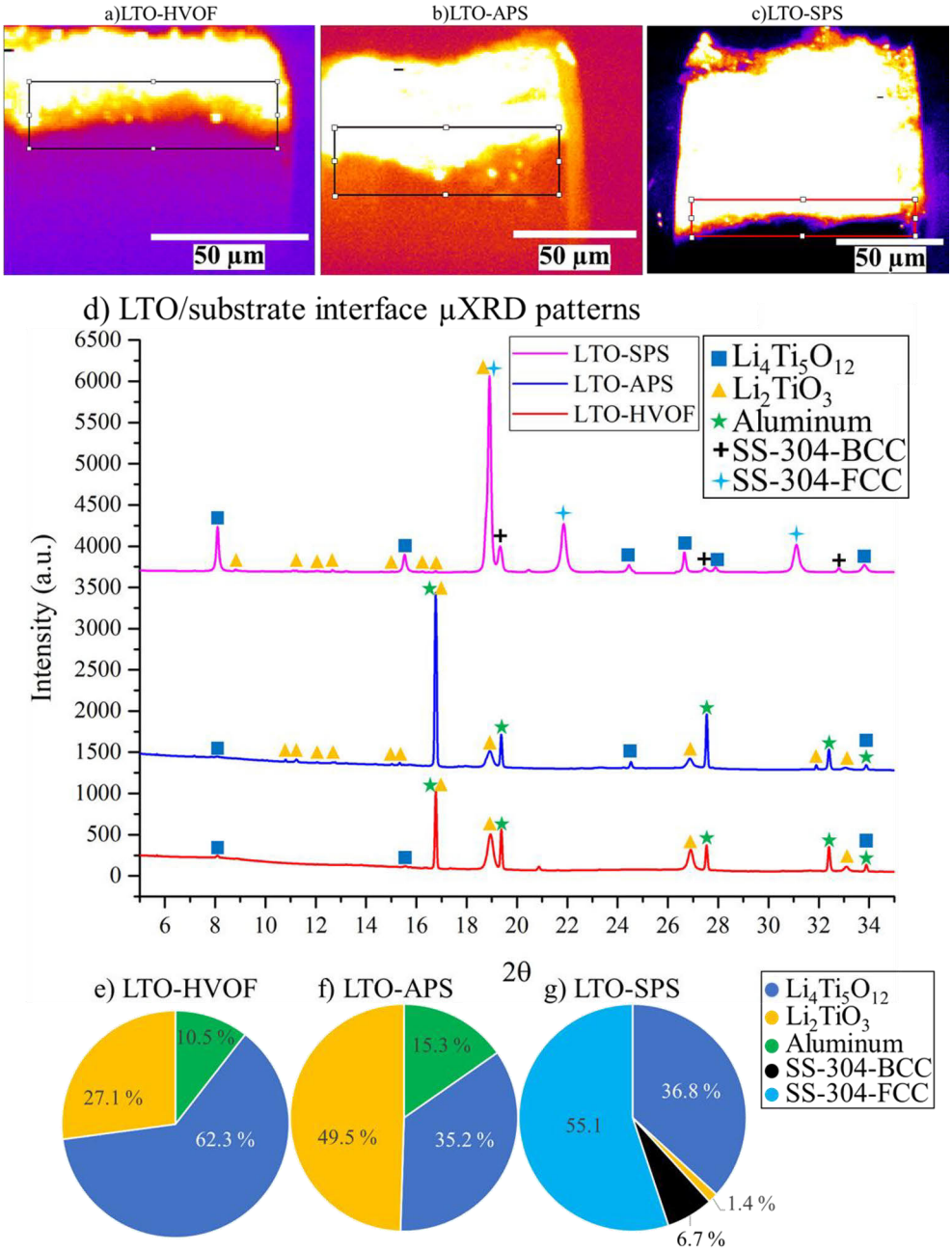

Figure 22. Synchrotron µXRD analysis of as-thermally-sprayed LTO thin-films mapped regions of interest (ROIs) for (a) LTO-APS, (b) LTO-SPS and (c) LTO-HVOF deposited films, (d) representative integrated patterns, (e–g) Rietveld-derived phase fraction **[Publication II].**

4.2.1.1.3 Local bright-spot analysis in LTO thin-films

One of the key advantages of synchrotron µXRD is the ability to probe small, pixel-sized ROIs and identify localized phase heterogeneities that cannot be captured by lab-scale XRD. For this purpose, several bright spots within the LTO-APS thin-film were examined (Figure 23). The µXRD patterns integrated over three bright regions (Spots 1–3) revealed multiple crystalline phases, deviating from the ideal single-phase spinel structure **[Publication II**]:

- All three spots contained Li_2TiO_3 and TiO_2, confirming partial LTO decomposition in specific micro-regions.
- Spot 1: retained the largest LTO fraction, with 25.4% LTO and 74.6% Li_2TiO_3.
- Spot 3: exhibited complete dominance of decomposition products, with 87.4% Li_2TiO_3 and 12.6% TiO_2

At Spots 1 and 2, traces of unreacted LTO were still present alongside Li_2TiO_3 and TiO_2, whereas Spot 3 represented a fully transformed region. These bright transformed zones are heterogeneously distributed across the thin-film and correspond to areas that likely experienced elevated in-flight temperatures or prolonged plasma exposure. Their presence explains the consistent detection of Li_2TiO_3 in both synchrotron and lab XRD analyses of LTO thin-films produced by HVOF, APS, and SPS. Nevertheless, despite the local dominance of Li_2TiO_3 within these zones, the overall thin-film remains spinel-rich when averaged over the full thickness **[Publication II]**.

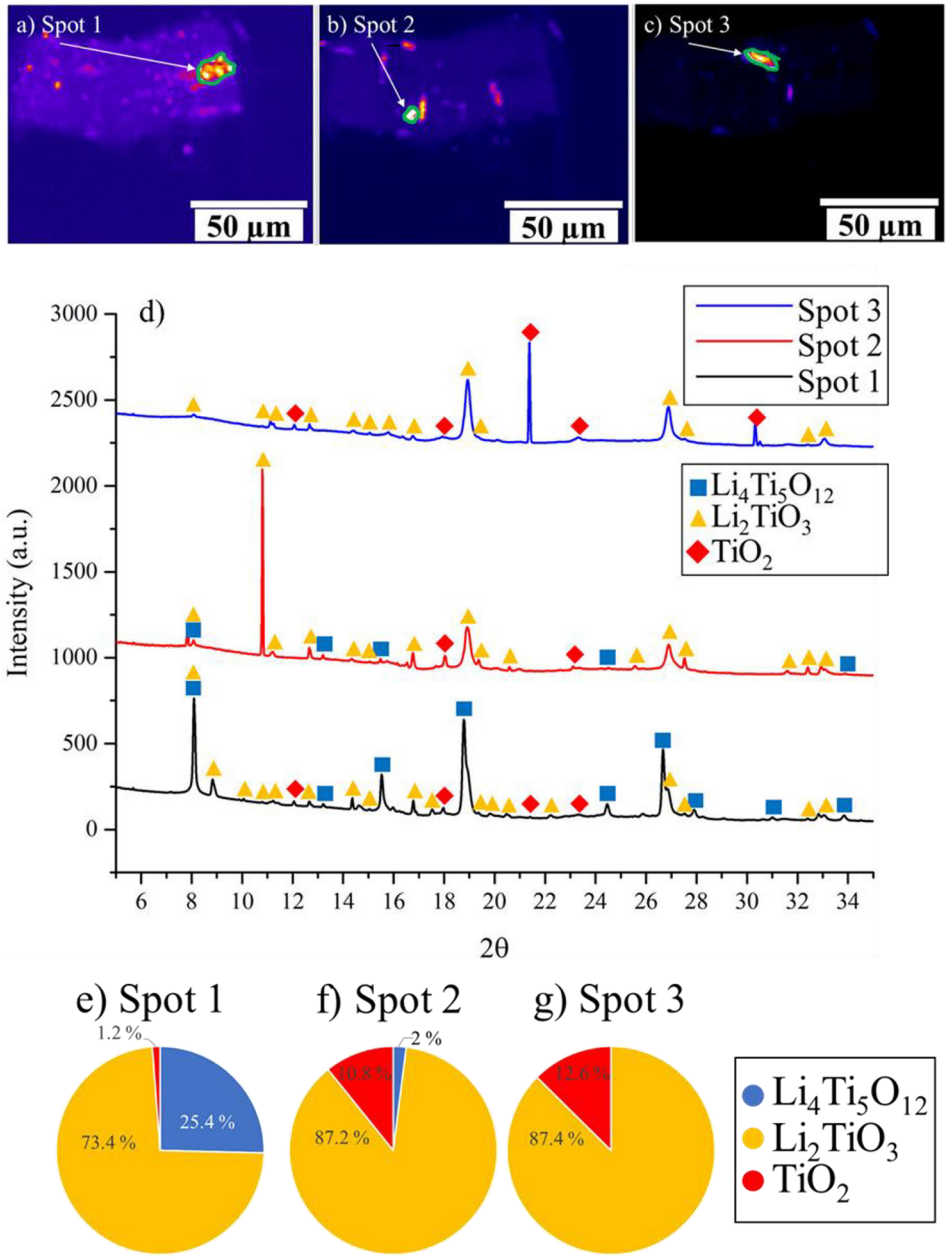

Figure 23. a-c) Synchrotron µXRD areas integrated over three distinct regions in the LTO-APS thin-film, where in spot 1 the diffraction is corresponded to 2θ=7.95, in the spot 2 the diffraction is corresponded to 2θ=10.73, and in the spot 3 the diffraction is corresponded to 2θ=21.73, d) Synchrotron µXRD patterns integrated over four distinct regions, e-g) phase percentages of spots 1-3 in the LTO-APS thin-film. **[Publication II].**

4.2.1.1.4 Through-thickness uniformity: top vs bottom regions

To further assess how processing conditions and substrate type influence phase uniformity, µXRD was conducted separately on top and bottom regions of the LTO-HVOF, LTO-APS, and LTO-SPS thin-films (Figure 24).

- For LTO-HVOF and LTO-APS, the diffraction patterns from top and bottom regions are nearly identical, indicating uniform phase composition through the thickness. This uniformity is attributed to relatively low thickness thin-films and the high thermal conductivity of the aluminum substrate, which enables efficient heat dissipation and similar cooling histories across the thin-film **[Publication II]**.
- For LTO-SPS, deposited on low-thermal-conductivity SS-304, noticeable differences appear between the top and bottom regions. A distinct color contrast near the substrate interface in the mapping images and the presence of two distinct peaks between top and bottom regions in the integrated patterns provide direct evidence of a through-thickness phase gradient. These variations are linked to higher thin-film thickness and slower heat transfer through steel, causing localized overheating and delayed solidification near the interface **[Publication I-II]**.

Minor intensity fluctuations in all patterns are mainly attributed to limited reflection statistics within the small probed volume rather than true compositional differences, except in the LTO-SPS case where clear peak differences confirm genuine phase gradients.

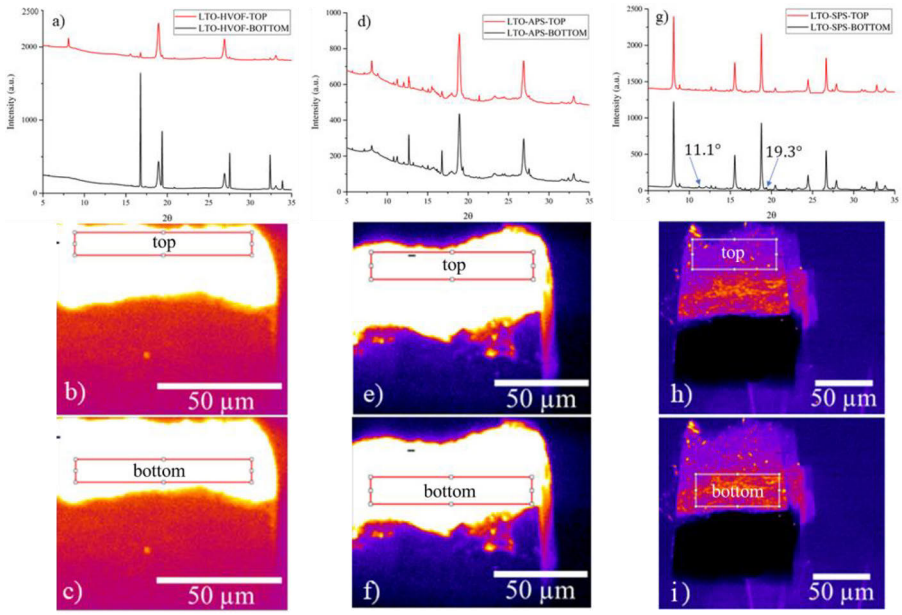

Figure 24. Synchrotron µXRD areas generated from selected areas from top and bottom sections integrated over LTO thin-films to show the phase distribution in the top and bottom part of LTO thin-films, a, b, c) LTO-HVOF, d, e, f) LTO-APS, g, h, i) LTO-SPS **[Publication II]**.

4.2.1.1.5 General interpretation for as-sprayed synchrotron µXRD results

Among the decomposition products, Li_2TiO_3 (monoclinic) consists of alternating Li and TiO_6 octahedral layers and is thermally stable up to ~1200 °C while being chemically inert in many environments [177]. However, its electrochemical performance is inferior to LTO, with practical capacities below 50 $mAh \cdot g^{-1}$ due to limited ionic and electronic conductivity. Consequently, Li_2TiO_3 is typically used as a passive or functional interlayer (e.g., buffer or SEI-like layer) in solid-state batteries rather than as an active anode material [138]. When formed within LTO thin-films, it decreases capacity and increases impedance.

Overall, the formation of Li_2TiO_3 and TiO_2 within LTO thin-films is a clear indicator of process-induced degradation. Consistent with µXRD phase quantification, LTO-SPS shows the most pronounced decomposition, while LTO-HVOF and LTO-APS maintain more than 65% LTO with only minor secondary phases. These trends align with earlier reports that link high plasma exposure to lithium loss and phase instability in LTO [83], [178], [179]. The synchrotron µXRD results therefore confirm that process enthalpy, plasma–liquid interactions, substrate thermal conductivity, and thin-film thickness collectively govern local phase stability and uniformity in thermally sprayed LTO anodes.

4.2.1.2 Laser Post-Processed Films

In addition to as-sprayed thin-films, synchrotron µXRD was employed to evaluate the effect of laser post-processing on phase composition in SPS-deposited LLZO solid-electrolyte thin-film single layers **[Publication III].**

4.2.1.2.1 Laser post-processed LLZO thin-films

According to Figure 25, µXRD analysis of the as-sprayed LLZO-SPS thin-film confirms that the primary garnet phase $Li_7La_3Zr_2O_{12}$ is largely retained, indicating partial preservation of the initial powder composition during plasma spraying. However, secondary phases were also detected, notably $La_2Zr_2O_7$ and $La(OH)_3$, formed due to thermal decomposition during plasma spraying and subsequent exposure to ambient moisture. However, LPP of LLZO-SPS induced further modifications in the phase composition. In the laser-processed regions, new phases such as Li_2ZrO_3 and Li_2CO_3 were identified **[Publication III]:**

- Li_2ZrO_3 formation is attributed to local high-temperature reactions involving Li and Zr species during surface remelting.
- Li_2CO_3 arises from chemical interaction with atmospheric CO_2 and H_2O at elevated temperatures, either through CO_2 absorption by LiOH or via direct reaction between LLZO and CO_2 [180].

Li_2CO_3 is known to be detrimental for garnet solid electrolytes, contributing to high interfacial resistance, voltage polarization, dendrite formation at Li anodes [181], and reduced ionic conductivity [182].

At the same time, the µXRD patterns show that $La(OH)_3$ peaks disappear after LPP, indicating its decomposition or evaporation under laser heating, consistent with its thermal instability [181], [182], [183]. Since $La(OH)_3$ is a well-documented impurity that increases interfacial resistance and degrades electrochemical performance in garnet-type electrolytes, its removal through LPP is beneficial for improving chemical purity and functional stability of LLZO-based solid electrolytes.

Taken together, the synchrotron µXRD results highlight the dual role of LPP for LLZO-SPS thin-films **[Publication III]**:

- Positively, LPP reduces surface roughness (as shown in Section 4.1.1) and eliminates detrimental $La(OH)_3$**,** thereby improving interfacial compatibility and chemical purity.
- Negatively, LPP also promotes the formation of Li_2CO_3 and Li_2ZrO_3**,** which can adversely affect interfacial resistance and ionic transport.

These findings underline the need for careful optimization of laser parameters and process atmosphere [184]. Future work should aim to preserve the beneficial effects of surface and phase refinement while suppressing unwanted decomposition products, supported by electrochemical testing to directly quantify performance changes.

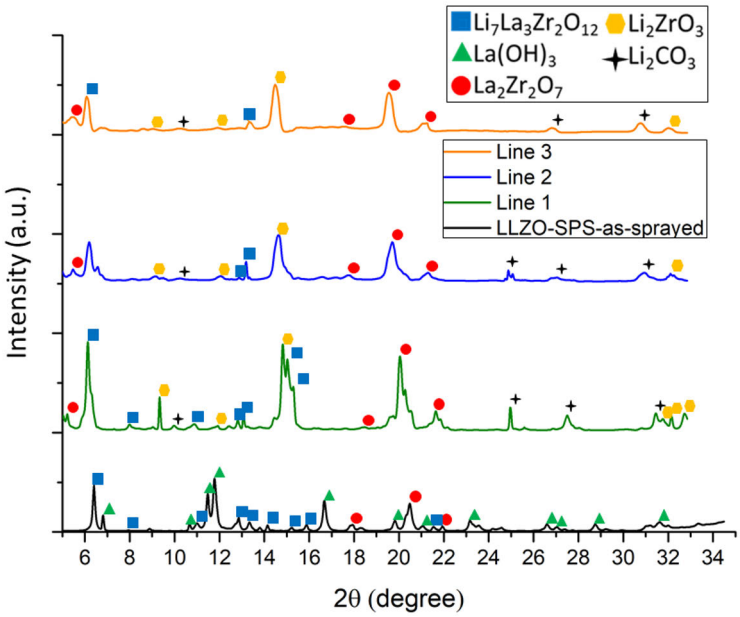

Figure 25. XRD patterns from laser-processed lines and the unprocessed region of as-sprayed LLZO-SPS, showing phase differences induced by laser processing **[Publication III]**

4.2.2 Elemental Assessment via Synchrotron µXRF

4.2.2.1 As-Thermally-Sprayed Films

Synchrotron-based micro-X-ray fluorescence (µXRF) mapping was employed as a complementary technique to µXRD to examine the spatial elemental distribution and interface integrity of thermally sprayed LTO thin-films **[Publication I-II]**. µXRF provides high-sensitivity, micron-scale elemental imaging, and when correlated with µXRD data, it enables detailed visualization of local chemical homogeneity across thin-film cross-sections.

For the LTO thin-films produced by HVOF, APS, and SPS in this study, Ti-Kα emission maps were acquired on LTO thin-film cross-sections (Figure 26). These Ti maps showed a continuous and uniform titanium distribution across all three thin-films, indicating homogeneous microstructures without obvious impurity-rich regions or undesired chemistry across the cross-section thickness. As mentioned in Chapter 3, the µXRF spectra were collected for elements with emission energies above ~2 keV, which is not sufficient to detect low atomic number elements such as lithium [185]. Therefore, the spatial distribution of lithium across the LTO thin-films can only be indirectly inferred from Ti and O intensity variations and from complementary XPS, XRD, and µXRD phase analysis data **[Publication I-II].**

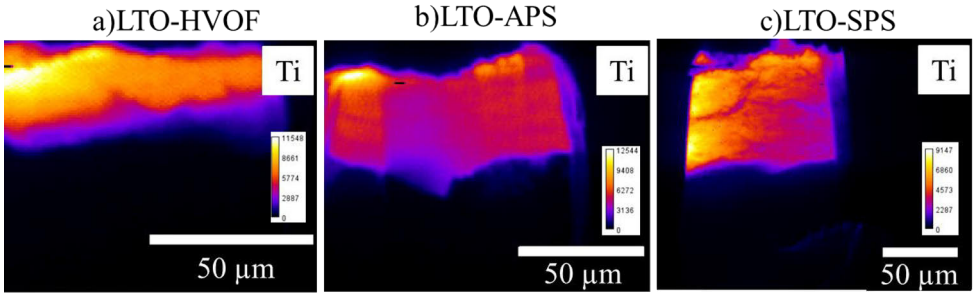

Figure 26. Synchrotron µXRF elemental maps of thermally sprayed LTO thin-films across thin-film cross-sections: (a) LTO-HVOF, (b) LTO-APS, and (c) LTO-SPS **[Publication II].**

To gain a more detailed understanding of interfacial chemistry in the system that exhibited the strongest indications of heterogeneity, µXRF elemental mapping was further focused on the LTO-SPS thin-film deposited on an SS-304 substrate. Among the three processes, SPS showed the most pronounced microstructural and phase non-uniformity in µXRD and lab-scale characterization, and the use of a stainless-steel substrate enabled simultaneous detection of multiple substrate elements (Fe, Cr, Ni, Mn) in addition to Ti from the LTO thin-film.

Figure 27 presents the elemental distributions obtained from the FIB-milled LTO-SPS thin-film sample. In Figure 27(a), the bright Ti signal defines a continuous LTO thin-film with a sharp thin-film–substrate interface, consistent with µXRD results confirming retention of the $Li_4Ti_5O_{12}$ spinel phase. Figures 27(b–e) show the distributions of Fe, Cr, Ni, and Mn originating from the SS-304 substrate. These maps reveal only limited interdiffusion of substrate elements into the LTO thin-film, confined to a narrow region extending a few micrometres from the interface **[Publication I]**. Although the interdiffusion of Fe, Cr, Ni, and Mn from the SS-304 substrate into the LTO thin-film is spatially limited and confined to a narrow near-interface region (on the order of a few micrometres), this localized diffusion is nonetheless significant. Even minor substrate element migration can locally perturb Li–Ti stoichiometry and Ti oxidation states, thereby promoting the formation of secondary phases such as $Li_2Ti_3O_7$, Li_2TiO_3, and TiO_2 detected by µXRD. Thus, the interdiffusion is limited in extent but consequential in terms of local phase evolution.

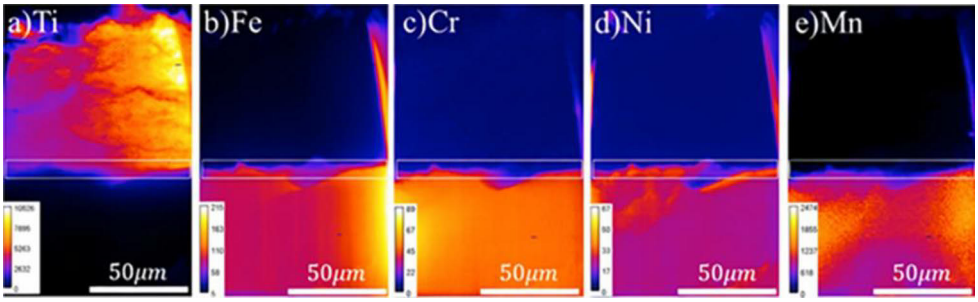

Figure 27. Elemental distribution in the LTO-SPS thin-film deposited on SS-304 **[Publication I]**

Taken together, the µXRF results complement the µXRD findings in two key ways. First, for all three LTO thin-films, continuous Ti-Kα maps confirm good thin-film continuity and strong adhesion at the macroscopic scale. Second, for the SPS thin-film on SS-304, the localized near-interface diffusion of Fe, Cr, Ni, and Mn is consistent with µXRD observations of secondary phases such as $Li_2Ti_3O_7$, Li_2TiO_3, and TiO_2, which likely form due to local stoichiometric changes and altered Ti oxidation states induced by substrate element migration **[Publication I]**. This combined µXRD–µXRF analysis thus provides a coherent picture of both phase distribution and elemental transport at the thin-film–substrate interface in thermally sprayed LTO thin-films.

4.2.2.2 Laser Post-Processed Films

In this thesis, synchrotron µXRF was applied only to as-sprayed thin-films. Elemental changes induced by LPP were therefore evaluated using lab-scale EDS (Section 4.1.3) and XPS (Section 4.1.4), while µXRD provided complementary phase information (Section 4.2.1.2). Extending µXRF mapping to laser-processed regions is a promising direction for future work to fully resolve LPP-induced elemental gradients at the micrometre scale.

4.3 Electrochemical Assessment of Thermally Sprayed LTO Thin-Film Anodes

Electrochemical testing was carried out only for the thermally sprayed LTO anodes. Cyclic voltammetry (CV) was performed at 0.1 $mV \cdot s^{-1}$ in the 1.0–2.5 V range to assess working voltage and polarization. LTO has a theoretical working voltage of 1.55 V vs. Li/Li^+ [186].

As shown in Figure 28(a), all LTO electrodes (LTO-HVOF, LTO-APS, LTO-SPS) exhibit a pair of reversible redox peaks at ~1.5 V (oxidation / cathodic potential, E_p,c). The reduction (anodic) potentials E_p,a are 1.68, 1.66, and 1.63 V for LTO-SPS, LTO-HVOF, and LTO-APS, respectively. The working voltage E_O , computed as:

$$E_O = \frac{E_{p,c} + E_{p,a}}{2} \qquad \text{Equation 3}$$

is 1.59, 1.58, and 1.56 V for LTO-SPS, LTO-HVOF, and LTO-APS, respectively. The LTO-APS electrode thus exhibits a working voltage closest to the theoretical 1.55 V vs. Li/Li^+.

The first galvanostatic charge–discharge (GCD) profiles at 0.05 C are shown in Figure 28(b). Unlike LTO-APS and LTO-HVOF electrodes, the LTO-SPS thin-film lacks a clear plateau near 1.55 V, reflecting extensive LTO decomposition observed earlier. The LTO-APS electrode delivers the highest first discharge capacity of 109 $mAh \cdot g^{-1}$ with an initial coulombic efficiency (ICE) of 69.5%, while LTO-SPS has the lowest ICE (60.7%).

Rate capability and cycling stability over 200 cycles at various C-rates (Figure 28(c)) confirm that LTO-APS offers superior electrochemical performance compared to LTO-HVOF and LTO-SPS. Although HVOF retains the highest fraction of LTO spinel according to µXRD and lab XRD, its electrochemical behaviour is hindered by ~6% Li_2CO_3, an insulating impurity that increases interfacial resistance [62]. The combination of LTO + Li_2TiO_3 without Li_2CO_3 contamination allows LTO-APS to attain the best performance among the three routes.

Thermally sprayed TFASSBs offer advantages in structural continuity and manufacturability, while alternative ASSB fabrication strategies emphasize peak electrochemical performance through interface optimization. In-situ solid electrolyte coatings and sulfide electrolyte infiltration into composite cathodes have achieved high capacities (up to ~196 mAh g^{-1}) with improved rate capability and cycling stability, whereas polymer-modified halide electrolytes enable stable cycling with >99% capacity retention at ~125 mAh g^{-1}. Advanced dry-binder electrodes further demonstrate capacities of ~184 mAh g^{-1} with good long-term retention. In contrast, vacuum-processed thin-film ASSBs exhibit exceptional cycling life and fast charging but remain limited by low areal capacity, positioning TFASSBs as a complementary, scalability-oriented approach [187], [188], [189], [190].

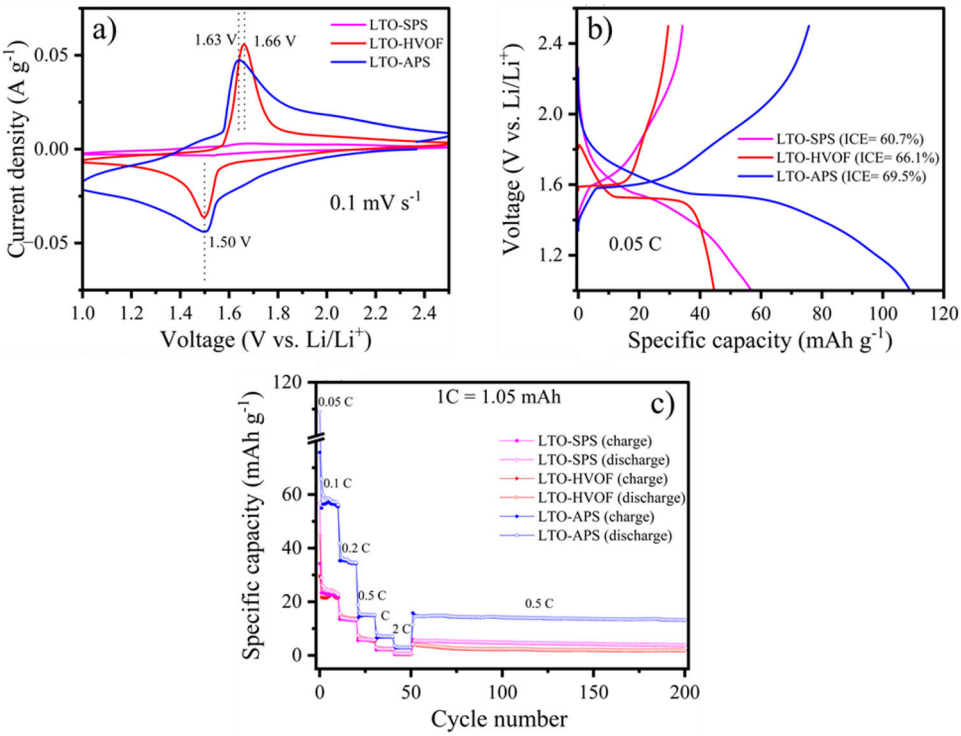

Figure 28. (a) CV curves, (b) initial charge–discharge profiles, and (c) rate and cycling performance of LTO-HVOF, LTO-APS, and LTO-SPS anode electrodes **[Publication II]**

5 Implications of Advanced Characterization for Thermally Sprayed TFASSBs

5.1 PSP² Matrix: Linking Process, Structure, Phase, and Performance

The combined findings from HVOF, APS, and SPS thin-films, together with LPP and multi-scale characterization, can be synthesized in a Process–Structure–Phase–Performance (PSP²) matrix (Table 13). This matrix provides a compact overview of how the different deposition routes and post-processing studied in this thesis influence:

1. Process conditions: thermal load, cooling rate, exposure time, atmosphere, plasma–liquid interactions in SPS, and LPP parameters.
2. Microstructural features: porosity, splat morphology, surface roughness, densification, and interfacial bonding in LTO and LLZO thin-films and in the LTO/LLZO half-cell.
3. Phase assemblages: spinel LTO versus Li_2TiO_3/TiO_2; garnet LLZO versus $La_2Zr_2O_7$, $La(OH)_3$, Li_2ZrO_3, Li_2CO_3; and surface Li_2CO_3 formation or Li-depleted surfaces identified by XRD/µXRD and XPS.
4. Electrochemical response: working voltage, capacity, rate capability, interfacial resistance, and cycling stability of the LTO electrodes.

In this thesis, the PSP² matrix should be interpreted primarily as a summary of experimentally observed correlations, rather than as a fully optimized process window. As highlighted earlier in Chapter 4, process optimization was not the main focus; instead, selected, reasonably performing thin-films were characterized in depth to establish baseline relationships between processing, local structure/phase formation, and electrochemical behaviour.

Table 16. PSP² matrix summarizing process–structure–phase–performance relationships for all thermally sprayed thin-film systems investigated in this thesis.

Process →	Structure →	Phase Composition →	Performance
HVOF	-Well-flattened splats, compact splats with minimal un-melted particles; uniform lamellar stacking. -Smooth, continuous interface with strong adhesion to Al substrate.	~67 % LTO (spinel), ~30 % Li_2TiO_3, minor TiO_2; occasional Li_2CO_3 from CO_2 uptake	High phase retention; good cycling stability
APS	-Coarse and irregular splats with partially melted particles and pronounced interlamellar ridges. -Rougher interface due to high plasma enthalpy; moderate adhesion.	~65 % LTO, ~34 % Li_2TiO_3; negligible TiO_2	Best electrochemical performance due to balanced spinel content and improved contact area
SPS	-Fine, thin, well-spread splats; dense microstructure but possible columnar features due to fine suspension feed. -Smooth interface on SS-304 substrate but diffusion layer formation reduces adhesion.	~53 % LTO, 44 % Li_2TiO_3, ~3 % TiO_2; higher Li loss	Lowest capacity; high chemical heterogeneity
Laser post-processing	-Re-melted, densified surface; crack-free under optimal energy; reduced roughness	-In the LTO anode, oxidation enrichment in, especially in lake-shaped melted zones. -In the LLZO electrolyte, Decomposition of $La(OH)_3$ and Li_2CO_3; enhanced crystallinity	Not measured but likely reduced interfacial resistance and improved phase stability

5.2 Multi-Scale Characterization Workflow for Thin-Film Battery Systems

Building on the characterization framework outlined, Figure 29 proposes a multi-scale characterization workflow for thermally sprayed thin-film battery systems. In this workflow, lab-scale tools (SEM/EDS, profilometry, XRD, XPS, electrochemistry) are used for initial screening of process conditions and overall performance, followed by synchrotron-based µXRD/µXRF for spatially resolved phase and elemental analysis. The insights gained from micro-characterization can then guide subsequent adjustments to thermal spray or LPP parameters, with electrochemical testing closing the loop.

This workflow reflects how the samples in this thesis were processed: not as fully optimized devices, but as model thin-films used to understand how thermal spraying and LPP affect phase evolution and interfacial chemistry at multiple length scales. The same logic can, in future work, be extended into an iterative process–characterization–refinement cycle for industrial process development.

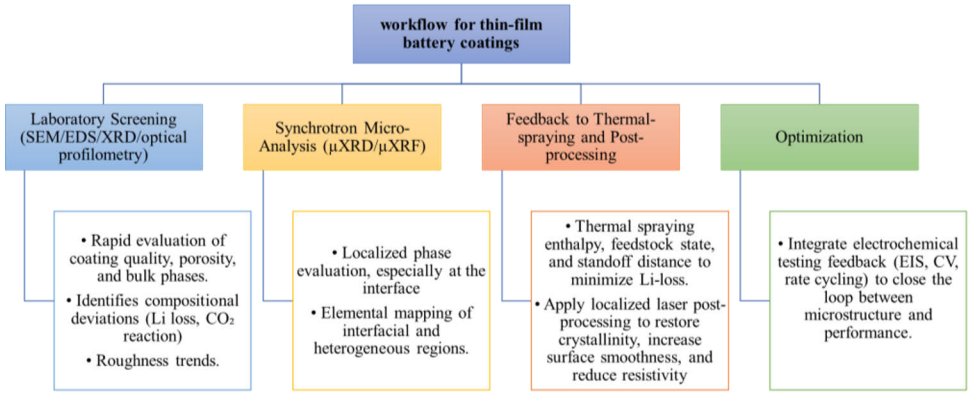

Figure 29. Workflow for thermally sprayed thin-film battery systems integrating lab-scale and synchrotron-based diagnostics with subsequent process refinement steps.

5.3 Complementarity of Lab-Scale and Synchrotron Tools

A key overarching outcome of this thesis is the complementarity between conventional lab-scale tools and synchrotron-based micro-probes, summarized in Table 15. Lab-scale SEM, EDS, XRD, and surface profilometry provide rapid, cost-effective screening of thin-film morphology, surface roughness, dominant phases, and averaged compositions over relatively large areas. These methods are indispensable for routine evaluation of thin-film quality and for comparing different thermal spray routes (HVOF, APS, SPS) and LPP conditions.

However, as demonstrated throughout Sections 4.1 and 4.2, bulk-averaged techniques alone cannot resolve micro-scale heterogeneities that arise from steep thermal gradients, plasma–liquid interactions, or substrate-driven diffusion. Synchrotron µXRD and µXRF bridge this gap by delivering micron-scale mapping of crystalline phases and elemental distributions through the film thickness and across buried interfaces. In this thesis, these methods revealed:

1. Localized Li_2TiO_3/TiO_2-rich regions predominantly within LTO thin-films.
2. Through-thickness phase gradients in SPS thin-films, contrasted with more homogeneous APS and HVOF cases.
3. Near-interface elemental migration (Fe, Cr, Ni, Mn) from SS-304 into LTO thin-films and its link to secondary-phase formation.
4. LPP-induced modifications to LLZO phase assemblages, including removal of $La(OH)_3$ and formation of Li_2ZrO_3 and Li_2CO_3.

These capabilities come with practical considerations such as beamtime access, FIB specimen preparation, and careful mitigation of potential beam- and FIB-induced artefacts. Nonetheless, when combined with lab-scale diagnostics,

synchrotron micro-characterization provides a multi-scale, quantitative picture of how thermal spray parameters and LPP shape local structure and chemistry, and how these, in turn, affect thermally sprayed TFASSB performance.

Table 17. Comparison of lab-scale tools and synchrotron-based µXRD/µXRF capabilities and limitations.

Category	Capabilities	Limitations
Bulk Laboratory Tools (SEM / EDS / XRD/ optical profilometry)	•Rapid, cost-effective screening of coating morphology, roughness, and major phase. •Provide averaged structural and compositional data over large areas. •Identify dominant crystalline phases, elemental distribution, and surface topography.	•Cannot resolve localized structural or chemical gradients at interfaces. •Limited depth sensitivity, surface-dominated information only. •Miss micro-scale heterogeneity that affects ionic transport and interfacial stability.
Synchrotron-Based (µXRD/µXRF)	•Provide micron-scale, spatially resolved mapping of crystal structure (µXRD) and elemental distribution (µXRF). • Detect minor secondary or metastable phases and compositional gradients invisible to bulk tools. •Correlate local structural distortions with chemical variations across interfaces. •Enable non-destructive probing of buried layers and interfacial reaction zones.	•Lower throughput and limited accessibility due to beamtime scheduling. •Requires sampling (FIB milling) •Requires careful mitigation of beam damage and data calibration for reproducibility.

5.4 Implications for Scalable Thermally Sprayed TFASSB Manufacturing

Finally, Figure 30 summarizes the main implications of this combined approach for scalable thermally sprayed TFASSB manufacturing. By using advanced characterization primarily as a diagnostic and understanding tool, rather than as a direct optimization engine, this thesis establishes a transferable methodology: thermal spray and LPP parameter sets can be evaluated not only in terms of macroscopic performance, but also in terms of how they control phase stability, interfacial reactions, and elemental gradients at the micrometre scale. This provides a robust foundation for future work aimed at true process optimization and cell-level implementation.

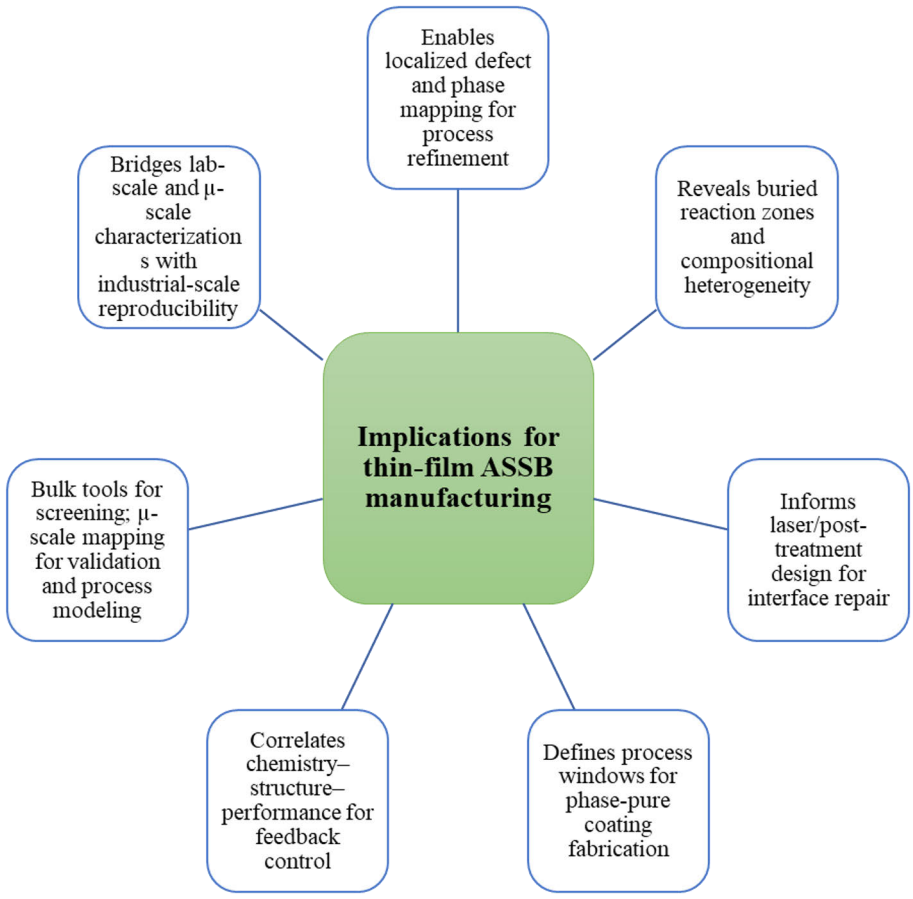

Figure 30. Key implications of combined lab-scale and synchrotron-based diagnostics for scalable thermally sprayed TFASSB manufacturing.

6 Summary/Conclusions

6.1 Conclusions

This dissertation sets out to develop a fundamental understanding of how thermal spraying (APS, SPS, HVOF) and laser post-processing (LPP) influence the microstructure, phase evolution, elemental gradients, and interfacial chemistry of thermally sprayed thin-film all-solid-state battery (TFASSB) constituents, and how advanced synchrotron micro-characterization can be used to establish robust process–structure–performance relationships. LTO anodes and LLZO solid electrolytes were used as model systems, and the work was guided by three sub-objectives and the associated research questions RQ1–RQ3 and hypotheses H1–H3.

With respect to **RQ1,** the results show that APS, SPS, and HVOF can all successfully produce LTO thin-films containing electrochemically active spinel $Li_4Ti_5O_{12}$, but with clear process-dependent differences in decomposition into Li_2TiO_3, $Li_2Ti_3O_7$, and TiO_2, as well as in interface quality. HVOF, with lower thermal enthalpy and higher particle velocities, preserved the LTO spinel phase most effectively and generated dense, uniform coatings with compact splats and good adhesion to Al substrates. APS LTO films exhibited more pronounced lamellar structures and higher surface roughness, yet retained a comparable LTO fraction in the film interior when parameters were carefully controlled. SPS LTO films showed the strongest signs of lithium volatilization and secondary phase formation, particularly near surfaces and interfaces, reflecting the combined effect of high plasma enthalpy and liquid feedstock chemistry. For LLZO, APS/SPS enabled the formation of garnet-type solid electrolyte layers, albeit with significant porosity, roughness, and strong sensitivity to process conditions. Together, these findings **only partially fulfilled Hypothesis H1:** thermal spraying is a viable high-throughput route for manufacturing TFASSB materials, but the degree of phase preservation and interface quality is critically governed by process enthalpy, feedstock state, and substrate heat management.

Addressing **RQ2,** LPP was shown to be an effective means to refine the inherently rough and heterogeneous microstructures generated by thermal spraying and to improve surface and interfacial properties of both single-layer and double-layer (LTO/LLZO) architectures. Optimised line-based and full-area LPP reduced

surface roughness of APS and SPS films by up to ~40%, while cross-sectional analyses revealed clear densification, thickness reduction, pore closure, and improved splat bonding in laser-remelted regions. In LTO/LLZO multilayers, LPP improved interfacial contact and reduced topographical mismatch between anode and electrolyte layers, which is essential for forming continuous solid–solid Li^+ transport pathways. However, excessive laser energy led to spattering, mud-crack formation, local film removal, and process-dependent compositional changes, such as enhanced LLZO oxidation and increased surface carbonate formation. These results, also **partially validated Hypothesis H2** that LPP is a powerful tool for microstructural refinement and interface engineering in thermally sprayed TFASSBs, while simultaneously highlighting a narrow processing window for Li-rich garnets that demands precise tuning of laser power, speed, frequency, and hatch spacing.

For **RQ3,** synchrotron µXRD and µXRF, complemented by XPS, proved indispensable for resolving local structural and chemical heterogeneities that conventional SEM/EDS/XRD cannot access. Synchrotron µXRD quantified process-dependent phase fractions both in the film interior and directly at the thin-film–substrate interfaces, revealing that lab-scale XRD systematically underestimates retained LTO spinel in HVOF and APS films and cannot resolve through-thickness gradients or interfacial reaction layers. Depth-resolved mappings identified micron-scale regions containing $Li_2Ti_3O_7$, Li_2TiO_3, and Ti-rich crystallites at splat boundaries and near thin-film–substrate interfaces. µXRF mapping exposed Ti-rich, La-rich, and Zr-rich inhomogeneities, diffusion layers, and lithium-related gradients (via cation and oxygen proxies) at LTO/metal and LLZO/metal interfaces, which correlate directly with local phase assemblages and expected interfacial resistance. Together with XPS evidence for Li_2CO_3 surface layers and lithium depletion, these results show that surface chemistry and carbonate formation are strongly process-specific: HVOF and APS can generate Li-rich surfaces prone to rapid carbonation in air, whereas SPS films exhibit severe surface Li loss despite retaining lithium-titanate phases in the bulk. Overall, these findings **fully validated Hypothesis H3**, demonstrating that synchrotron µXRD/µXRF provide the localized structural and chemical insight required to understand how non-equilibrium thermal spraying and LPP drive local phase evolution and interface formation.

Collectively, the thesis confirms that thermal spraying, when combined with carefully tuned laser post-processing and advanced synchrotron micro-characterization, provides a credible and industrially scalable manufacturing route for thermally sprayed ceramic TFASSB constituents. The proposed PSP^2 (Process–Structure–Phase–Performance) framework, which integrates lab-scale and synchrotron tools, establishes a generalizable methodology for linking thermal spray and laser parameters to microstructure, chemistry, and ultimately electrochemical

behaviour in non-equilibrium battery thin-films. Although the work deliberately focused on model LTO and LLZO layers and half-cell configurations rather than full multi-layer TFASSB stacks, the mechanistic insights into phase stability, lithium retention, surface chemistry, and solid–solid interface engineering are directly transferable to future multi-layer architectures and alternative chemistries. In this way, the dissertation provides both a scientific foundation and a methodological toolkit for moving thermally sprayed and laser-refined TFASSBs closer to technologically relevant, large-area solid-state battery systems.

6.2 Future Work

Based on the experience gained during this research, several future research directions can be proposed that address the remaining open questions and unexplored aspects in this field. These are outlined below:

- Exploring additional thermal spraying techniques, such as flame spraying and cold spraying, to evaluate their suitability for thin-film all-solid-state battery (TFASSB) fabrication.
- Manufacturing full-cell configurations using optimized parameters from the thermal spraying methods investigated in this work.
- Applying laser-directed energy deposition (L-DED) for the direct fabrication of TFASSB layers and assessing its potential advantages over conventional spraying methods.
- Utilizing femtosecond laser processing to study the influence of ultrafast laser parameters on the microstructure and performance of TFASSB components.
- Conducting synchrotron-based microanalysis on full-cell structures to better understand interfacial phenomena and phase evolution across multiple layers.
- Performing extended electrochemical evaluations of TFASSBs before and after laser post-processing to determine the long-term impact of laser processing on cell performance.

Acknowledgements

I would like to express my sincere gratitude to the *University of Turku* for offering me the opportunity to join this research project and the PhD program, and for hosting me in Finland throughout my doctoral journey. I am deeply thankful to *Finland* as a country for providing me the opportunity to build a new chapter of life, to experience a new culture, and to grow both professionally and personally. I am especially grateful to the *Finnish people* and my colleagues for their acceptance, hospitality, patience, kindness, and support, which made Finland truly feel like a second home.

I gratefully acknowledge the financial support received during my doctoral studies from the *GREEN-BAT project* (2022–2025, grant no. 352517) under the M-ERA.NET framework, co-funded by the Research Council of Finland, the European Commission (M-ERA.NET 3), and national and regional funding agencies in Finland, Sweden, and Germany. Additional funding was provided by the *SOLACE* Academy Research Fellowship (DNR 360540), funded by the Research Council of Finland. I also acknowledge personal financial support from the *TOP-Säätiö* foundation and the *DPT grant from University of Turku*, which covered seven months of my salary during my Ph.D. studies. This project has also received funding from the *European Union's Horizon 2020* research and innovation programme under grant agreement No. 958174. I further acknowledge the *Finnish Digital Design and Manufacturing Infrastructure (FiDiEm)* for providing access to experimental facilities.

My deepest gratitude goes to my primary supervisor, *Professor Ashish Ganvir*, for his exceptional guidance, constant support, and genuine kindness. His down-to-earth attitude allowed me to seek his advice freely at any stage of my PhD. His strong encouragement to attend conferences and engage in international research environments enabled me to expand my scientific network, collaborate with outstanding researchers, and mature as an independent scientist. Most importantly, his empathy and understanding created a peaceful and low-stress research environment that made this challenging journey both enjoyable and fulfilling.

I also sincerely thank my co-supervisor, *Professor Antti Salminen*, for his continuous support, wisdom, and encouragement. His vast experience both scientific and life-related has been invaluable. I am equally grateful to my co-supervisor, *Dr. Sneha Goel*, for her guidance, support, and consistently kind and professional attitude.

I would like to warmly thank *Dr. Małgorzata Grażyna Makowska* for her support and hospitality during my research visits to PSI, as well as for her professional advice

and regular scientific discussions. I also acknowledge *Dr. Joakim Reuteler* for his valuable assistance with FIB milling of samples.

My sincere thanks go to *Professor Jussi Kantola*, Head of our department, for his support, responsibility, and thoughtful leadership, and to *Professor Shrikant Joshi* for his encouragement, insightful advice, and inspiring comments.

I am deeply thankful to *Dr. Aki Piiroinen*, our outstanding laboratory engineer at QTT, University of Turku, for his technical expertise, unwavering assistance in experimental work, and for his friendship. I also thank *Stefan Björklund* from University West, Trollhättan, for his invaluable support in plasma spraying of battery materials, and *Dr. Ermei Mäkila* for his assistance with SEM/EDS and XPS measurements.

I would like to acknowledge my colleagues and friends who supported me throughout this PhD journey, both scientifically and emotionally: *Dr. Vahid Abbasi, Professor Mohsen Amraei, Dr. Saeid Parchegani, Dr. Mojtaba Miri, and Dr. Behnam Chameh.* Their friendship and mental support were as important as their scientific contributions. I also thank *Dr. Vinay Gidla, Dr. Nikhil Kamboj, and Dr. Chinmayee Nayak* for their collaboration and contributions to our joint publications. My sincere appreciation goes to all members of the DMS research group for creating a positive, motivating, and friendly working atmosphere.

To my friends and family members in Iran and around the world *Mahdi, Hosain, Ehsan, Narges, Amin, Babak, Meysam, Shiva, Mostafa, Ali, Reza, and Human* thank you for your constant emotional support. Without your encouragement, this journey would not have been possible.

Above all, my deepest and most heartfelt gratitude goes to my family. To my *parents and my sister*, I cannot express in words how essential your love, patience, sacrifices, and unconditional support have been throughout this journey. Every step I took forward was built on your strength and belief in me. I truly cannot imagine completing this PhD without you standing beside me, even across distances.

I also acknowledge all those who, in one way or another, supported me during this PhD journey.

Finally, I dedicate this work to my *home country, Iran*. I carry Iran with me wherever I go. I hope for a future of freedom, prosperity, and growth, meaning development, flourishing, and lasting progress for my country and its people.

February. 2026
Arman Hasani

ARMAN HASANI

MY RESEARCH INTERESTS ENCOMPASS ADVANCED MATERIALS PROCESSING AND MANUFACTURING, WITH PARTICULAR EMPHASIS ON LASER-BASED TECHNOLOGIES, THERMAL SPRAY PROCESSES, AND SOLID-STATE LITHIUM-ION BATTERY MATERIALS. I POSSESS EXTENSIVE EXPERTISE IN LASER MATERIALS PROCESSING, INCLUDING ADDITIVE MANUFACTURING, SURFACE MODIFICATION, AND POST-PROCESSING. MY RESEARCH IS STRONGLY SUPPORTED BY COMPREHENSIVE EXPERIENCE IN MATERIALS CHARACTERIZATION, RANGING FROM MICROSTRUCTURAL AND PHASE ANALYSIS TO ADVANCED SYNCHROTRON-BASED TECHNIQUES. IN PARALLEL WITH MY RESEARCH ACTIVITIES, I HAVE ACCUMULATED SUBSTANTIAL TEACHING EXPERIENCE IN MECHANICAL AND MATERIALS SCIENCE AND ENGINEERING, COVERING SUBJECTS SUCH AS MATERIALS CHARACTERIZATION, CERAMICS PROCESSING, AND MANUFACTURING TECHNOLOGIES. THIS COMBINATION OF RESEARCH, TEACHING, AND HANDS-ON TECHNICAL EXPERIENCE HAS SHAPED A SYSTEMATIC AND APPLICATION-ORIENTED APPROACH TO MECHANICAL AND MATERIALS ENGINEERING, WHICH UNDERPINS THE WORK PRESENTED IN THIS THESIS.

List of References

[1] J. Tahalyani, M. J. Akhtar, J. Cherusseri, and K. K. Kar, “Characteristics of Capacitor: Fundamental Aspects,” 2020, pp. 1–51. doi: 10.1007/978-3-030-43009-2_1.

[2] B. Dunn, H. Kamath, and J.-M. Tarascon, “Electrical Energy Storage for the Grid: A Battery of Choices,” *Science (1979).*, vol. 334, no. 6058, pp. 928–935, Nov. 2011, doi: 10.1126/science.1212741.

[3] B. Nykvist and M. Nilsson, “Rapidly falling costs of battery packs for electric vehicles,” *Nat. Clim. Chang.*, vol. 5, no. 4, pp. 329–332, Apr. 2015, doi: 10.1038/nclimate2564.

[4] S. Sakib, Md. B. Hossain, M. A. Zamee, M. J. Hossain, and Md. A. Habib, “Role of battery energy storage systems: A comprehensive review on renewable energy zones integration in weak transmission networks,” *J. Energy Storage*, vol. 128, p. 117223, Aug. 2025, doi: 10.1016/j.est.2025.117223.

[5] Y. Liang *et al.*, “A review of rechargeable batteries for portable electronic devices,” *InfoMat*, vol. 1, no. 1, pp. 6–32, Mar. 2019, doi: 10.1002/inf2.12000.

[6] J. B. Goodenough and K.-S. Park, “The Li-Ion Rechargeable Battery: A Perspective,” *J. Am. Chem. Soc.*, vol. 135, no. 4, pp. 1167–1176, Jan. 2013, doi: 10.1021/ja3091438.

[7] M. Sajjad, Y. Zhang, A. J. Khan, D. Zhang, L. Gao, and G. Zhao, “Solid-state lithium batteries: Opportunities and limitations for next-generation energy storage,” *J. Alloys Compd.*, vol. 1034, p. 181405, Jun. 2025, doi: 10.1016/j.jallcom.2025.181405.

[8] P. Roy and S. K. Srivastava, “Nanostructured anode materials for lithium ion batteries,” *J. Mater. Chem. A Mater.*, vol. 3, no. 6, pp. 2454–2484, 2015, doi: 10.1039/C4TA04980B.

[9] F. Zheng, M. Kotobuki, S. Song, M. O. Lai, and L. Lu, “Review on solid electrolytes for all-solid-state lithium-ion batteries,” *J. Power Sources*, vol. 389, pp. 198–213, Jun. 2018, doi: 10.1016/j.jpowsour.2018.04.022.

[10] T. Famprikis, P. Canepa, J. A. Dawson, M. S. Islam, and C. Masquelier, “Fundamentals of inorganic solid-state electrolytes for batteries,” *Nat. Mater.*, vol. 18, no. 12, pp. 1278–1291, Dec. 2019, doi: 10.1038/s41563-019-0431-3.

[11] X. Yao *et al.*, “All-solid-state lithium batteries with inorganic solid electrolytes: Review of fundamental science,” *Chinese Physics B*, vol. 25, no. 1, p. 018802, Jan. 2016, doi: 10.1088/1674-1056/25/1/018802.

[12] M. Kotobuki *et al.*, “Preparation of thin solid electrolyte by hot-pressing and diamond wire slicing,” *RSC Adv.*, vol. 9, no. 21, pp. 11670–11675, 2019, doi: 10.1039/C9RA00711C.

[13] M. Rosner *et al.*, “Toward Higher Energy Density All-Solid-State Batteries by Production of Freestanding Thin Solid Sulfidic Electrolyte Membranes in a Roll-to-Roll Process,” *Adv. Energy Mater.*, vol. 15, no. 19, May 2025, doi: 10.1002/aenm.202404790.

[14] C. Wang *et al.*, “Solvent-Free Approach for Interweaving Freestanding and Ultrathin Inorganic Solid Electrolyte Membranes,” *ACS Energy Lett.*, vol. 7, no. 1, pp. 410–416, Jan. 2022, doi: 10.1021/acsenergylett.1c02261.

[15] S. Li *et al.*, “Sulfide-based composite solid electrolyte films for all-solid-state batteries,” *Commun. Mater.*, vol. 5, no. 1, p. 44, Mar. 2024, doi: 10.1038/s43246-024-00482-8.

[16] J. F. M. Oudenhoven, Loïc. Baggetto, and P. H. L. Notten, “All-Solid-State Lithium-Ion Microbatteries: A Review of Various Three-Dimensional Concepts,” *Adv. Energy Mater.*, vol. 1, no. 1, pp. 10–33, Jan. 2011, doi: 10.1002/aenm.201000002.

[17] A. Jetybayeva, B. Uzakbaiuly, A. Mukanova, S.-T. Myung, and Z. Bakenov, “Recent advancements in solid electrolytes integrated into all-solid-state 2D and 3D lithium-ion microbatteries,” *J. Mater. Chem. A Mater.*, vol. 9, no. 27, pp. 15140–15178, 2021, doi: 10.1039/D1TA02652F.

[18] B. Ke and X. Wang, “Integratable all-solid-state thin-film microbatteries,” *Proceedings of the National Academy of Sciences*, vol. 122, no. 16, Apr. 2025, doi: 10.1073/pnas.2415693122.

[19] N. J. Dudney, “Thin Film Micro-Batteries,” *Electrochem. Soc. Interface*, vol. 17, no. 3, pp. 44–48, Sep. 2008, doi: 10.1149/2.F04083IF.

[20] T. Khan, S. Bihn, D. U. Sauer, and N. Fuengwarodsakul, “Cathode Thickness Variation Analysis and Pareto Optimization of Virtual Li-Ion Cells,” in *2022 International Conference on Power, Energy and Innovations (ICPEI)*, IEEE, Oct. 2022, pp. 1–4. doi: 10.1109/ICPEI55293.2022.9986762.

[21] K. Lee, K. Yanagi, T. Arashi, and M. Kodama, “3D simulation of all-solid-state batteries with real electrode structures derived from X-ray computed tomography,” *J. Power Sources*, vol. 654, p. 237821, Oct. 2025, doi: 10.1016/j.jpowsour.2025.237821.

[22] T. Wu, W. Dai, M. Ke, Q. Huang, and L. Lu, “All-Solid-State Thin Film μ-Batteries for Microelectronics,” *Advanced Science*, vol. 8, no. 19, Oct. 2021, doi: 10.1002/advs.202100774.

[23] R. Pfenninger, S. Afyon, I. Garbayo, M. Struzik, and J. L. M. Rupp, “Lithium Titanate Anode Thin Films for Li-Ion Solid State Battery Based on Garnets,” *Adv. Funct. Mater.*, vol. 28, no. 21, May 2018, doi: 10.1002/adfm.201800879.

[24] S. Puls *et al.*, “Benchmarking the reproducibility of all-solid-state battery cell performance,” *Nat. Energy*, vol. 9, no. 10, pp. 1310–1320, Sep. 2024, doi: 10.1038/s41560-024-01634-3.

[25] A. M. Laptev, H. Zheng, M. Bram, M. Finsterbusch, and O. Guillon, “High-pressure field assisted sintering of half-cell for all-solid-state battery,” *Mater. Lett.*, vol. 247, pp. 155–158, Jul. 2019, doi: 10.1016/j.matlet.2019.03.109.

[26] L. Wang *et al.*, “Fundamentals of Electrolytes for Solid-State Batteries: Challenges and Perspectives,” *Front. Mater.*, vol. 7, Jul. 2020, doi: 10.3389/fmats.2020.00111.

[27] T.-L. Pham, L. Wang, and B. Ouyang, “Design principles for anode stable solid-state electrolytes,” *J. Mater. Chem. A Mater.*, vol. 12, no. 31, pp. 19979–19987, 2024, doi: 10.1039/D4TA02269F.

[28] P. Arunachalam, G. Murugadoss, C. Karuppiah, A. M. Al-Mayouf, and C.-C. Yang, “Prospective Anodes for Solid-State Lithium-Ion Battery,” 2022, pp. 65–81. doi: 10.1007/978-3-031-12470-9_3.

[29] P. Sivaraj, K. P. Abhilash, P. Nithyadharseni, S. Agarwal, S. A. Joshi, and Z. Sofer, “Interfaces in Solid-State Batteries: Challenges and Design Strategies,” 2022, pp. 193–218. doi: 10.1007/978-3-031-12470-9_7.

[30] A. Machín, C. Morant, and F. Márquez, “Advancements and Challenges in Solid-State Battery Technology: An In-Depth Review of Solid Electrolytes and Anode Innovations,” *Batteries*, vol. 10, no. 1, p. 29, Jan. 2024, doi: 10.3390/batteries10010029.

[31] K. H. Kim *et al.*, “Characterization of the interface between LiCoO2 and Li7La3Zr2O12 in an all-solid-state rechargeable lithium battery,” *J. Power Sources*, vol. 196, no. 2, pp. 764–767, Jan. 2011, doi: 10.1016/j.jpowsour.2010.07.073.

[32] A. M. Nolan, Y. Liu, and Y. Mo, “Solid-State Chemistries Stable with High-Energy Cathodes for Lithium-Ion Batteries,” *ACS Energy Lett.*, vol. 4, no. 10, pp. 2444–2451, Oct. 2019, doi: 10.1021/acsenergylett.9b01703.

[33] S. Choi *et al.*, “Quantitative Analysis of Microstructures and Reaction Interfaces on Composite Cathodes in All-Solid-State Batteries Using a Three-Dimensional Reconstruction Technique,” *ACS Appl. Mater. Interfaces*, vol. 10, no. 28, pp. 23740–23747, Jul. 2018, doi: 10.1021/acsami.8b04204.

[34] W. Xu *et al.*, “Lithium metal anodes for rechargeable batteries,” *Energy Environ. Sci.*, vol. 7, no. 2, pp. 513–537, 2014, doi: 10.1039/C3EE40795K.

[35] I. Madinabeitia *et al.*, “Monolithic All-Solid-State High-Voltage Li-Metal Thin-Film Rechargeable Battery,” *ACS Appl. Energy Mater.*, vol. 5, no. 10, pp. 12120–12131, Oct. 2022, doi: 10.1021/acsaem.2c01581.

[36] K. B. Hatzell *et al.*, “Challenges in Lithium Metal Anodes for Solid-State Batteries,” *ACS Energy Lett.*, vol. 5, no. 3, pp. 922–934, Mar. 2020, doi: 10.1021/acsenergylett.9b02668.

[37] A. Jetybayeva, D. S. Aaron, I. Belharouak, and M. M. Mench, “Critical review on recently developed lithium and non-lithium anode-based solid-state lithium-ion batteries,” *J. Power Sources*, vol. 566, p. 232914, May 2023, doi: 10.1016/j.jpowsour.2023.232914.

[38] Y. Huang, B. Shao, Y. Wang, and F. Han, “Solid-state silicon anode with extremely high initial coulombic efficiency,” *Energy Environ. Sci.*, vol. 16, no. 4, pp. 1569–1580, 2023, doi: 10.1039/D2EE04057C.

[39] H. Pan *et al.*, “A solid-state lithium-ion battery with micron-sized silicon anode operating free from external pressure,” *Nat. Commun.*, vol. 15, no. 1, p. 2263, Mar. 2024, doi: 10.1038/s41467-024-46472-9.

[40] X. Zhan *et al.*, “Challenges and opportunities towards silicon-based all-solid-state batteries,” *Energy Storage Mater.*, vol. 61, p. 102875, Aug. 2023, doi: 10.1016/j.ensm.2023.102875.

[41] H. Huo and J. Janek, "Silicon as Emerging Anode in Solid-State Batteries," *ACS Energy Lett.*, vol. 7, no. 11, pp. 4005–4016, Nov. 2022, doi: 10.1021/acsenergylett.2c01950.

[42] T. Palaniselvam, A. I. Freytag, H. Moon, K. A. Janßen, S. Passerini, and P. Adelhelm, "Tin–Graphite Composite as a High-Capacity Anode for All-Solid-State Li-Ion Batteries," *The Journal of Physical Chemistry C*, vol. 126, no. 31, pp. 13043–13052, Aug. 2022, doi: 10.1021/acs.jpcc.2c04024.

[43] Y. Zheng *et al.*, "Recent advances in solid-state lithium batteries based on anode engineering," *Nano Research Energy*, vol. 3, no. 3, p. e9120118, Sep. 2024, doi: 10.26599/NRE.2024.9120118.

[44] P. U. Nzereogu, A. D. Omah, F. I. Ezema, E. I. Iwuoha, and A. C. Nwanya, "Anode materials for lithium-ion batteries: A review," *Applied Surface Science Advances*, vol. 9, p. 100233, Jun. 2022, doi: 10.1016/j.apsadv.2022.100233.

[45] Y. Huang, B. Shao, and F. Han, "Li alloy anodes for high-rate and high-areal-capacity solid-state batteries," *J. Mater. Chem. A Mater.*, vol. 10, no. 23, pp. 12350–12358, 2022, doi: 10.1039/D2TA02339C.

[46] J. A. Lewis, K. A. Cavallaro, Y. Liu, and M. T. McDowell, "The promise of alloy anodes for solid-state batteries," *Joule*, vol. 6, no. 7, pp. 1418–1430, Jul. 2022, doi: 10.1016/j.joule.2022.05.016.

[47] C. Yu *et al.*, "Core-shell engineering of titanium-based anodes toward enhanced electrochemical lithium/sodium storage performance: a review," *Mater. Today Energy*, vol. 43, p. 101589, Jul. 2024, doi: 10.1016/j.mtener.2024.101589.

[48] Z. Chen, I. Belharouak, Y. -K. Sun, and K. Amine, "Titanium-Based Anode Materials for Safe Lithium-Ion Batteries," *Adv. Funct. Mater.*, vol. 23, no. 8, pp. 959–969, Feb. 2013, doi: 10.1002/adfm.201200698.

[49] R. Okuno, M. Yamamoto, A. Kato, and M. Takahashi, "Performance improvement of nanoporous Si composite anodes in all-solid-state lithium-ion batteries by using acetylene black as a conductive additive," *Electrochem. commun.*, vol. 138, p. 107288, May 2022, doi: 10.1016/j.elecom.2022.107288.

[50] T. Panneerselvam, R. Murugan, and O. V. Sreejith, "Highly stable all-solid-state batteries with Li–LTO composite anode," *Sustain. Energy Fuels*, vol. 8, no. 8, pp. 1704–1711, 2024, doi: 10.1039/D3SE01730C.

[51] H. Ueda, F. Mizuno, M. Forsyth, and P. C. Howlett, "Tailoring Silicon Composite Anodes with Li^+-Containing Organic Ionic Plastic Crystals for Solid-State Batteries," *J. Electrochem. Soc.*, vol. 171, no. 2, p. 020556, Feb. 2024, doi: 10.1149/1945-7111/ad29c5.

[52] G. Kalita, T. Endo, and T. Nishi, "Recent development on low temperature synthesis of cubic-phase LLZO electrolyte particles for application in all-solid-state batteries," *J. Alloys Compd.*, vol. 969, p. 172282, Dec. 2023, doi: 10.1016/j.jallcom.2023.172282.

[53] C. Xu, Y. Xue, M. Zhang, and N. Liao, "Atomic-level designed LLZO electrolyte for LTO electrode in all-solid-state batteries with superb interfacial properties," *Surfaces and Interfaces*, vol. 40, p. 103128, Aug. 2023, doi: 10.1016/j.surfin.2023.103128.

[54] Y. Li, Y. Zhai, S. Xu, M. Tang, S. Zhang, and Z. Zou, “Using LLTO with vertically aligned and oriented structures to improve the ion conductivity of composite solid-state electrolytes,” *Mater. Today Commun.*, vol. 33, p. 104243, Dec. 2022, doi: 10.1016/j.mtcomm.2022.104243.

[55] S. Stramare, V. Thangadurai, and W. Weppner, “Lithium Lanthanum Titanates: A Review,” *Chemistry of Materials*, vol. 15, no. 21, pp. 3974–3990, Oct. 2003, doi: 10.1021/cm0300516.

[56] J. Sastre, A. Priebe, M. Döbeli, J. Michler, A. N. Tiwari, and Y. E. Romanyuk, “Lithium Garnet $Li_7La_3Zr_2O_{12}$ Electrolyte for All-Solid-State Batteries: Closing the Gap between Bulk and Thin Film Li-Ion Conductivities,” *Adv. Mater. Interfaces*, vol. 7, no. 17, Sep. 2020, doi: 10.1002/admi.202000425.

[57] S. HORI, “Development of Li₁₀GeP₂S₁₂-type Solid Electrolytes for the Understanding of Superionic Conduction, and Their Application in All-solid-state Batteries,” *Electrochemistry*, vol. 92, no. 10, pp. 24–00075, Oct. 2024, doi: 10.5796/electrochemistry.24-00075.

[58] K. Hikima, R. Kishi, H. Tsukasaki, S. Mori, H. Muto, and A. Matsuda, “Electrochemical Properties of $Li_{10}GeP_2S_{12}$ Solid Electrolytes Synthesized Using a Solution-Based Method,” *ACS Appl. Energy Mater.*, vol. 7, no. 19, pp. 8788–8796, Oct. 2024, doi: 10.1021/acsaem.4c01759.

[59] W.-Q. Ding, F. Lv, N. Xu, M.-T. Wu, J. Liu, and X.-P. Gao, “Polyethylene Oxide-Based Solid-State Composite Polymer Electrolytes for Rechargeable Lithium Batteries,” *ACS Appl. Energy Mater.*, vol. 4, no. 5, pp. 4581–4601, May 2021, doi: 10.1021/acsaem.1c00216.

[60] X. Su, X.-P. Xu, Z.-Q. Ji, J. Wu, F. Ma, and L.-Z. Fan, “Polyethylene Oxide-Based Composite Solid Electrolytes for Lithium Batteries: Current Progress, Low-Temperature and High-Voltage Limitations, and Prospects,” *Electrochemical Energy Reviews*, vol. 7, no. 1, p. 2, Dec. 2024, doi: 10.1007/s41918-023-00204-7.

[61] S. Wang and G. P. Demopoulos, “High-conductive polymer-in-porous garnet solid electrolyte structure for all-solid-state lithium batteries enabled by molecular engineering,” *Energy Storage Mater.*, vol. 71, p. 103604, Aug. 2024, doi: 10.1016/j.ensm.2024.103604.

[62] X. Liu *et al.*, “Designing Compatible Ceramic/Polymer Composite Solid-State Electrolyte for Stable Silicon Nanosheet Anodes,” *Small*, vol. 20, no. 25, Jun. 2024, doi: 10.1002/smll.202309724.

[63] B. Put, P. M. Vereecken, J. Meersschaut, A. Sepúlveda, and A. Stesmans, “Electrical Characterization of Ultrathin RF-Sputtered LiPON Layers for Nanoscale Batteries,” *ACS Appl. Mater. Interfaces*, vol. 8, no. 11, pp. 7060–7069, Mar. 2016, doi: 10.1021/acsami.5b12500.

[64] H. Su *et al.*, “Recent progress of sulfide electrolytes for all-solid-state lithium batteries,” *Energy Materials*, 2022, doi: 10.20517/energymater.2022.01.

[65] J.-Y. Han *et al.*, “Electrospun 1D Al-LLZO incorporated PVDF-HFP composite electrolyte with fast Li+ pathway derived from highway-traction effect for high performance lithium metal batteries,” *Chemical Engineering Journal*, vol. 505, p. 159627, Feb. 2025, doi: 10.1016/j.cej.2025.159627.

[66] N. J. Dudney and B. J. Neudecker, “Solid state thin-film lithium battery systems,” *Curr. Opin. Solid State Mater. Sci.*, vol. 4, no. 5, pp. 479–482, Oct. 1999, doi: 10.1016/S1359-0286(99)00052-2.

[67] J. Ko and Y. S. Yoon, “Influence of process conditions on structural and electrochemical properties of lithium phosphorus oxynitride thin films,” *Ceram. Int.*, vol. 46, no. 13, pp. 20623–20632, Sep. 2020, doi: 10.1016/j.ceramint.2020.05.251.

[68] Y. Yu, M. Gong, C. Dong, and X. Xu, “Thin-film deposition techniques in surface and interface engineering of solid-state lithium batteries,” *Next Nanotechnology*, vol. 3–4, p. 100028, Sep. 2023, doi: 10.1016/j.nxnano.2023.100028.

[69] Z. Jiang *et al.*, “Enabling superior electrochemical performance of NCA cathode in Li5.5PS4.5Cl1.5-based solid-state batteries with a dual-electrolyte layer,” *Chinese Chemical Letters*, vol. 35, no. 4, p. 108561, Apr. 2024, doi: 10.1016/j.cclet.2023.108561.

[70] Y. Lyu *et al.*, “An Overview on the Advances of $LiCoO_2$ Cathodes for Lithium-Ion Batteries,” *Adv. Energy Mater.*, vol. 11, no. 2, Jan. 2021, doi: 10.1002/aenm.202000982.

[71] T. Fan *et al.*, “Operating Highly Stable $LiCoO_2$ Cathodes up to 4.6 V by Using an Effective Integration of Surface Engineering and Electrolyte Solutions Selection,” *Adv. Funct. Mater.*, vol. 32, no. 33, Aug. 2022, doi: 10.1002/adfm.202204972.

[72] Z. Duan, Y. Wu, J. Lin, L. Wang, and D.-L. Peng, “Thin-Film Lithium Cobalt Oxide for Lithium-Ion Batteries,” *Energies (Basel).*, vol. 15, no. 23, p. 8980, Nov. 2022, doi: 10.3390/en15238980.

[73] R. Hao and W. Sun, “Facile synthesis of LiFePO4/Cu composite as enhanced cathode material for lithium-ion battery by a solid-state grinding method,” *Int. J. Electrochem. Sci.*, vol. 19, no. 8, p. 100684, Aug. 2024, doi: 10.1016/j.ijoes.2024.100684.

[74] H. Erabhoina and M. Thelakkat, “Tuning of composition and morphology of LiFePO4 cathode for applications in all solid-state lithium metal batteries,” *Sci. Rep.*, vol. 12, no. 1, p. 5454, Mar. 2022, doi: 10.1038/s41598-022-09244-3.

[75] C.-Y. Lin, J.-G. Duh, C.-H. Hsu, and J.-M. Chen, “LiNi0.5Mn1.5O4 cathode material by low-temperature solid-state method with excellent cycleability in lithium ion battery,” *Mater. Lett.*, vol. 64, no. 21, pp. 2328–2330, Nov. 2010, doi: 10.1016/j.matlet.2010.07.017.

[76] H. J. Lee *et al.*, “$LiNi_{0.5}Mn_{1.5}O_4$ Cathode Microstructure for All-Solid-State Batteries,” *Nano Lett.*, vol. 22, no. 18, pp. 7477–7483, Sep. 2022, doi: 10.1021/acs.nanolett.2c02426.

[77] Z.-J. Zhang *et al.*, “Enhancing the High Rate Capability and Cycling Stability of $LiMn_2O_4$ by Coating of Solid-State Electrolyte $LiNbO_3$,” *ACS Appl. Mater. Interfaces*, vol. 6, no. 24, pp. 22155–22165, Dec. 2014, doi: 10.1021/am5056504.

[78] T. Takeuchi *et al.*, “Improvement of the rate capability of all-solid-state cells with Fe-based polysulfide positive electrode materials by modifying the microstructure,” *RSC Adv.*, vol. 14, no. 10, pp. 7229–7233, 2024, doi: 10.1039/D3RA08641K.

[79] T. Gavrilova *et al.*, “Li3V2(PO4)3 Cathode Material: Synthesis Method, High Lithium Diffusion Coefficient and Magnetic Inhomogeneity,” *Int. J. Mol. Sci.*, vol. 25, no. 5, p. 2884, Mar. 2024, doi: 10.3390/ijms25052884.

[80] N. R. Khasanova, O. A. Drozhzhin, D. A. Storozhilova, C. Delmas, and E. V. Antipov, “New Form of Li $_2$ FePO $_4$ F as Cathode Material for Li-Ion Batteries,” *Chemistry of Materials*, vol. 24, no. 22, pp. 4271–4273, Nov. 2012, doi: 10.1021/cm302724a.

[81] S. Lv, M. Li, X. Luo, J. Cheng, and Z. Li, “High-voltage LiNi0.5Mn1.5O4 thin film cathodes stabilized by LiPON solid electrolyte coating to enhance cyclic stability and rate capability,” *J. Alloys Compd.*, vol. 815, p. 151636, Jan. 2020, doi: 10.1016/j.jallcom.2019.07.348.

[82] D. Ren *et al.*, “Challenges and opportunities of practical sulfide-based all-solid-state batteries,” *eTransportation*, vol. 18, p. 100272, Oct. 2023, doi: 10.1016/j.etran.2023.100272.

[83] D. L. Wood *et al.*, “Perspectives on the relationship between materials chemistry and roll-to-roll electrode manufacturing for high-energy lithium-ion batteries,” *Energy Storage Mater.*, vol. 29, pp. 254–265, Aug. 2020, doi: 10.1016/j.ensm.2020.04.036.

[84] J. Schnell, F. Tietz, C. Singer, A. Hofer, N. Billot, and G. Reinhart, “Prospects of production technologies and manufacturing costs of oxide-based all-solid-state lithium batteries,” *Energy Environ. Sci.*, vol. 12, no. 6, pp. 1818–1833, 2019, doi: 10.1039/C8EE02692K.

[85] K. B. Hatzell and Y. Zheng, “Prospects on large-scale manufacturing of solid state batteries,” *MRS Energy & Sustainability*, vol. 8, no. 1, pp. 33–39, Mar. 2021, doi: 10.1557/s43581-021-00004-w.

[86] M. Batzer, C. Heck, P. Michalowski, and A. Kwade, “Current Status of Formulations and Scalable Processes for Producing Sulfidic Solid-State Batteries,” *Batter. Supercaps*, vol. 5, no. 12, Dec. 2022, doi: 10.1002/batt.202200328.

[87] J. Lee, T. Lee, K. Char, K. J. Kim, and J. W. Choi, “Issues and Advances in Scaling up Sulfide-Based All-Solid-State Batteries,” *Acc. Chem. Res.*, vol. 54, no. 17, pp. 3390–3402, Sep. 2021, doi: 10.1021/acs.accounts.1c00333.

[88] J. Minkiewicz *et al.*, “Large-scale manufacturing of solid-state electrolytes: Challenges, progress, and prospects,” *Open Ceramics*, vol. 16, p. 100497, Dec. 2023, doi: 10.1016/j.oceram.2023.100497.

[89] T. H. Dolla, S. O. Ajayi, L. L. Sikeyi, M. K. Mathe, and N. Palaniyandy, “Advances in solid-state batteries fabrication strategies for their manufacture,” *J. Energy Storage*, vol. 106, p. 114737, Jan. 2025, doi: 10.1016/j.est.2024.114737.

[90] B. Wu, C. Chen, D. L. Danilov, R.-A. Eichel, and P. H. L. Notten, “All-Solid-State Thin Film Li-Ion Batteries: New Challenges, New Materials, and New Designs,” *Batteries*, vol. 9, no. 3, p. 186, Mar. 2023, doi: 10.3390/batteries9030186.

[91] N. Gavrilov, A. Kamenetskikh, P. Tretnikov, and A. Ershov, “Synthesis of LiPON Solid Electrolyte Films by Thermal Evaporation of Lithium Orthophosphate,” *Coatings*, vol. 13, no. 10, p. 1765, Oct. 2023, doi: 10.3390/coatings13101765.

[92] M. Z. Ansari *et al.*, “Atomic Layer Deposition—A Versatile Toolbox for Designing/Engineering Electrodes for Advanced Supercapacitors,” *Advanced Science*, vol. 11, no. 1, Jan. 2024, doi: 10.1002/advs.202303055.

[93] H. Xia, L. Lu, and G. Ceder, “Li diffusion in LiCoO2 thin films prepared by pulsed laser deposition,” *J. Power Sources*, vol. 159, no. 2, pp. 1422–1427, Sep. 2006, doi: 10.1016/j.jpowsour.2005.12.012.

[94] N. H. Menzler, J. Malzbender, P. Schoderböck, R. Kauert, and H. P. Buchkremer, “Sequential Tape Casting of Anode-Supported Solid Oxide Fuel Cells,” *Fuel Cells*, vol. 14, no. 1, pp. 96–106, Feb. 2014, doi: 10.1002/fuce.201300153.

[95] L. O. Orzari *et al.*, “Screen-Printing vs Additive Manufacturing Approaches: Recent Aspects and Trends Involving the Fabrication of Electrochemical Sensors,” *Anal. Chem.*, vol. 97, no. 3, pp. 1482–1494, Jan. 2025, doi: 10.1021/acs.analchem.4c05786.

[96] J. Chen, Y. Yuan, Q. Wang, H. Wang, and R. C. Advincula, “Bridging Additive Manufacturing and Electronics Printing in the Age of AI,” *Nanomaterials*, vol. 15, no. 11, p. 843, May 2025, doi: 10.3390/nano15110843.

[97] S. Matsuda, “New Insights into Fundamental Processes and Physical Degradation Mechanisms in Rechargeable Lithium-Oxygen Batteries Providing Suitably High Energy Densities,” *ChemElectroChem*, vol. 11, no. 6, Mar. 2024, doi: 10.1002/celc.202300605.

[98] Y. Yang *et al.*, “Kinetic Mechanism and Structural Design of Thick Electrodes in Lithium-Ion Batteries: Challenges and Optimization Strategies,” *Small*, vol. 21, no. 43, Oct. 2025, doi: 10.1002/smll.202506931.

[99] J. Wu, L. Yuan, W. Zhang, Z. Li, X. Xie, and Y. Huang, “Reducing the thickness of solid-state electrolyte membranes for high-energy lithium batteries,” *Energy Environ. Sci.*, vol. 14, no. 1, pp. 12–36, 2021, doi: 10.1039/D0EE02241A.

[100] Y. Kim *et al.*, “Thermally Driven Interfacial Degradation between $Li_7La_3Zr_2O_{12}$ Electrolyte and $LiNi_{0.6}Mn_{0.2}Co_{0.2}O_2$ Cathode,” *Chemistry of Materials*, vol. 32, no. 22, pp. 9531–9541, Nov. 2020, doi: 10.1021/acs.chemmater.0c02261.

[101] M. Balaish *et al.*, “Emerging processing guidelines for solid electrolytes in the era of oxide-based solid-state batteries,” *Chem. Soc. Rev.*, vol. 54, no. 19, pp. 8925–9007, 2025, doi: 10.1039/D5CS00358J.

[102] Q. Wang *et al.*, “Optimization and progress of interface construction of ceramic oxide solid-state electrolytes in Li-metal batteries,” *Energy Storage Mater.*, vol. 71, p. 103589, Aug. 2024, doi: 10.1016/j.ensm.2024.103589.

[103] J. Liang *et al.*, “Current Status and Future Directions in Environmental Stability of Sulfide Solid-State Electrolytes for All-Solid-State Batteries,” *Energy Material Advances*, vol. 4, Jan. 2023, doi: 10.34133/energymatadv.0021.

[104] G. Patry, A. Romagny, S. Martinet, and D. Froelich, “Cost modeling of lithium-ion battery cells for automotive applications,” *Energy Sci. Eng.*, vol. 3, no. 1, pp. 71–82, Jan. 2015, doi: 10.1002/ese3.47.

[105] K. Ukoba and T.-C. Jen, “Challenges and Opportunities of Thin Films and 3D Printing,” 2025, pp. 235–325. doi: 10.1007/978-3-031-84124-8_4.

[106] K. Tufail Chaudhary, “Thin Film Deposition: Solution Based Approach,” in *Thin Films*, IntechOpen, 2021. doi: 10.5772/intechopen.94455.

[107] M. El Hammoumi, V. Chaudhary, P. Neugebauer, and A. El Fatimy, “Chemical vapor deposition: a potential tool for wafer scale growth of two-dimensional layered materials,” *J. Phys. D Appl. Phys.*, vol. 55, no. 47, p. 473001, Nov. 2022, doi: 10.1088/1361-6463/ac928d.

[108] N. H. Faisal *et al.*, “Thermal Spray Coatings for Electromagnetic Wave Absorption and Interference Shielding: A Review and Future Challenges,” *Adv. Eng. Mater.*, vol. 24, no. 7, p. 2200171, Jul. 2022, doi: 10.1002/adem.202200171.

[109] N. Yamaguchi, T. Hattori, K. Terashima, and T. Yoshida, “High-rate deposition of LiNbO3 films by thermal plasma spray CVD,” *Thin Solid Films*, vol. 316, no. 1–2, pp. 185–188, Mar. 1998, doi: 10.1016/S0040-6090(98)00412-X.

[110] M. Topuz, O. Yigit, M. Kaseem, and B. Dikici, “Synthesis of implantable ceramic coatings and their properties,” in *Advanced Ceramic Coatings for Biomedical Applications*, Elsevier, 2023, pp. 53–86. doi: 10.1016/B978-0-323-99626-6.00008-1.

[111] S. Sampath, “Thermal Spray Applications in Electronics and Sensors: Past, Present, and Future,” *Journal of Thermal Spray Technology*, vol. 19, no. 5, pp. 921–949, Sep. 2010, doi: 10.1007/s11666-010-9475-2.

[112] Y. Liu *et al.*, “Roll-to-roll solvent-free manufactured electrodes for fast-charging batteries,” *Joule*, vol. 7, no. 5, pp. 952–970, May 2023, doi: 10.1016/j.joule.2023.04.006.

[113] D. Tejero-Martin, M. Rezvani Rad, A. McDonald, and T. Hussain, “Beyond Traditional Coatings: A Review on Thermal-Sprayed Functional and Smart Coatings,” *Journal of Thermal Spray Technology*, vol. 28, no. 4, pp. 598–644, Apr. 2019, doi: 10.1007/s11666-019-00857-1.

[114] V. Gopal *et al.*, “Exploring atmospheric plasma spraying as a pathway to fabricate solid-state battery constituents,” *Surf. Coat. Technol.*, vol. 502, p. 131945, Apr. 2025, doi: 10.1016/j.surfcoat.2025.131945.

[115] S. Mathiyalagan *et al.*, “Facile one-step fabrication of Li4Ti5O12 coatings by suspension plasma spraying,” *Mater. Res. Bull.*, vol. 181, p. 113111, Jan. 2025, doi: 10.1016/j.materresbull.2024.113111.

[116] J. Schou, B. Toftmann, and S. Amoruso, “Pulsed laser deposition: from basic processes to film deposition (Invited Paper),” P. A. Atanasov, S. V. Gateva, L. A. Avramov, and A. A. Serafetinides, Eds., Apr. 2005, p. 1. doi: 10.1117/12.617169.

[117] F. T. Z. Toma, Md. S. Rahman, K. Md. A. Hussain, and S. Ahmed, “Thin Film Deposition Techniques: A Comprehensive Review,” *Journal of Modern Nanotechnology*, vol. 4, p. 6, Nov. 2024, doi: 10.53964/jmn.2024006.

[118] L. R. Pederson, P. Singh, and X.-D. Zhou, “Application of vacuum deposition methods to solid oxide fuel cells,” *Vacuum*, vol. 80, no. 10, pp. 1066–1083, Aug. 2006, doi: 10.1016/j.vacuum.2006.01.072.

[119] M. Oksa, E. Turunen, T. Suhonen, T. Varis, and S.-P. Hannula, “Optimization and Characterization of High Velocity Oxy-fuel Sprayed Coatings: Techniques, Materials, and Applications,” *Coatings*, vol. 1, no. 1, pp. 17–52, Sep. 2011, doi: 10.3390/coatings1010017.

[120] A. Meghwal, A. Anupam, B. S. Murty, C. C. Berndt, R. S. Kottada, and A. S. M. Ang, "Thermal Spray High-Entropy Alloy Coatings: A Review," *Journal of Thermal Spray Technology*, vol. 29, no. 5, pp. 857–893, Jun. 2020, doi: 10.1007/s11666-020-01047-0.

[121] J. Ann Gan and C. C. Berndt, "Thermal spray forming of titanium and its alloys," in *Titanium Powder Metallurgy*, Elsevier, 2015, pp. 425–446. doi: 10.1016/B978-0-12-800054-0.00023-X.

[122] L. Bianchi, A. C. Leger, M. Vardelle, A. Vardelle, and P. Fauchais, "Splat formation and cooling of plasma-sprayed zirconia," *Thin Solid Films*, vol. 305, no. 1–2, pp. 35–47, Aug. 1997, doi: 10.1016/S0040-6090(97)80005-3.

[123] P. Kotalík and K. Voleník, "Cooling rates of plasma-sprayed metallic particles in liquid and gaseous nitrogen," *J. Phys. D Appl. Phys.*, vol. 34, no. 4, pp. 567–573, Feb. 2001, doi: 10.1088/0022-3727/34/4/318.

[124] K. Bobzin, L. Zhao, H. Heinemann, and E. Burbaum, "Influence of the atmospheric plasma spraying parameters on the coating structure and the deposition efficiency of silicon powder," *The International Journal of Advanced Manufacturing Technology*, vol. 123, no. 1–2, pp. 35–47, Nov. 2022, doi: 10.1007/s00170-022-10008-6.

[125] N. Hosseinabadi and H. A. Dehghanian, *Suspension Plasma Spray Coating of Advanced Ceramics*. Boca Raton: CRC Press, 2022. doi: 10.1201/9781003285014.

[126] I. Koresh, Z. Tang, and T. Troczynski, "A novel approach to prepare Li-La-Zr-O solid state electrolyte films by suspension plasma spray," *Solid State Ion.*, vol. 368, p. 115679, Oct. 2021, doi: 10.1016/j.ssi.2021.115679.

[127] J. Yu *et al.*, "Research and Application of High-Velocity Oxygen Fuel Coatings," *Coatings*, vol. 12, no. 6, p. 828, Jun. 2022, doi: 10.3390/coatings12060828.

[128] G. Bolelli *et al.*, "Comparison between plasma- and HVOF-sprayed ceramic coatings. Part I: microstructure and mechanical properties," *International Journal of Surface Science and Engineering*, vol. 1, no. 1, p. 38, 2007, doi: 10.1504/IJSURFSE.2007.013620.

[129] M. Gell *et al.*, "The Solution Precursor Plasma Spray Process for Making Durable Thermal Barrier Coatings," in *Volume 2: Turbo Expo 2005*, ASMEDC, Jan. 2005, pp. 905–911. doi: 10.1115/GT2005-68942.

[130] A. Kebriyaei, M. R. Rahimipour, M. Razavi, and A. Alizade Herfati, "Effect of Solution Precursor on Microstructure and High-Temperature Properties of the Thermal Barrier Coating Made by Solution Precursor Plasma Spray (SPPS) Process," *Journal of Thermal Spray Technology*, vol. 32, no. 1, pp. 8–28, Feb. 2023, doi: 10.1007/s11666-022-01470-5.

[131] R. A. Wicaksono, A. Ardeshiri Lordejani, and S. Bagherifard, "Current Trends and Future Perspective for Cold Spray Metal-Ceramic Composites," *Adv. Eng. Mater.*, vol. 27, no. 10, May 2025, doi: 10.1002/adem.202401657.

[132] G. Mauer, K.-H. Rauwald, Y. J. Sohn, and R. Vaßen, "The Potential of High-Velocity Air-Fuel Spraying (HVAF) to Manufacture Bond Coats for Thermal Barrier Coating Systems," *Journal of Thermal Spray Technology*, vol. 33, no. 2–3, pp. 746–755, Mar. 2024, doi: 10.1007/s11666-023-01659-2.

[133] J. Sung *et al.*, “Recent advances in all-solid-state batteries for commercialization,” *Mater. Chem. Front.*, vol. 8, no. 8, pp. 1861–1887, 2024, doi: 10.1039/D3QM01171B.

[134] A. Moridi, S. M. Hassani-Gangaraj, M. Guagliano, and M. Dao, “Cold spray coating: review of material systems and future perspectives,” *Surface Engineering*, vol. 30, no. 6, pp. 369–395, Jun. 2014, doi: 10.1179/1743294414Y.0000000270.

[135] M. Liu *et al.*, “Plasma spray–physical vapor deposition toward advanced thermal barrier coatings: a review,” *Rare Metals*, vol. 39, no. 5, pp. 479–497, May 2020, doi: 10.1007/s12598-019-01351-x.

[136] X. Liang, Y. Wang, X. Zhang, D. Han, L. Lan, and Y. Zhang, “Performance study of a Li4Ti5O12 electrode for lithium batteries prepared by atmospheric plasma spraying,” *Ceram. Int.*, vol. 45, no. 17, pp. 23750–23755, Dec. 2019, doi: 10.1016/j.ceramint.2019.08.091.

[137] A. Hasani *et al.*, “Localized Phase and Elemental Mapping in Solid-State Lithium Battery LTO Anode Thin-Film Produced by a Novel Suspension Plasma Spray Approach,” *Journal of Thermal Spray Technology*, May 2025, doi: 10.1007/s11666-025-02003-6.

[138] D. Yost, J. Laurer, K. Childrey, C. Cai, and G. M. Koenig, “Fabrication and Characterization of Plasma Sprayed TiO2 and Li4Ti5O12 Materials as All Active Material Lithium-Ion Battery Electrodes,” *Batteries*, vol. 9, no. 12, p. 598, Dec. 2023, doi: 10.3390/batteries9120598.

[139] T.-H. Hsueh *et al.*, “LiCoO $_2$ Battery Electrode Fabricated by High Deposition-Rate Atmospheric Plasma Spraying for Lithium Battery,” *J. Electrochem. Soc.*, vol. 169, no. 10, p. 100506, Oct. 2022, doi: 10.1149/1945-7111/ac9555.

[140] D. Lou, H. Hong, M. Ellingsen, and R. Hrabe, “Supersonic cold-sprayed Si composite alloy as anode for Li-ion batteries,” *Appl. Phys. Lett.*, vol. 122, no. 2, Jan. 2023, doi: 10.1063/5.0135408.

[141] S.-L. Zhang, C.-X. Li, C.-J. Li, G.-J. Yang, and M. Liu, “Application of high velocity oxygen fuel flame (HVOF) spraying to fabrication of La0.8Sr0.2Ga0.8Mg0.2O3 electrolyte for solid oxide fuel cells,” *J. Power Sources*, vol. 301, pp. 62–71, Jan. 2016, doi: 10.1016/j.jpowsour.2015.09.050.

[142] Y. Wu *et al.*, “Rapid Processing of Uniform, Thin, Robust, and Large-Area Garnet Solid Electrolyte by Atmospheric Plasma Spraying,” *Adv. Energy Mater.*, vol. 13, no. 30, Aug. 2023, doi: 10.1002/aenm.202300809.

[143] S. Singh *et al.*, “Innovative manufacturing of nanostructured solid state electrolyte using suspension plasma spray,” *Surf. Coat. Technol.*, vol. 507, p. 132112, Jul. 2025, doi: 10.1016/j.surfcoat.2025.132112.

[144] Y.-Q. Sun, X.-T. Luo, Y.-S. Zhu, X.-J. Liao, and C.-J. Li, “Li3PO4 electrolyte of high conductivity for all-solid-state lithium battery prepared by plasma spray,” *J. Eur. Ceram. Soc.*, vol. 42, no. 10, pp. 4239–4247, Aug. 2022, doi: 10.1016/j.jeurceramsoc.2022.04.010.

[145] X.-C. Bu, N. Chen, X.-T. Luo, and C.-J. Li, “Plasma Spray Deposition of Na3Zr2Si2PO12 Electrolyte for High-Performance All-Solid-State Sodium-Ion Battery,” *Journal of Thermal Spray Technology*, vol. 34, no. 2–3, pp. 495–505, Mar. 2025, doi: 10.1007/s11666-025-01928-2.

[146] M. Ockel *et al.*, “Atmospheric Plasma Spraying for Copper Coating of Ceramic Solid Electrolytes for Anode-Free Solid-State Batteries with Increased Interfacial Contact,” in *2024 1st International Conference on Production Technologies and Systems for E-Mobility (EPTS)*, IEEE, Jun. 2024, pp. 1–5. doi: 10.1109/EPTS61482.2024.10586742.

[147] J. Košir, S. Mousavihashemi, B. P. Wilson, E.-L. Rautama, and T. Kallio, “Comparative analysis on the thermal, structural, and electrochemical properties of Al-doped Li7La3Zr2O12 solid electrolytes through solid state and sol-gel routes,” *Solid State Ion.*, vol. 380, p. 115943, Jul. 2022, doi: 10.1016/j.ssi.2022.115943.

[148] T. Park, S. Lee, and D.-M. Kim, “Low-Temperature Manufacture of Cubic-Phase Li7La3Zr2O12 Electrolyte for All-Solid-State Batteries by Bed Powder,” *Crystals (Basel).*, vol. 14, no. 3, p. 271, Mar. 2024, doi: 10.3390/cryst14030271.

[149] H. Zhang *et al.*, “On High-Temperature Thermal Cleaning of $Li_7La_3Zr_2O_{12}$ Solid-State Electrolytes,” *ACS Appl. Energy Mater.*, vol. 6, no. 13, pp. 6972–6980, Jul. 2023, doi: 10.1021/acsaem.3c00459.

[150] J. Liang *et al.*, “Stabilizing and understanding the interface between nickel-rich cathode and PEO-based electrolyte by lithium niobium oxide coating for high-performance all-solid-state batteries,” *Nano Energy*, vol. 78, p. 105107, Dec. 2020, doi: 10.1016/j.nanoen.2020.105107.

[151] Z. Jiang, Q. Han, S. Wang, and H. Wang, “Reducing the Interfacial Resistance in All-Solid-State Lithium Batteries Based on Oxide Ceramic Electrolytes,” *ChemElectroChem*, vol. 6, no. 12, pp. 2970–2983, Jun. 2019, doi: 10.1002/celc.201801898.

[152] J. Yang *et al.*, “Research Advances in Interface Engineering of Solid-State Lithium Batteries,” *Carbon Neutralization*, vol. 4, no. 1, Jan. 2025, doi: 10.1002/cnl2.188.

[153] L. Indrizzi, N. Ohannessian, D. Pergolesi, T. Lippert, and E. Gilardi, “Pulsed Laser Deposition as a Tool for the Development of All Solid-State Microbatteries,” *Helv. Chim. Acta*, vol. 104, no. 2, Feb. 2021, doi: 10.1002/hlca.202000203.

[154] G. Ryoo *et al.*, “Laser-Assisted Interfacial Engineering for High-Performance All-Solid-State Batteries,” *ChemElectroChem*, vol. 10, no. 20, Oct. 2023, doi: 10.1002/celc.202300349.

[155] R. K. Guduru, U. Dixit, and A. Kumar, “A critical review on thermal spray based manufacturing technologies,” *Mater. Today Proc.*, vol. 62, pp. 7265–7269, 2022, doi: 10.1016/j.matpr.2022.04.107.

[156] Z. D. Hood, Y. Zhu, L. J. Miara, W. S. Chang, P. Simons, and J. L. M. Rupp, “A sinter-free future for solid-state battery designs,” *Energy Environ. Sci.*, vol. 15, no. 7, pp. 2927–2936, 2022, doi: 10.1039/D2EE00279E.

[157] D. Yang, “Applications of Laser Material Processing for Solid-State Lithium Batteries,” *Batteries*, vol. 11, no. 4, p. 128, Mar. 2025, doi: 10.3390/batteries11040128.

[158] J. Bonse and J. Krüger, “Structuring of thin films by ultrashort laser pulses,” *Applied Physics A*, vol. 129, no. 1, p. 14, Jan. 2023, doi: 10.1007/s00339-022-06229-x.

[159] X. Li and Y. Guan, “Theoretical fundamentals of short pulse laser–metal interaction: A review,” *Nanotechnology and Precision Engineering*, vol. 3, no. 3, pp. 105–125, Sep. 2020, doi: 10.1016/j.npe.2020.08.001.

[160] A. G. Lekatou *et al.*, “Effect of Laser Surface Melting on the Microstructure and Corrosion Resistance of Laser Powder Bed Fusion and Wrought Ti-6Al-4V Alloys,” *Coatings*, vol. 15, no. 11, p. 1285, Nov. 2025, doi: 10.3390/coatings15111285.

[161] V. Kumar, R. Verma, S. Kango, and V. S. Sharma, “Recent progresses and applications in laser-based surface texturing systems,” *Mater. Today Commun.*, vol. 26, p. 101736, Mar. 2021, doi: 10.1016/j.mtcomm.2020.101736.

[162] N. Zamperlin *et al.*, “Advanced manufacturing of thin-film lithium metal anode by pulsed-laser deposition for next-generation solid-state batteries,” *J. Power Sources*, vol. 655, p. 237986, Nov. 2025, doi: 10.1016/j.jpowsour.2025.237986.

[163] A. Ali, Y. W. Chiang, and R. M. Santos, “X-ray Diffraction Techniques for Mineral Characterization: A Review for Engineers of the Fundamentals, Applications, and Research Directions,” *Minerals*, vol. 12, no. 2, p. 205, Feb. 2022, doi: 10.3390/min12020205.

[164] D. N. G. Krishna and J. Philip, “Review on surface-characterization applications of X-ray photoelectron spectroscopy (XPS): Recent developments and challenges,” *Applied Surface Science Advances*, vol. 12, p. 100332, Dec. 2022, doi: 10.1016/j.apsadv.2022.100332.

[165] T. Kato *et al.*, “A comprehensive and quantitative SEM–EDS analytical process applied to lithium-ion battery electrodes,” *Sci. Rep.*, vol. 15, no. 1, p. 5428, Feb. 2025, doi: 10.1038/s41598-025-89362-w.

[166] B. Putz *et al.*, “Glass and nanocrystalline phase formation in CuZrAg alloys: Insights from combinatorial thin film libraries studied by mapping synchrotron X-ray diffraction,” *Mater. Des.*, vol. 244, p. 113144, Aug. 2024, doi: 10.1016/j.matdes.2024.113144.

[167] C. Ioannidou *et al.*, “In-situ synchrotron X-ray analysis of metal Additive Manufacturing: Current state, opportunities and challenges,” *Mater. Des.*, vol. 219, p. 110790, Jul. 2022, doi: 10.1016/j.matdes.2022.110790.

[168] R. Zhou *et al.*, “High temperature in-situ synchrotron X-ray diffraction technique of thermal barrier coatings under thermal gradient and mechanical loads,” *Journal of Materials Research and Technology*, vol. 33, pp. 9155–9165, Nov. 2024, doi: 10.1016/j.jmrt.2024.11.234.

[169] H. A. O. Wang *et al.*, “Quantitative Chemical Imaging of Element Diffusion into Heterogeneous Media Using Laser Ablation Inductively Coupled Plasma Mass Spectrometry, Synchrotron Micro-X-ray Fluorescence, and Extended X-ray Absorption Fine Structure Spectroscopy,” *Anal. Chem.*, vol. 83, no. 16, pp. 6259–6266, Aug. 2011, doi: 10.1021/ac200899x.

[170] C. N. Borca *et al.*, “The microXAS beamline at the swiss light source: Towards nano-scale imaging,” *J. Phys. Conf. Ser.*, vol. 186, p. 012003, Sep. 2009, doi: 10.1088/1742-6596/186/1/012003.

[171] Sascha Grimm and Tilman Donath, “https://www.dectris.com/en/detectors/x-ray-detectors/eiger2/eiger2-for-synchrotrons/.”

[172] A. W. Colldeweih, M. G. Makowska, O. Tabai, D. F. Sanchez, and J. Bertsch, “Zirconium hydride phase mapping in Zircaloy-2 cladding after delayed hydride cracking,” *Materialia (Oxf).*, vol. 27, p. 101689, Mar. 2023, doi: 10.1016/j.mtla.2023.101689.

[173] G. Ashiotis *et al.*, “The fast azimuthal integration Python library: *pyFAI*,” *J. Appl. Crystallogr.*, vol. 48, no. 2, pp. 510–519, Apr. 2015, doi: 10.1107/S1600576715004306.

[174] V. A. Solé, E. Papillon, M. Cotte, Ph. Walter, and J. Susini, “A multiplatform code for the analysis of energy-dispersive X-ray fluorescence spectra,” *Spectrochim. Acta Part B At. Spectrosc.*, vol. 62, no. 1, pp. 63–68, Jan. 2007, doi: 10.1016/j.sab.2006.12.002.

[175] A. Hasani *et al.*, “Laser Processing of Liquid Feedstock Plasma-Sprayed Lithium Titanium Oxide Solid-State-Battery Electrode,” *Coatings*, vol. 14, no. 2, p. 224, Feb. 2024, doi: 10.3390/coatings14020224.

[176] A. Kozlova, N. Uvarov, M. Sharafutdinov, E. Gerasimov, and Y. Mateyshina, “In situ study of solid-state synthesis of Li4Ti5O12–Li2TiO3 and Li4Ti5O12–TiO2 composites,” *J. Solid State Chem.*, vol. 313, p. 123302, Sep. 2022, doi: 10.1016/j.jssc.2022.123302.

[177] Y. Kang, Y. Xie, F. Su, K. Dai, M. Shui, and J. Shu, “α-Li_2TiO_3: a new ultrastable anode material for lithium-ion batteries,” *Dalton Transactions*, vol. 51, no. 47, pp. 18277–18283, 2022, doi: 10.1039/D2DT03115A.

[178] Carmen. de la Torre-Gamarra *et al.*, “Tape casting manufacturing of thick Li4Ti5O12 ceramic electrodes with high areal capacity for lithium-ion batteries,” *J. Eur. Ceram. Soc.*, vol. 41, no. 1, pp. 1025–1032, Jan. 2021, doi: 10.1016/j.jeurceramsoc.2020.07.049.

[179] A. Sharafi *et al.*, “Impact of air exposure and surface chemistry on Li–$Li_7La_3Zr_2O_{12}$ interfacial resistance,” *J. Mater. Chem. A Mater.*, vol. 5, no. 26, pp. 13475–13487, 2017, doi: 10.1039/C7TA03162A.

[180] H. Zhang *et al.*, “On High-Temperature Thermal Cleaning of $Li_7La_3Zr_2O_{12}$ Solid-State Electrolytes,” *ACS Appl. Energy Mater.*, vol. 6, no. 13, pp. 6972–6980, Jul. 2023, doi: 10.1021/acsaem.3c00459.

[181] P. Ghorbanzade *et al.*, “Impact of thermal treatment on the Li-ion transport, interfacial properties, and composite preparation of LLZO garnets for solid-state electrolytes,” *J. Mater. Chem. A Mater.*, vol. 11, no. 22, pp. 11675–11683, 2023, doi: 10.1039/D3TA01145C.

[182] P. Ghorbanzade, P. López-Aranguren, and J. M. López del Amo, “A Vision for LLZO Carbonate Formation: Perspectives on Surface Treatment Approaches and Characterization Techniques,” *ChemElectroChem*, vol. 11, no. 11, Jun. 2024, doi: 10.1002/celc.202400136.

[183] C. Schneider, M. G. Makowska, and J. Bertsch, “3D microscopic X-ray fluorescence and diffraction analysis of a fuel-cladding interface of a highly irradiated boiling water reactor fuel rod,” *Journal of Nuclear Materials*, vol. 616, p. 156020, Oct. 2025, doi: 10.1016/j.jnucmat.2025.156020.

[184] A. Hasani *et al.*, “Advanced synchrotron micro characterization of laser post-processed plasma sprayed LLZO solid-state battery electrolyte,” *IOP Conf. Ser. Mater. Sci. Eng.*, vol. 1332, no. 1, p. 012022, Aug. 2025, doi: 10.1088/1757-899X/1332/1/012022.

[185] J.-H. Choi *et al.*, “Multi-layer electrode with nano-Li4Ti5O12 aggregates sandwiched between carbon nanotube and graphene networks for high power Li-ion batteries,” *Sci. Rep.*, vol. 4, no. 1, p. 7334, Dec. 2014, doi: 10.1038/srep07334.

[186] B. Priyono, P. B. Murti, A. Z. Syahrial, and A. Subhan, “Optimizing the performance of Li4Ti5O12 anode synthesized from TiO2 xerogel and LiOH with hydrothermal-ball mill method by using acetylene black,” 2017, p. 020005. doi: 10.1063/1.4979221.

[187] M. H. Futscher, L. Brinkman, A. Müller, J. Casella, A. Aribia, and Y. E. Romanyuk, “Monolithically-stacked thin-film solid-state batteries,” *Commun. Chem.*, vol. 6, no. 1, p. 110, Jun. 2023, doi: 10.1038/s42004-023-00901-w.

[188] J. Cha, Y.-J. Lee, and D.-W. Kim, “High-performance all-solid-state lithium batteries enabled by a highly adhesive dry-processable binder,” *Mater. Today Energy*, vol. 53, p. 102009, Oct. 2025, doi: 10.1016/j.mtener.2025.102009.

[189] P. N. Didwal and G. Chen, “Lithium-metal all-solid-state batteries enabled by polymer-coated halide solid electrolytes,” *EES Batteries*, vol. 1, no. 6, pp. 1612–1625, 2025, doi: 10.1039/D5EB00134J.

[190] J. Sung *et al.*, “Infiltration-driven performance enhancement of poly-crystalline cathodes in all-solid-state batteries,” *NPG Asia Mater.*, vol. 16, no. 1, p. 53, Oct. 2024, doi: 10.1038/s41427-024-00555-7.

TURUN
YLIOPISTO
UNIVERSITY
OF TURKU

Painosalama, Turku, Finland 2026

ISBN 978-952-02-0545-4 (PRINT)
ISBN 978-952-02-0546-1 (PDF)
ISSN 2736-9390 (Painettu/Print)
ISSN 2736-9684 (Sähköinen/Online)